The Use of Metal Nanoparticles as an Antimicrobial Agent and as a Catalyst for Organic Synthesis

By

Nancy Marina

Thesis submitted to the

Faculty of Graduate and Postdoctoral Studies

In partial fulfillment of the requirements

For the Master degree in

Chemistry

Department of Chemistry and Bimolecular Sciences

University of Ottawa

To my husband Jessen Khoury, and my family

For the love and encouragement

&

To my mentors

Dr. Juan Scaiano

&

Dr. Anabel Lanterna

Abstract

Nanomaterial's applications have expanded greatly in the last few decades due to their interesting properties. Example of nanomaterials are metal nanoparticles NP. NP have interesting physical and optical properties that make them different and more useful than their bulk counterpart. Some of these properties are the large surface area to mass ratio and their ability to absorb light. NP have been applied in the health, environment, and catalysis fields

The main focus of this thesis will be on the applications of nanomaterials in medicine and catalysis. In the first part of the thesis, coated polydispersed and polymorphic silver nanostructures AgNS were synthesized using seed mediated method. The synthesized AgNS were characterized using SEM, TEM, and UV-VIS. The stability of these AgNS were determined by measuring the shift in the plasmon band over time and by measuring their zeta potential. Moreover, the bactericidal properties of coated AgNS were tested on gram negative bacteria such as *Escherichia coli and Pseudomonas aeruginosa* and gram positive bacteria such *as Methicillin- Resistant Staphylococcus aureus (MRSA) and Staphylococcus aureus.*

The second part of the thesis discusses the field of nanocatalysis where different supported metal nanoparticles on TiO_2 were synthesized and characterized by TEM, diffuse reflectance DR, XPS and ICP. The activity of the synthesized catalysts was tested for Ullmann C-C cross coupling reaction. The use of the photoresponisve Pd@TiO_2 under the combination of UVA 368 and visible light 465nm irradiation offered the highest selectivity toward the cross coupling product.

Acknowledgments

I am very lucky to have been a graduate student in the Scaiano lab. Tito has been a great mentor. I thank Tito for being a very supportive supervisor in good and bad time. Thank you Tito for giving me the opportunity to be part of your lab. I have learned a lot about photochemistry and instrumentation over the last few years. I would also like to specifically thank Anabel Lanterna for being an amazing supervisor. I learned a lot from her. She taught me how to never give up on things no matter how impossible they seem. I would also like to thank the entire Scaiano group for being there for me whenever I needed them. I would like to specially thank Ayda Elhage for helping me around the lab and being a great friend.

Table of Contents

List of Figures

List of Figures

List of Figures

List of Figures

List of Figures

List of Schemes

List of Tables

List of Tables

List of Acronyms

[ ]	Concentration
ζ Potential	Zeta Potential
0D	Zero dimensional
1D	One dimensional
2D	Two dimensional
3D	Three dimensional
Ag	Silver
$AgNO_3$	Silver nitrate
AgNS	Silver nanostructures
Au	Gold
AuNR	Gold nanorods
Aq	Aqueous
Asp	Aspartame
Br	Bromine
Cs_2CO_3	Cesium carbonate
C	Carbon
Cu	Copper
CND	Carbon nanodiamond
CTAB	hexadecyltrimethylammonium bromide
Degrees C	Degrees Celsius
CB	Conduction band
DNA	Deoxyribonucleic acid
DABCO	1,4-Diazabicyclo[2.2.2]octane

DCM	Dichloromethane
DR	Diffuse reflectance
EDS	Energy- dispersive X-ray spectroscopy
eV	Electron volt
FRET	Förster Resonance Energy Transfer
HEBA	4-hydroxyethoxybenzoic acid
EWG	Electron withdrawing group
EDG	Electron donating group
Glu	Glucosamine
GC-FID	Gas Chromatograph coupled to a Flame Ionization Detector
GC-MS	Gas Chromatograph coupled with mass spectrometer
HCl	Hydrochloric acid
THF	Tetrahydrofuran
H^+	Proton
HOMO	Highest occupied molecular orbital
hv	Light
ICP-OES	Inductively coupled plasma optical emission spectroscopy
IR	Infrared
I-2959	Irgacure 2959
LED	Light emitting diodes
LSPR	Localized Surface Plasmon Resonance
LUMO	Lowest occupied molecular orbital
MeCN	Acetonitrile
MeOH	Methane
mM	Millimolar

mmol	Millimole
MIC	Minimum inhibition concentrations
$MBEC_{80}$	Minimal biofilm eradication concentration
MRSA	methicillin-resistant *Staphylococcus aureus*
N	Nitrogen
$NaBH_4$	Sodium borohydride
NaOH	Sodium hydroxide
nm	Nanometer
NP	Nanoparticles
NMR	Nuclear magnetic resonance
P	Product
PC	Photocatalyst
PBS	phosphate buffered saline
Pd	Palladium
Pt	Platinum
QD	Quantum dots
R	Reactant
ROS	Reactive oxygen species
rpm	Revolutions per minute
S	Substrate
SEM	Scanning Electron Microscopy
Suc	Sucralose
Sor	Sorbitol
SPP	Surface Plasmon Polariton
TEM	Transmission Electron Microscopy

TEA	Triethylamine
TEMPO	2,2,6,6-Tetramethyl-1-piperidinyloxy
TiO_2	Titanium dioxide
TLC	Thin layer chromatography
TMS	Tetramethylsilane
UV	Ultraviolet
VB	Valence band
VIS	Visible
XPS	X-ray Photoelectron Spectroscopy

Chapter 1
Introduction

1. Definition of nanomaterials

Nanomaterials are materials that range in size from 1 to 100 nm.[1] Nanomaterials are amorphous or crystalline structures that can consist of single or multi-elements (i.e. metallic, non-metallic, polymeric, etc.) and be synthesized into different shapes and sizes. Figure 1.1 illustrates the size of nanoparticles (NP) relative to other biological and non-biological materials.

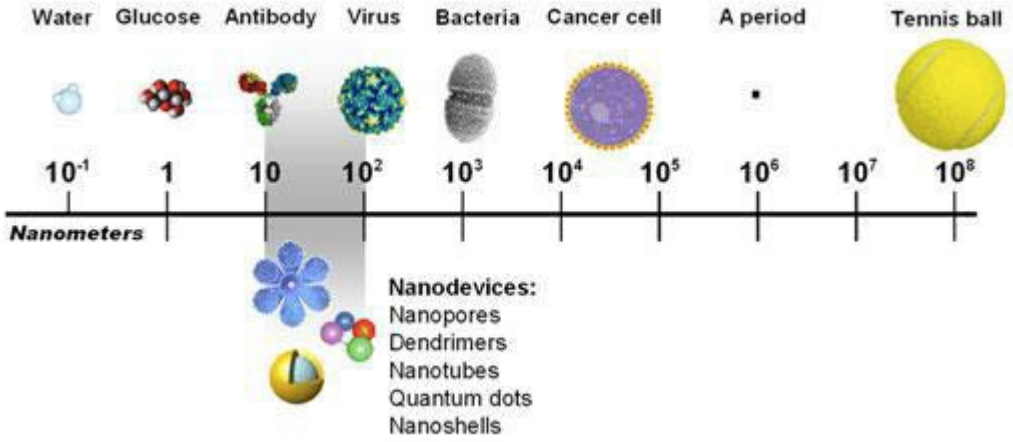

Figure 1.1: NP size relationship to biological and non-biological materials. Adapted from ref. [2] © 2015 Nikalje AP.

2. History of nanoparticles

In the past 150 years researchers have been extensively studying colloidal NP. However, the first use of NP was dated to ancient time. The Roman Empire was known for their fascinating architectures and buildings. Ancient people were the masters of adding nanoscale material to bulk material in order to improve properties. One of the oldest examples that were reported on the use of NP is the Lycurgus cup (AD 400), the cup was made from glass but it displayed a strange phenomenon. The colour of the cup changes depending on whether the cup is illuminated from the front (green, Figure 1.2 left) or from inside (red, Figure 1.2 right). This incident remained a mystery until the British museum analyzed the glass material of the cup. It was found that Ag and AuNP were

added to the glass in a ratio of 7:3 and relative size of 70 nm. This composition was responsible for the different colours seen when the cup reflects or transmits the light (*vide infra*).[3]

Figure 1.2: Lycurgus cup. Left: Green color adopted due to light reflection; Right: Red color adopted due to light transmission. © Trustees of the British Museum. Reproduced from ref.[4] with permission from Springer Nature, Nature photonics.

Another example where nanomaterials were used in the old ages is the Damascus sword. [5] Damascus steel amazed people with its strength, elasticity and durability. The secret of the Damascus steel remained a mystery till 2006 when a group of German researchers analyzed the composition of the sword and to their surprise it contained carbide nanowires and carbon nanotubes.

3. Classification of nanomaterials

There are varieties of ways that are used to classify nanomaterials, such as dimensionality and chemical composition.

In terms of dimensions, nanomaterials can be classified according to the size of each 3D dimensions [6] Thus, zero dimensional (0D) materials where all the dimensions fall within the nanoscale (below 100 nm) are usually considered NP (Figure 1.3 A); one dimensional (1D) materials where two dimensions are in the nanoscale range and one in the macroscale, for example nanotubes, nanowires and nanorods (Figure 1.3 B); two dimensional (2D) materials with only one dimension in the nano range, i.e. nanoplates

and nanofilms (Figure 1.3 C); and three dimensional (3D) materials with all their dimensions in the macroscale. Figure 1.3 D

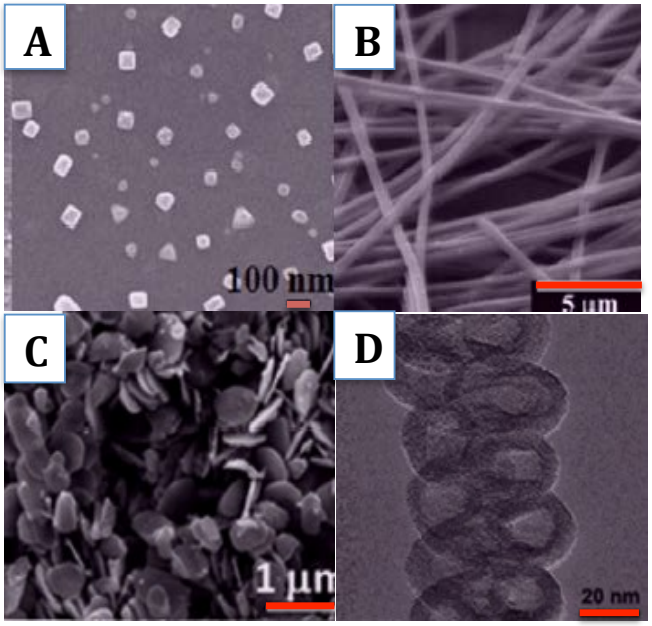

Figure 1.3: SEM images of different nanomaterials. A represent NP, B nanoribbons, C nanoplates and D nanocoils. Adapted from ref. [6] with permission from Elsevier, Progress in Material Science

According to their chemical composition, NP can be categorized into carbon-based nanomaterial such as graphite and carbon nanotubes, or metal NP usually constituted by noble transition metals, such as Au, Ag, or Pd, among others. This thesis will be only focused on the latter ones.

Metal NP, such as Au, Ag and Cu, have special optical properties due to the presence of localized surface plasmon resonance (LSPR), which is responsible for their great absorption properties in the visible region of the electromagnetic solar spectrum. Other metal NP, like Pd or Pt, do not display this kind of behaviour, therefore metal NP can be categorized into plasmonic and non-plasmonic NP based on the optical properties that they have in the visible region.[7, 8]

4. Plasmonic metal nanoparticles

The plasmonic properties of metals strongly depend on the material geometry.[9] In order to understand the LSPR in NP, one could start analysing this phenomenum over flat gold surfaces. Theoretically, a slab of metal consists of a periodic array of positive

charges (the nuclei) and electrons that are bound to the positive charges by electrostatic interactions. When the metal slab absorbs polarized light – with its oscillating electric field component perpendicular to the surface of the metal –, the electric field leads to oscillation of the electrons in the metal. Then the oscillating electrons couple with the electromagnetic field mode and they travel as a package forming a surface wave. This phenomenon is known as surface plasmon polaritons (SPP) and is shown in Figure 1.4, left panel. In SPP the surface plasmon wave propagates between the metal surface and the dielectric medium, for that reason, both the metal and the medium dielectric constants are important for the properties of the surface plasmon.

In the case of NP, they absorb light in the same manner as SPP. However, the NP are not flat like metal slab, their surface has curvature which defines its finite dimensions usually smaller than the excitation wavelength. Moreover, the surface plasmon wave is able to penetrate the entire NP due its small size. Polaritons are just due to oscillating electro-magnetic field that is trapped on the particle. The electrons oscillate together but only the surface has oscillating charge, which is known as surface plasmons as shown in Figure 1.4, right panel. [10, 11]

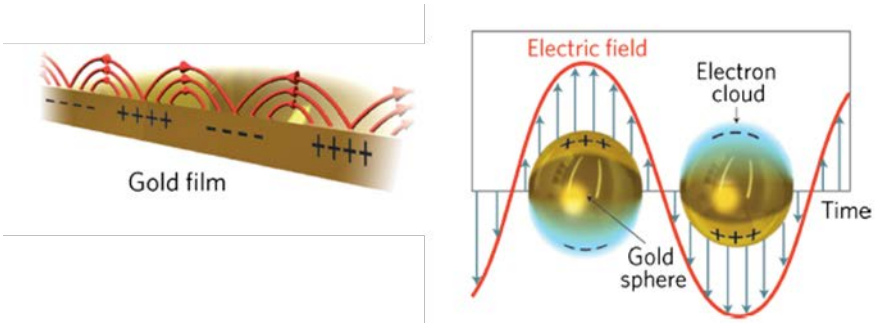

Figure 1.4: Schematic representation of plasmon resonance. Left: propagating SPP along the dielectric–metal interface. Right: localized surface Plasmon on the surface of metal NP. Adapted from ref. [11] with permission Springer Nature, Nature Photonics.

The plasmon absorption was described by Mie in 1908, after he solved Maxwell's equation for spherical NP. Thus, assuming that the particles are in homogenous dielectric material, when the radius of NP is smaller than the wavelength of the incident light, only the dipolar mode participates in the absorption. [12, 13] The ability of the particle to absorb light is illustrated in equation 1.2

$$a = 3\ \epsilon_0\ V \frac{\epsilon - \epsilon_m}{\epsilon + 2\epsilon_m} \qquad (1.2)$$

Where α is the polarizability, $\in_0$ is the permittivity of vacuum, V corresponds to the volume of the particles, $\in$ is the permittivity of the material, and $\in_m$ is the permittivity of the particles' environment.

Le Ru and Etchegonic described the relation between polarizability and the radius of the particles (R). Equation 1.3 shows how polarizability is directly proportional to the cube of R, and therefore related to particle size.

$$\alpha = 4 \in_0 \pi R^3 \frac{\in -1}{\in +2} \qquad (1.3)$$

According to equation 1.2, resonance occurs at the maximum absorbance of light by the particle, which is achieved when

$$\in = -2 \in_m \qquad (1.4)$$

Therefore, the dielectric constant of the material has to be negative in order for plasmon to absorb, a condition met by Au, Ag and Cu among others. {L. Dmitruk, 2009, Physical nature of anomalous optical transmission of thin absorptive corrugated films}

Mie assumed that for particles that are smaller than 20 nm, they tend to have an absorbance band that is dominated by a dipole whose position and widths are independent of size with the following equation. Where σ(ω) is the absorption cross section,

$$\sigma_{ext=} \frac{9V \in_m^{3/2}}{c} \cdot \frac{\omega \in_2 (\omega)}{[\in_1 (\omega) + 2 \in_m]^2 + \in_2 (\omega)^2} \qquad (1.5)$$

V is the volume of the particle, ω is the angular frequency of excitation, and c is the speed of light. $\in_m \ and \ \in = \in_1 (\omega) + i \in_2 (\omega)$ Illustrate the dielectric function of the medium and metal respectively.

Extinction consists of two phenomena, the first one is the absorption of light produced by plasmon, and the second one is the scattering of light due to particle size.

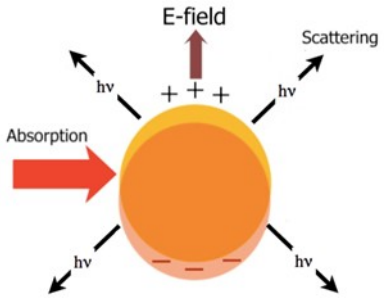

Figure 1.5: Illustration of the events contributing to the extinction: surface plasmon absorption of a metal NP and light scattering.

The decay of the plasmon occurs through de-phasing of the collective coherent oscillation of electrons in the particle. [14]

- **LSPR: dependence on size, shape, chemical nature and environment**

As mentioned above, LSPR depends on different factors such as size, shape, and chemical nature of the metal and dielectric media. Different sizes lead to different light absorption. When the particle size of Cu, Ag and Au is smaller than the wavelength of the incident light, they absorb light at different frequencies, which leads to different color of the colloidal solution. Larger particles absorb near IR light because the cross section for absorption and scattering depends on the polarizability (equations 1.6 and 1.7), which is proportional to the size of the particle (equation 1.3).[15] Figure 1.6. Illustrates the effect of different size of AuNP on the absorption of light. [16]

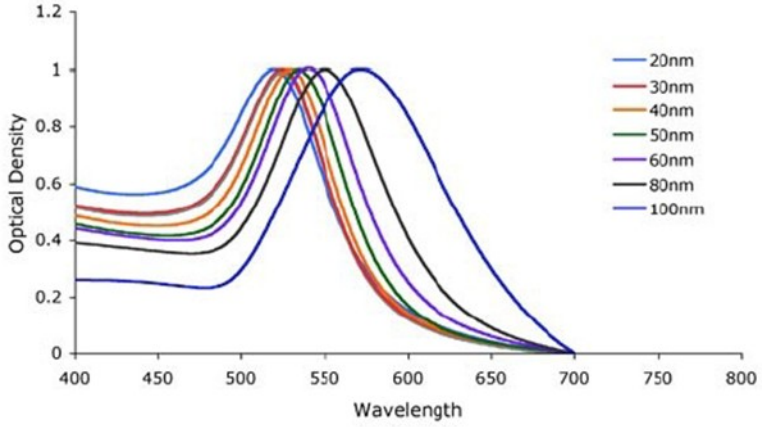

Figure 1.6. Extinction spectra of different-size AuNP suspended in water showing the dependence of LSPR with particle size. Reprinted with permission from cytodiagnostic Inc. [16]

Additionally, the shape of the NP plays an important role in adjusting the optical properties of the nanomaterial. When the NP is not symmetrical; the particles acquire extra plasmon resonance which is translated into transversal and longitudinal plasmons. Figure 1.7 shows the effect of different shape of AuNP on the LSPR. In some cases, more than one plasmon band can be distinguished, i.e. Au nanorods have transversal band at 530 nm and longitudinal SPR band at 640 nm, [17]

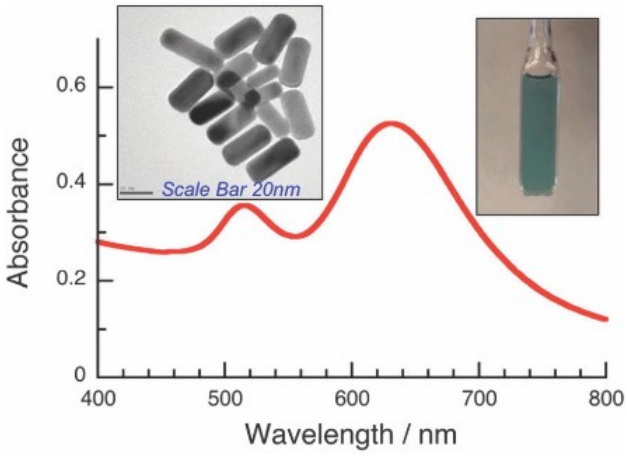

Figure 1.7. Absorption spectrum of colloidal AuNR solution in water that illustrates the presence of two plasmon bands. Adapted from ref.[17] with permission from Royal Society of Chemsitry, Chemical Communication.

The optical properties of AuNR have been described by Gans model for ellipsoids, where polarizibility is described in equation 1.6

$$\alpha_{x,y,z} = \frac{4\pi\, abc\, (\epsilon - \epsilon_m)}{3\epsilon_m + 3L_{x,y,z}\, (\epsilon - \epsilon_m)} \qquad (1.6)$$

Where, a,b, and c are the length of the ellipsoid along the axes x,y, and z, respectively, ∈_ is the permittivity of the material, ϵ_m is the permittivity of free space, and $L_{x,y,z}$ is the depolarization factor for the respective axes which in turn depends on the ellipticity of the particle. Therefore, the absorption of AuNR relies on the aspect ratio more than the absolute dimensions of the NP. [18]

As mentioned before, the absorption properties of the NP also depend on the nature of the metal used. For instance, Figure 1.8 presents the absorption spectra of CuNP, AgNP and AuNP; which shows that Cu absorbs at longer wavelengths than Au and Ag. [19]

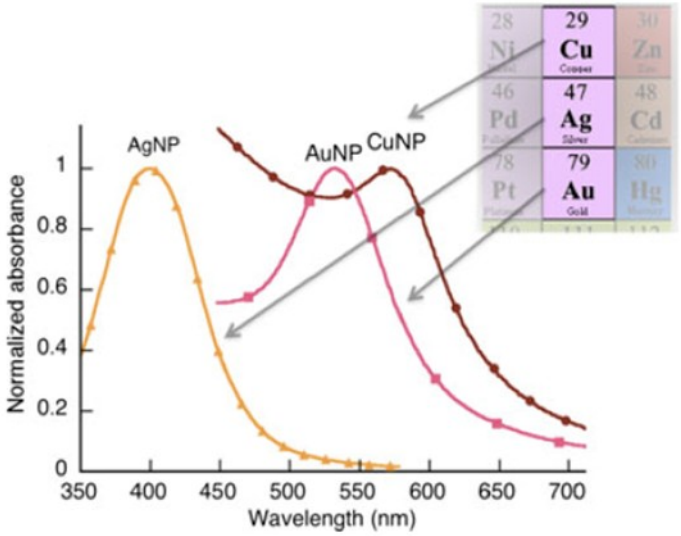

Figure 1.8: Illustration of the absorption spectra of colloidal Ag, Au and CuNP. Adapted from ref. [19] with permission from John Wiley and Sons, Photochemistry and Photobiology.

LSPR show also dielectric medium dependency as presented in equation 1.2. For instance, when AuNP are suspended in high concentration of NaCl they agglomerate leading to red-shift absorption, as larger particles absorb near the IR region because when the particles aggregate the conduction electrons become delocalized and shared with close particles (Figure 1.9).[16]

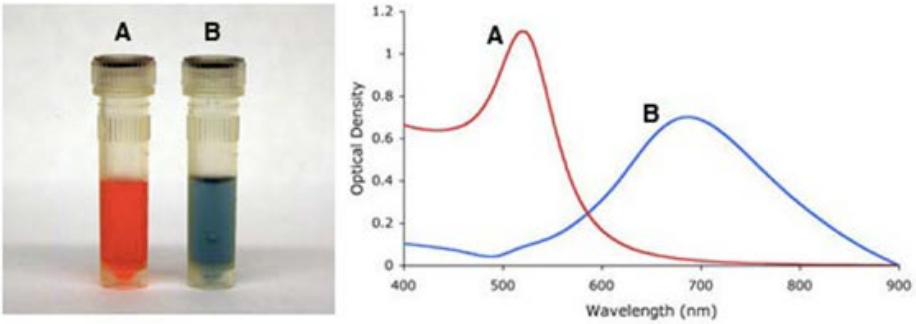

Figure 1.9 UV-Vis spectra (right) of monodisperse (A) 15 nm AuNP (B) in sodium chloride (NaCl). Reprinted with permission from cytodiagnostic Inc . [16]

- **LSPR effect**

The excitation of the plasmon can lead to many effects as illustrated in Figure 1.10. Thus, upon excitation the large absorption coefficient of AuNP can promote different phenomena such as antenna effect, electron-hole transfer, and heat transfer. The antenna effect leads to energy transfer and the generation of singlet (or triplet) excited state when a receiver is available close to the NP surface. This non-radiative resonance energy transfer is known as Förster Resonance Energy Transfer (FRET) or dipole-dipole interaction. FRET occurs via coulombic interaction, there is no electron transfer involved. FRET happens when there is orbital overlap between the donor and the acceptor, and therefore they must be within proximity and have a specific orientation. The efficiency of FRET is inversely proportional to the sixth power of the distance between donor and acceptor molecules. In the case of NP, this efficiency varies with the fourth power of the inverse of the distance (R^{-4}) and results from the coupling of the AuNP's plasmon resonance and the acceptor orbital.[20] The second effect observed upon plasmon excitation is the hole or electron transfer to molecules that act as electron donors or acceptors, and it is really important for catalytic applications. Finally, the third effect is related to the thermal relaxation of the plasmon, which leads to high surface temperature that facilitates chemical or physical changes of molecules in close proximity to the surface by

overcoming energy barriers. For example, a study performed by the Scaiano group showed that the temperature of the surface of AuNP can reach 500 ºC.[21]

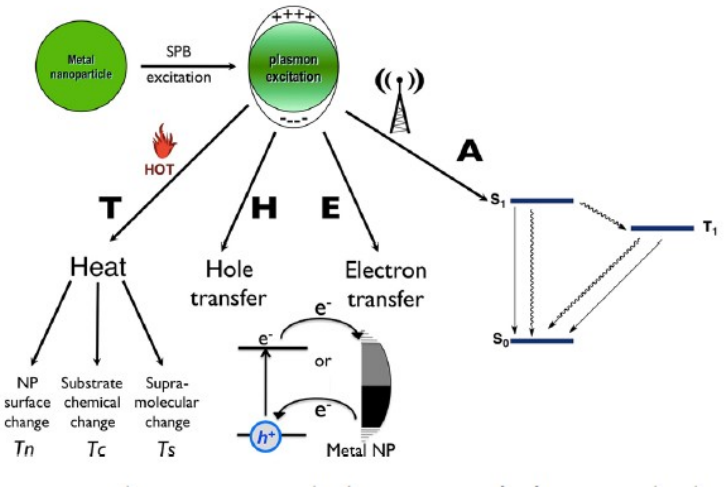

Figure 1.10: Plasmon excitation effects on molecules close to NP surface: A) antenna effect, E) electron transfer, H) hole transfer, and T) thermal effect. Adapted from ref. [20] with permission from Copyright (2017) American Chemical Society.

5. Synthesis of metal nanoparticles

The NP preparation methods are divided into top-down and bottom-up approaches. Top-down method starts with bulk materials that are ablated into smaller units to form NP. Mechanical grinding, physical deposition, laser ablation and electro-explosion are examples of this method.[22-24] On the other hand, during bottom-up approaches, the NP are generated from small units, usually atoms, that are generated (e.g., by redox reactions) and grown to particle size. This thesis is focused in the use of bottom-up methods.

During bottom-up methods, the metal salt (M^{n+}) is reduced into its atomic form (M^0). The process is described by equation 1.7

$$M^{n+} + n\,e^- \rightarrow M^0 \rightarrow\rightarrow\rightarrow MNP \qquad (1.7)$$

The process has been described as shown in Figure 1.11. First, the concentration of M^0 spikes as the precursor M^{+2} is reduced. Once the concentration of M^0 reaches the level of super-saturation (C_{SS}) the atoms start to aggregate and form small clusters through self-nucleation until the concentration of M^0 drop below the level of saturation. Then the nucleation step is terminated and clusters will stop forming. Finally, the clusters keep on growing by consuming M^0 that stayed in solution forming NP. [25]

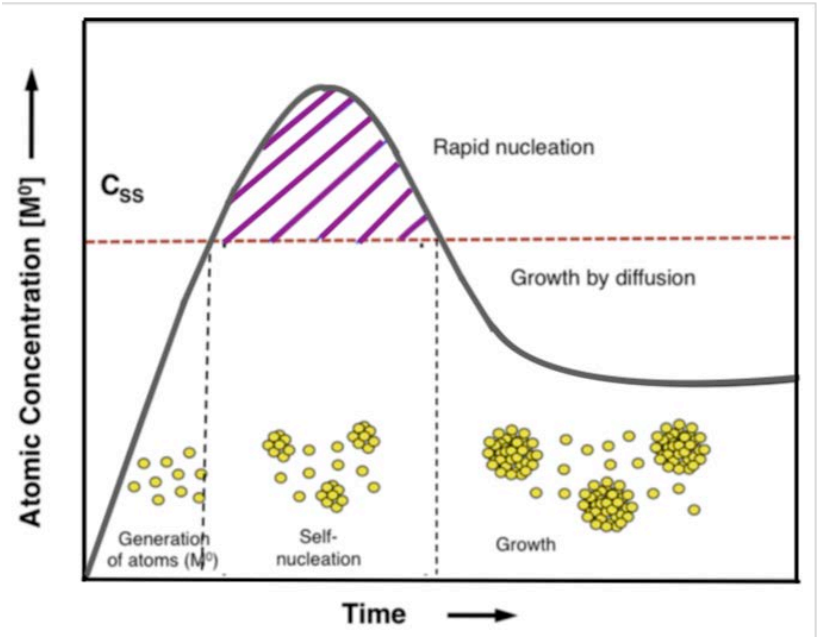

Figure 1.11. LaMer and Dinegar's nucleation mechanism. Adpated from ref. [25]

Particularly for the synthesis of AuNP and AgNP, the most frequently used reducing agent is $NaBH_4$. These NP tend to aggregate easily if they are not stabilized with capping agents, usually organic molecules. The role of the capping agent is preventing the growth of the NP and concomitant aggregation and precipitation. The most common capping agents usually contain N, S and P that bind strongly to the surface of the NP. [26,27,

Photochemical approach

There are a variety of methods that are used to synthesize metal NP,[28-31] but the photochemical method offers many advantages over the other methods. Some of these advantages are spatial and temporal resolution, and synthesis flexibility –thus, tuning the size and shape by altering the irradiation wavelength, intensity and time of irradiation. The photochemical approach utilizes a photosensitizer that acts as the initiator of the photochemical reaction. Norrish type I reaction is the most common method for the photochemical synthesis of the Ag and AuNP. The Norrish type I reaction of a benzoin shown below generates upon UVA irradiation a ketyl radical, a strong reducing agent capable to reduce the metal salt.

The general method for making AuNP in the Scaiano group is shown in Figure 1.12. [32] Briefly, the photochemical synthesis of AuNP involves the use of Irgacure 2959 (I-2959), which generates the 4-hydroxyethoxybenzoyl radical – a precursor for 4-hydroxyethoxybenzoic acid (HEBA) – and the ketyl radical, the reducing agent for the formation of AuNP.

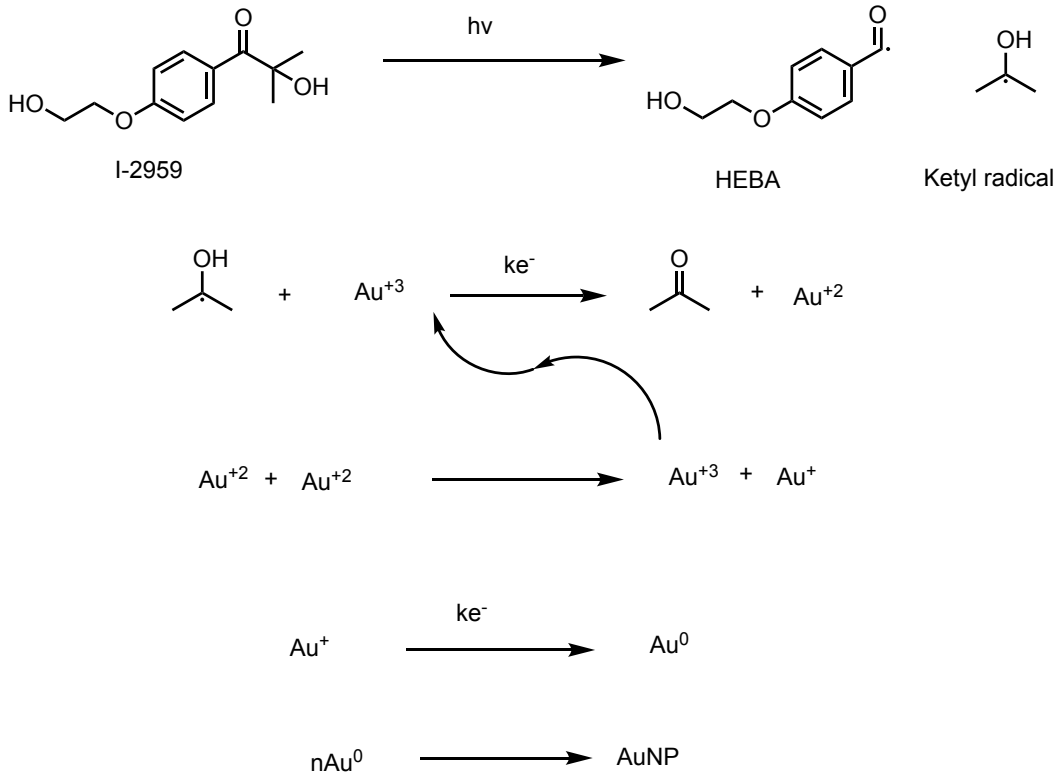

Figure 1.12. General scheme for the photochemical synthesis of AuNP.

Seed mediated method

Despite the presence of many methods to synthesize NP, the seed mediated method remains one of the most efficient due to the high yield of NP generated and ability to control size of the NP. The first step in this approach is to create small NP, which are called seeds by reducing the metal salt using $NaBH_4$. Then growth solution is prepared and the seeds are added to it, allowing them to grow into a specific size. This method has been implemented to synthesise high quality Au nanorods with specific aspect ratio. Different aspect ratio is obtained by manipulating many factors such as concentration of metal, time, and amount of reducing agent. Growth solution for the synthesis of Au nanorods is made of high amount of surfactant (cetyltrimethyl ammonium bromide – CTAB –), Au salt, Ag nitrate and a mild reducing agent. Some important factors for synthesis quality are the age of the seeds, amount of seeds added, amount of reducing agents used, amount of Ag nitrate in growth solution, and temperature. Figure 1.13 shows a representation of the seed mediated method for Au nanorods. [33]

The role of $AgNO_3$ is to control the final aspect ratio of the rods. However its exact role is still under investigation. Some studies claim that a $Ag[BrCTA]_2$ complex is formed and this complex acts as a specific capping agent on the seeds by changing the CTAB micellar structure by silver bromide interaction. [34]

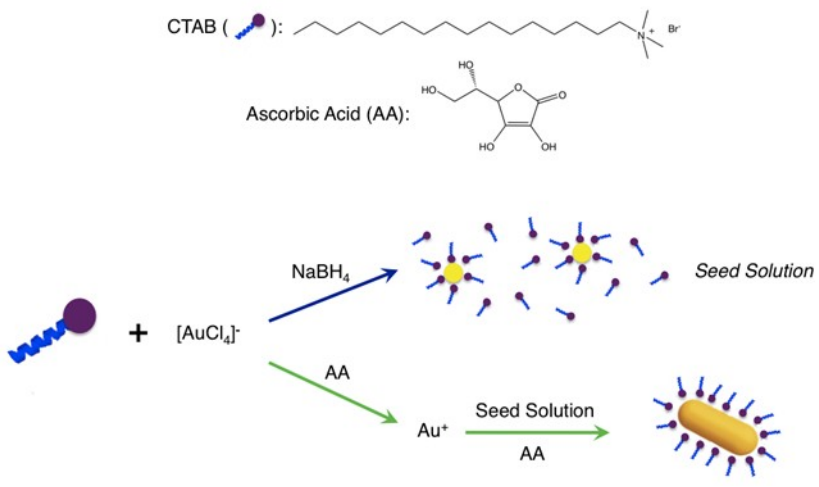

Figure 1.13. Representation of the seed-mediated method for the synthesis of AuNRs. Adapted from ref. [33] with permission from The Royal Society of Chemistry.

6. Nanomaterials Applications

NP are used for biomedical, environmental, technological and catalytic applications. The main focus of this thesis will be on the biomedical and catalytic aspects.

6.1 Biomedical applications

The stability, low toxicity, biocompatibility, and the ability to absorb light and emit energy have made NP useful for biomedical applications such as imaging, drug delivery and therapeutics.[35] Although this thesis is focused on the use of Ag nanstructures for therapeutics, other biomedical applications are briefly described below.

a. Imaging

Semiconductor NP, also known as quantum dots (QD), are great for imaging due to their photostability, narrow emission, and broad excitation wavelength. These photoactive nanomaterials can be used as labels as they produce a strong fluorescent signal. Fluorescent NP are of great promise for imaging because they are bright, have broad range of excitation wavelength and narrow emission bands that can be tuned by controlling the size of the QD. There have been reports about how QD were used to label tumour cells where the divisions of the cancer cell were monitored by the change of fluorescence signal. Even though this method could revolutionize the imaging field as it could offer early detection of cancer, toxicity remains a challenge.[36] Moreover, QD TV's have been commercially available for a few years.

b. Drug delivery

The use of NP as drug carrier became very popular in the 21st century. Some of the attributes that one needs to consider when designing a drug delivery systems are: the system has to have a specific target, low toxicity, and the therapeutic effect of the drug should be unchanged. The system has to be also biocompatible.

Drug delivery offers many advantages such as the ability to control when and where the drug is being released. AuNP are very promising in the field of drug delivery due to special optical, electronic and biochemical properties. AuNP are easily functionalized due to the presence of the negative charge on the surface. In one of the studies a system was designed by making AuNP that are tethered with doxorubicin with poly (ethylene glycol) spacer using acid labile linkage. It was found that as soon as the DOX-tethered AuNP enters acidic media, the drug release was monitored by the monitoring the fluorescence signal. AuNP quenches the fluorescence due to nanosurface energy transfer between the dexorubicinyl groups and gold NP.[37]

c. Therapeutics

The therapeutic applications of NP are countless. One of the biggest breakthroughs is the use of NP to cure cancer. In addition to the use of NP for imaging and carrier of drugs, NP can be used as the therapeutic agents themselves. In recent research, it was reported that functionalizing the AuNP with a protein that has specific binding to the tumour cells and then irradiating the AuNP with near IR light will release local heating, killing the cancer cell. [38]

Another example where NP themselves are used as therapeutic agents is the use of Ag or AuNP as antimicrobial agents. In recent years, the world has been facing a crisis due to the development of antibiotic resistance, which has caused an urgent demand to develop alternatives. Developing coated Ag and AuNP, as an alternative to antibiotics has been the center of NP research over the past decade. In a recent study by the Scaiano group, AuNP coated with amoxicillin have been used as antibacterial agents toward *Staphylococcus aureus*. [39] The main focus of this thesis will be on the use of coated Ag nanostructures as antimicrobial agents toward *Staphylococcus aureus, Escherichia coli, Methicillin-Resistant Staphylococcus aureus (MRSA), and Pseudomona aeruginosa*.

6.2 Catalytic applications

Heterogeneous *vs* homogeneous catalysis

A catalyst is a material that takes part in a chemical reaction facilitating the reaction by interaction with reactants, but remains unchanged after the reaction is completed. The main advantage of using a catalyst is to increase the speed of the reaction by lowering the activation energy, which allows the reaction to occur under milder conditions. The majority of catalysts work based on the principle of thermal mechanism where, after heating, the catalyst uses the thermal energy that is gained to catalyze the reaction toward the desired product. This type of catalysis has low energy efficiency, low selectivity and it is costly.[40] Catalysts can be in two forms, homogeneous and heterogeneous. In homogeneous catalysis the reactant, product and catalyst are all in the same phase, while in heterogeneous catalysis the reaction happens in multiple phases. Figure 1.14 shows the main difference between the homogeneous and heterogeneous catalysts. In heterogeneous catalysis the reactant interacts with the catalyst usually supported on a solid surface. [41]

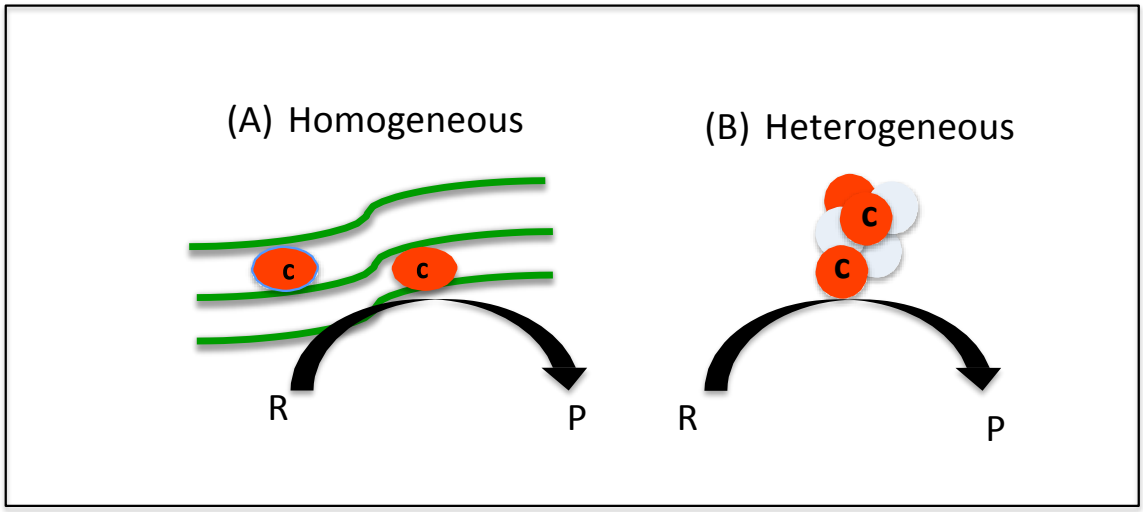

Figure 1.14. Representation of how the reactant interacts with (A) homogeneous and (B) heterogeneous catalysts.

This classification of catalysis into two categories usually overlooks intermediate situations that do not fall into the heterogeneous or homogeneous group. Scaiano has described these particular situations as follows: i) heterogeneous to homogeneous, where the active species can leach and diffuse away from the surface of the heterogeneous material to react in the homogenous phase; ii) homogeneous to heterogeneous catalysis, where the homogeneous catalyst forms insoluble nanostructure complex that acts as in situ heterogeneous catalyst; and iii) heterogeneous to homogeneous and back, where the heterogeneous catalyst releases the active catalytic species that after the catalysis are deposited back on the surface of the catalyst. Figure 1.15. illustrates these three different situations.[41]

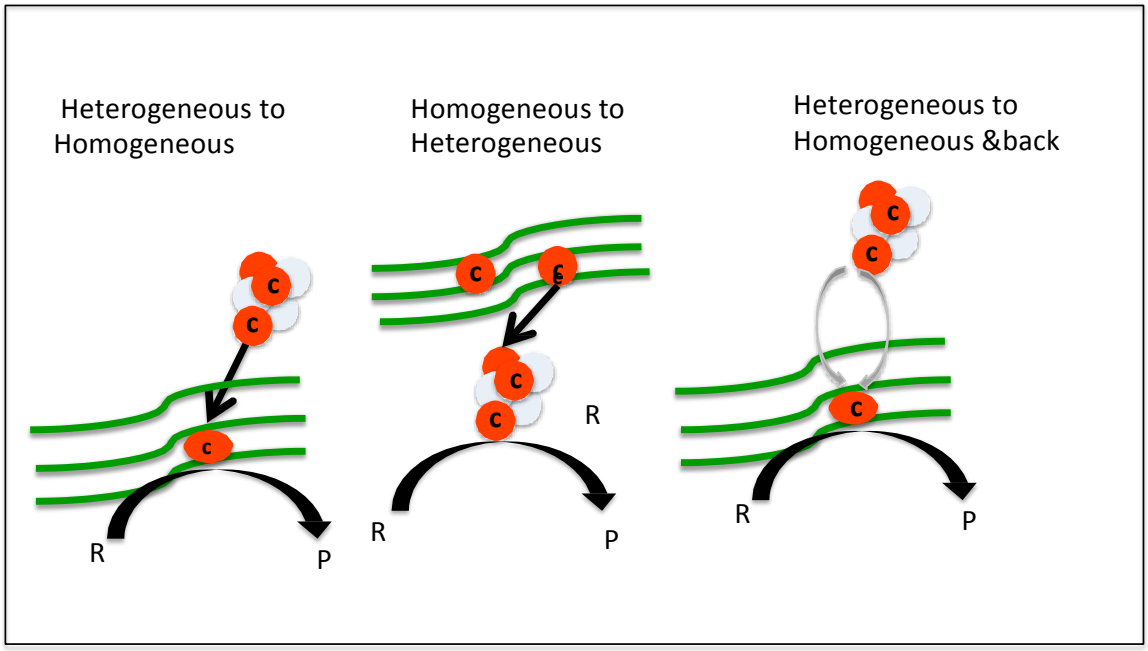

Figure 1.15 Representation of the three types of heterogeneous catalysis and how they interact with the reactant (R) to give product (P).

One of the greatest advantages of using heterogeneous catalysts is the ability to separate and reuse them; making the process more economically and environmentally friendly, desired attributes of Green Chemistry.

Nanocatalysts

NP-based catalysts are widely used in the pharmaceutical industry. [42] Due to their large surface area, NP have become greatly used as catalysts, i.e. more catalytic sites so more reactions can happen simultaneously. NP are greater in size than atoms and smaller than bulk materials, therefore they can be described as a state of matter between bulk and single molecules. When the bulk is reduced to nanometer dimension, the energy bands of the bulk material split into discrete levels, conduction and valence level. The density for material begin to build up from the center of the band and the edges of the electronic band represent the surface states. NP, have lower density of states than the bulk materials and they have higher contribution from the surface state. Therefore, NP have different electronic band structure than the bulk material, which leads to different properties. Figure 1.16 illustrates the difference between NP and the bulk material.[43, 44]

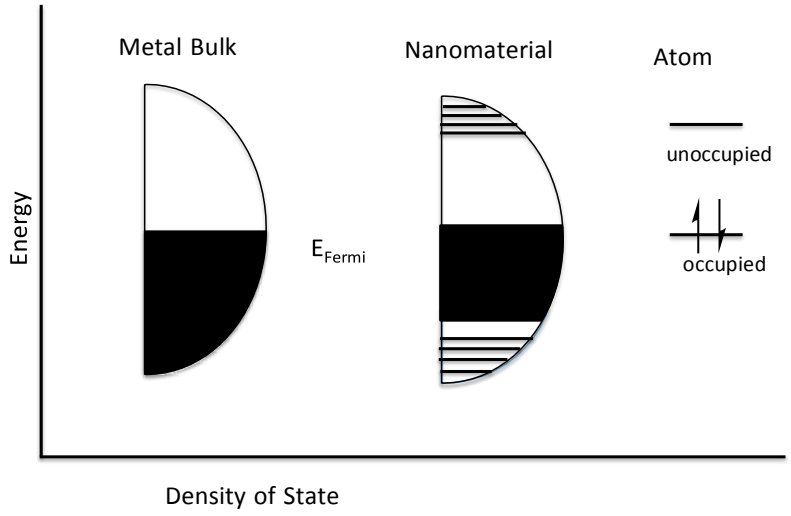

Figure 1.16: Density of states for metal NP compared to those of bulk and of isolated atoms.

The desired attributes for a good catalyst are high activity, selectivity, and stability. There have been reports on the use of NP for many chemical reactions such as dehalogenation, C-C coupling, cyclization and many more. There is also a trend to transform some of the reactions that are catalyzed by NP in the homogeneous phase into the heterogeneous phase. [45-52]

Photocatalysis

Photocatalysis is an active area of research that aims toward performing reactions under milder conditions. In photocatalysis, the reaction is catalyzed through light absorption,i.e. high temperature and high pressure can be avoided. In photocatalysis, the light needs to be absorbed in order to activate the substrate. In order to speed up the reaction, the photocatalyst needs to interact with the substrate in the ground or excited state. Photocatalysts (PC) can also be homogeneous or heterogeneous materials.[49, 53- 59]The main interest in the Scaiano group is to design systems that allow running reactions under milder conditions, where heterogeneous photocatalysts can substitute the use of homogeneous catalysts and harsh reaction conditions.

The photocatalytic mechanism involves the excitation of the PC after absorption of light, which can take two routes to accelerate the reaction:[53] i) energy transfer, which leads to the formation of the excited state of substrate (S) that is easier to oxidize (and to reduce)

than the ground state –scheme 1.1 a–; ii) electron transfer, where the catalyst acts as electron donor or acceptor –scheme 1.1 b.

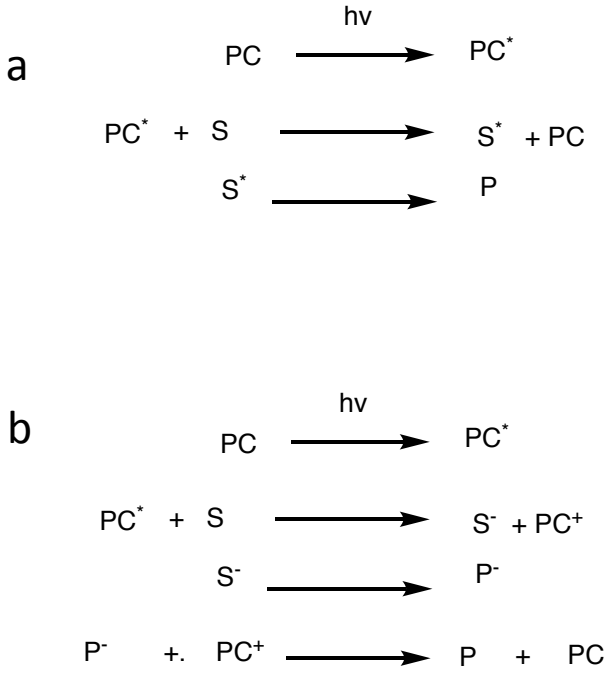

Scheme 1.1. Illustration of the photocatalytic mechanism. a) energy transfer, b) electron transfer. Similar mechanism can be written leading to P^+ and PC^-.

In nature, the most abundant PC that can be found is Chlorophyll. Plants use chlorophyll to absorb sunlight and convert it into chemical energy, thus plants turn water and CO_2 into glucose and O_2 upon absorption of sunlight (Figure 1.17).[54]

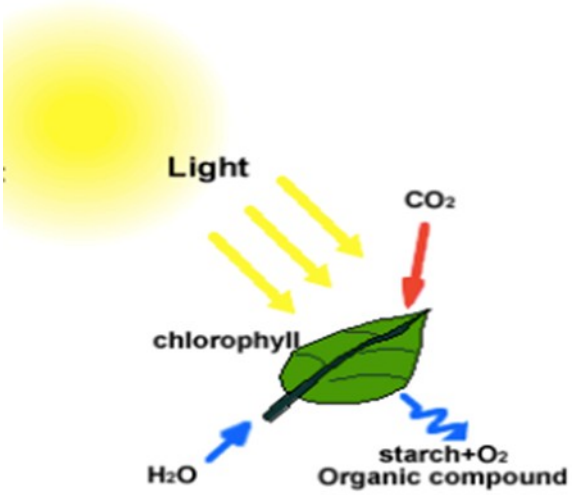

Figure 1.17: Illustration of the photocatalysis of water into O_2 and glucose in the presence of sunlight. Reprinted with permission from.[54]

The most used synthetic heterogeneous photocatalyst is Titanium dioxide (TiO_2), a semiconductor that possesses great stability, low toxicity, high reactivity, and low cost. The major disadvantage for TiO_2 is that it can only absorb light below ~ 400 nm due to its large band gap 3.2eV. Moreover, TiO_2 requires high energy UV irradiation to get activated, so it can make use of 5% of the solar energy on earth, therefore, the potential of using TiO_2 for environmentally sustainable applications is limited. [55]In order to overcome this drawback and make TiO_2 absorb in the visible region, metals were supported on the TiO_2. For example, doping TiO_2 with Pd will lead to great absorption in the visible region as metals provide additional energy levels within the band gap; therefore electron transfer to the conduction band will demand less photon energy. Absorption spectra of TiO_2 and Pd@TiO_2 are shown in figure 1.18.

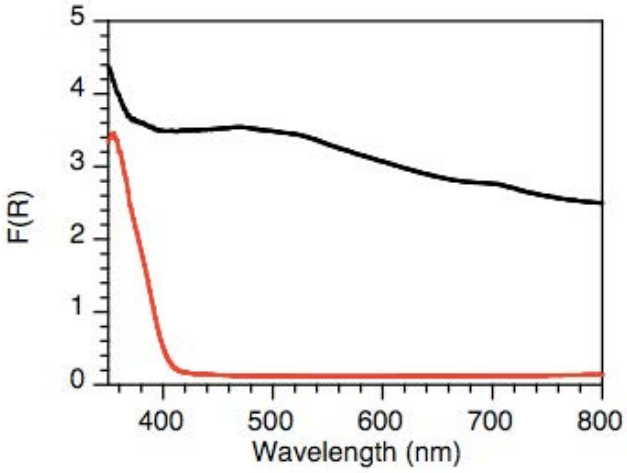

Figure 1.18. Absorption spectra of TiO_2 in red, Pd@TiO_2 in Black.

Figure 1.19, left panel, shows how upon excitation with UV light, TiO_2 electrons move from the valence band to the conduction band creating electron-hole pairs, which are responsible for the oxidation and reduction properties of excited TiO_2. Unfortunately, the electron-hole recombination process occurs rapidly, limiting the catalytic activity of TiO_2. The addition of metal NP, e.g. Pd, onto TiO_2 can introduce an electron capture center that traps the electron, increasing the charge separation and slowing down the electron-hole recombination (Figure 1.19, right panel). This is reflected in the improvement of the photocatalytic activity. [57]

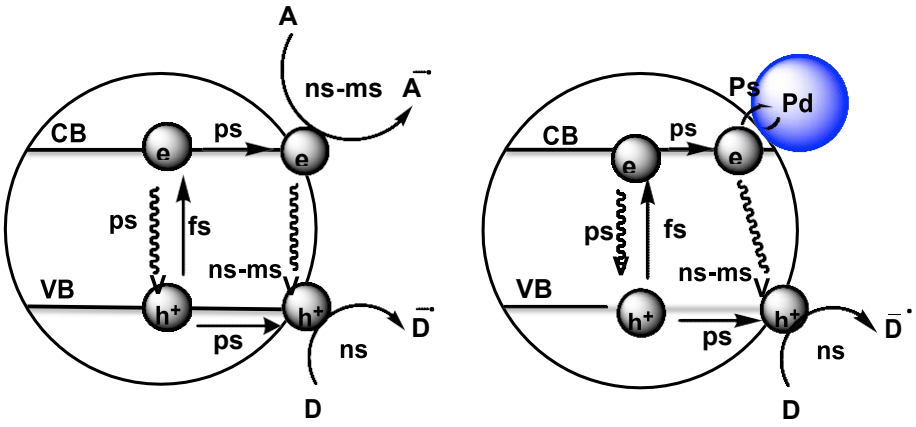

Figure 1.19. Illustration of the electron hole recombination before and after doping TiO_2.

The applications of TiO_2 are countless. TiO_2 is used for catalytic, environmental and health applications. Some of the most important environmental applications of TiO_2 are the photocatalytic production of hydrogen and water treatment.[58] TiO_2 can also be used as self-cleaning service for example; when TiO_2 is added to tiles and paints it provides a self-sterilizing material. These antimicrobial properties of TiO_2 arise from the hydroxyl free radicals that are generated upon excitation of TiO_2 with UV light, these radical convert organic molecules to CO_2 and water and therefore lead to the destruction of the microorganism.[59] Moreover, TiO_2 has been used a photocatalyst or support for catalyst for many reactions. [45-52]

7. Characterization of nanoparticles

There are many techniques used to characterize the various properties of NP. The following section describes the techniques utilized during this thesis.

7.1 Electron Microscopy

Scanning Electron Microscopy

Scanning Electron Microscopy (SEM) allows NP imaging for size and shape characterization. The principle of operation is based on the observation of the electrons that are scattered from the sample after irradiation with an electron beam. Briefly, the sample is deposited on a grid and the electron beam –generated by the electron gun at the top of the microscope– is focused on the surface of the nanomaterial through a set of lenses. Once the electrons interact with the sample the image can be formed by both secondary electrons (SE) emitted from the sample or back scattered electrons (BSE) scattered by the sample. SE gives higher resolution images than BSE as they come from near the surface of the sample. Figure 1.20 summarizes the operation of a SEM. [60]

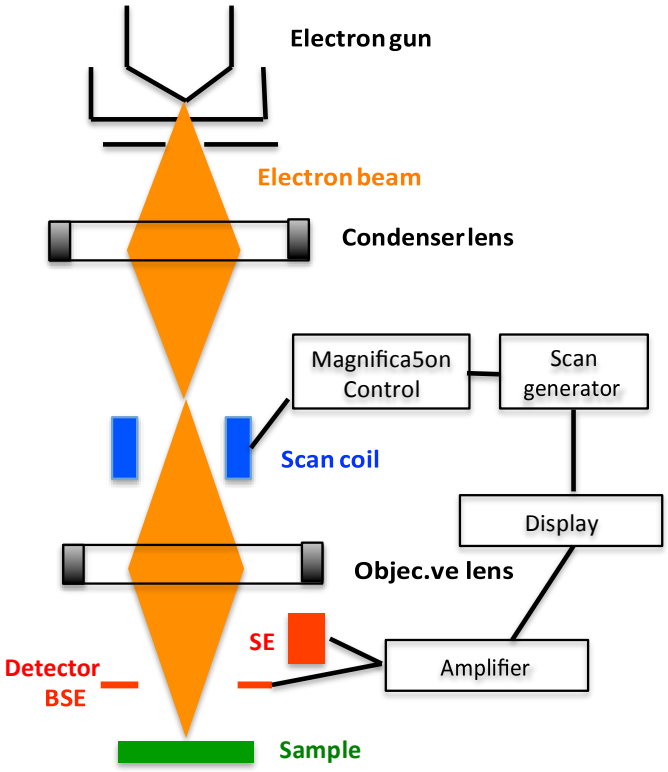

Figure 1.20. Scanning Electron Microscope**.** The generated electron beam is focused on a spot of the sample. The interaction between the electrons and the sample generate an image that is formed by both secondary electrons (SE) emitted from the sample or back-scattered electrons (BSE) scattered by the sample.

Transmission Electron Microscopy

Transmission Electron Microscopy (TEM) operates in a very similar manner compared to SEM. TEM differs from SEM in the following: i) TEM works on the concept of transmitted electrons, it detect primary electrons that are transmitted from the sample; ii) TEM provides sub-nanometer spatial resolution; and iii) the voltage in TEM is much higher than SEM.[61]

7.2 X-ray Photoelectron Spectroscopy

X-ray Photoelectron Spectroscopy (XPS) is the most common surface analysis technique. It gives information about the elemental ratio and bonding nature. It also provides information about the chemical state and electronic state of the element. The analyte is irradiated with X-ray in vacuum, the electron near the surface will be ejected if the energy is sufficient, the emitted electron is used to identify the source of the element. The emitted electron has kinetic energy K_E.[62]

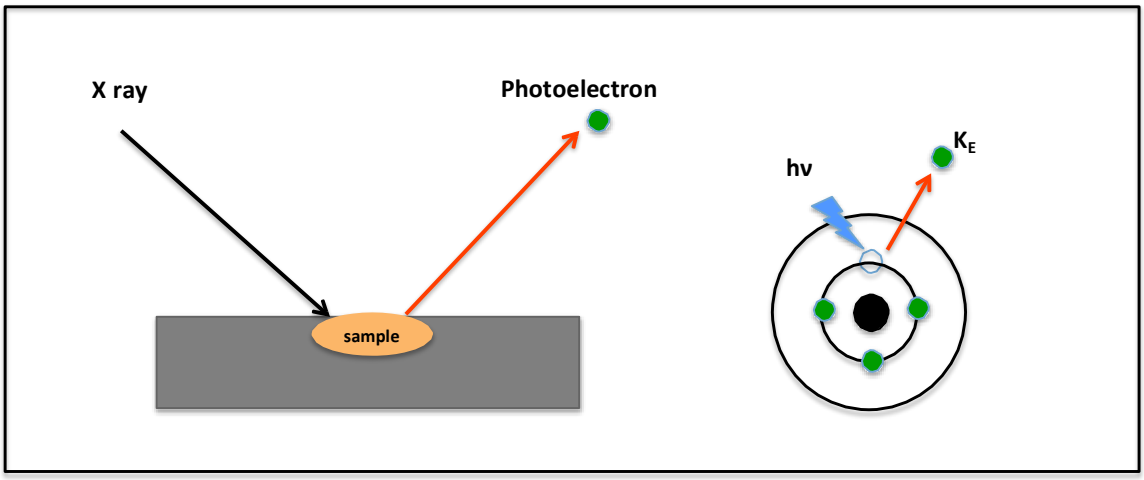

Figure 1.21 Representation of the principle of operation of XPS.

XPS is used to analyze inorganic compounds such as metals and semiconductors. In this thesis XPS was used as a technique to learn about the oxidation state of metals such as Pd, Cu and Au.

7.3 Inductively coupled plasma optical emission spectroscopy

Inductively coupled plasma optical emission spectroscopy (ICP-OES) is a method that is used to determine the metal concentration in a sample. It operates based on the following concept, the torch plasma will ionize the sample into ions which lead to excitation of the atoms. When the atoms relax to low energy level they emit at wavelengths that are characteristic to a specific element. The concentration of the element is related to the intensity of the emission.[63]

7.4 Diffuse reflectance spectroscopy

Diffuse reflectance (DR) spectroscopy is used to analyze the optical properties of solid samples. Since light cannot penetrate opaque samples, DR is used to determine the absorption profile of the material. Thus, the sample is irradiated with polychromatic light inside of an integrating sphere (a sphere made of totally reflective material) and only the light that is reflected from the sample (not absorbed) is reaching the detector (Figure 1.22).[64] The DR spectrum can be used to determine the semiconductor band gap using the Kubelka Function. The relation between absorption coefficient and band gap energy is giving in the following equation

$$\alpha h\nu^{\frac{1}{2}} = A(h\nu - E_g)$$

where α is absorption coefficient, *v* is light frequency, A proportionality constant , E_g is the band gap energy.

Plotting $\alpha h\nu^{1/2}$ vs $h\nu$ allows the evaluation of the band gap energy by plotting the straight line to the axis intercept. [65]

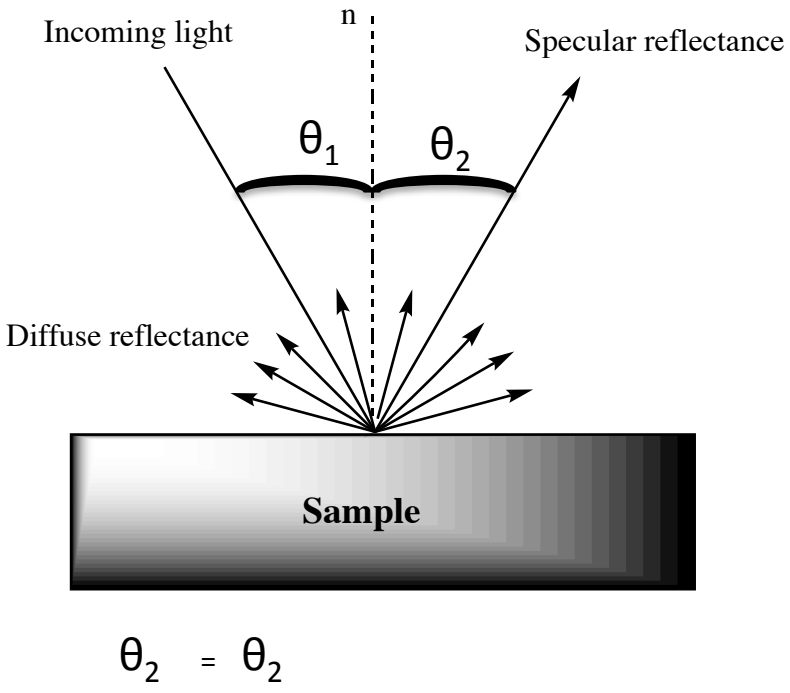

Figure 1.22. Presentation of the working principle of DR. Reflection includes two components: specular and diffuse. Specular reflectance is the mirror like reflection of the sample surface. Diffuse reflectance happens when the surface reflects light in different directions

References

1. Maynard, A. D., Don't define nanomaterials. *Nature* **2011,** *475* (7354), 31.
2. Nikalje, A., Nanotechnology and its Applications in Medicine. *Med Chem* **2015,** *5*, 5:081-089.
3. Freestone, I.; Meeks, N.; Sax, M.; Higgitt, C., The Lycurgus Cup — A Roman nanotechnology. *Gold Bull* **2007,** *40* (4), 270-277.
4. Leonhardt, U., Invisibility cup. *Nat. Photonics* **2007,** *1*, 207.
5. Anon History and Development of Nanomaterials. https://www.azonano.com/article.aspx?ArticleID=3393 (accessed March 2018).

6. Tiwari, J. N.; Tiwari, R. N.; Kim, K. S., Zero-dimensional, one-dimensional, two-dimensional and three-dimensional nanostructured materials for advanced electrochemical energy devices. *Prog Mater Sci* **2012,** *57* (4), 724-803.

7. Tana, T.; Guo, X. W.; Xiao, Q.; Huang, Y.; Sarina, S.; Christopher, P.; Jia, J.; Wu, H.; Zhu, H., Non-plasmonic metal nanoparticles as visible light photocatalysts for the selective oxidation of aliphatic alcohols with molecular oxygen at near ambient conditions. *Chem Commun* **2016,** *52* (77), 11567-70.

8. Hashimoto, Y.; Seniutinas, G.; Balčytis, A.; Juodkazis, S.; Nishijima, Y., Au-Ag-Cu nano-alloys: tailoring of permittivity. *Sci Rep* **2016,** *6*, 25010.
9. Stryer, L., Fluorescence energy transfer as a spectroscopic ruler. *Annu Rev Biochem* **1978,** *47*, 819-46.

10. Liang, Z.; Sun, J.; Jiang, Y.; Jiang, L.; Chen, X., Plasmonic enhanced optoelectronic devices. *Plasmonics* **2014,** *9* (4), 859-866.
11. Juan, M. L.; Righini, M.; Quidant, R., Plasmon nano-optical tweezers. *Nat Photonics* **2011,** *5*, 349.
12. Kreibig, U.; Vollmer, M., *Optical Properties of Metal Clusters.Springer Verslg:Berlin Heidelberg,* 1995; Vol. 25.
13. L. Dmitruk, N.; Korovin, A., *Physical nature of anomalous optical transmission of thin absorptive corrugated films*. Jetp Lett **2009,** 89, 68-72.

14. Liau, Y. H.; Egusa, S.; Scherer, N. F., Ultrafast interferometric measurements of plasmonic transport in photonic crystals. *Opt Lett* **2002,** *27* (10), 857-9.

15. Guler, U.; Turan, R., Effect of particle properties and light polarization on the plasmonic resonances in metallic nanoparticles. *Opt Express* **2010,** *18* (16), 17322-38.

16. Gold Nanoparticle Properties. http://www.cytodiagnostics.com/store/pc/Gold-Nanoparticle-Properties-d2.html (accessed March 8, 2018).
17. Marquez, D. T.; Scaiano, J. C., Plasmon induced self-assembly of gold nanorods in polymer films. *Chem Commun* **2015,** *51* (10), 1911-3.

18. Pérez-Juste, J.; Rodríguez-González, B.; Mulvaney, P.; Liz-Marzán, L. M.,

Optical Control and Patterning of Gold-Nanorod–Poly(vinyl alcohol) Nanocomposite Films. *Adv Funct Mater* **2005,** *15* (7), 1065-1071.

19. Stamplecoskie, K. G.; Scaiano, J. C., Silver as an example of the applications of photochemistry to the synthesis and uses of nanomaterials. *Photochem Photobiol* **2012,** *88* (4), 762-8.

20. Scaiano, J. C.; Stamplecoskie, K., Can Surface Plasmon Fields Provide a New Way to Photosensitize Organic Photoreactions? From Designer Nanoparticles to Custom Applications. *J Phys Chem Lett* **2013,** *4* (7), 1177-87.
21. Fasciani, C.; Bueno Alejo, C. J.; Grenier, M.; Netto-Ferreira, J. C.; Scaiano, J. C., High-temperature organic reactions at room temperature using plasmon excitation: decomposition of dicumyl peroxide. *Org Lett* **2011,** *13* (2), 204-7.
22. Petroski, J. M.; Wang, Z. L.; Green, T. C.; El-Sayed, M. A., Kinetically Controlled Growth and Shape Formation Mechanism of Platinum Nanoparticles. *J Phys Chem B* **1998,** *102* (18), 3316-3320.
23. Yu; Chang, S.-S.; Lee, C.-L.; Wang, C. R. C., Gold Nanorods: Electrochemical Synthesis and Optical Properties. *J Phys Chem B* **1997,** *101* (34), 6661-6664.

24. Scaiano, J. C.; Stamplecoskie, K. G.; Hallett-Tapley, G. L., Photochemical Norrish type I reaction as a tool for metal nanoparticle synthesis: importance of proton coupled electron transfer. *Chem Commun* **2012,** *48* (40), 4798-808.
25. LaMer, V. K.; Dinegar, R. H., Theory, Production and Mechanism of Formation of Monodispersed Hydrosols. *J Am Chem Soc* **1950,** *72* (11), 4847-4854.
26. Gandubert, V. J.; Lennox, R. B., Assessment of 4-(Dimethylamino)pyridine as a Capping Agent for Gold Nanoparticles. *Langmuir* **2005,** *21* (14), 6532-6539.

27. Mirkhalaf, F.; Paprotny, J.; Schiffrin, D. J., Synthesis of Metal Nanoparticles Stabilized by Metal−Carbon Bonds. *J Am Chem Soc* **2006,** *128* (23), 7400-7401.

28. Schmid, G.; Corain, B., Nanoparticulated Gold: Syntheses, Structures, Electronics, and Reactivities. *Eur J Inorg Chem* **2003,** *2003* (17), 3081-3098.
29. Yonezawa, T.; Kunitake, T., Practical preparation of anionic mercapto ligand-stabilized gold nanoparticles and their immobilization. *Colloids Surf A: Physicochem Eng Asp* **1999,** *149* (1), 193-199.

30. Waters, C. A.; Mills, A. J.; Johnson, K. A.; Schiffrin, D. J., Purification of dodecanethiol derivatised gold nanoparticles. *Chem Commun* **2003,** (4), 540-1.

31. Daniel, M. C.; Astruc, D., Gold nanoparticles: assembly, supramolecular chemistry, quantum-size-related properties, and applications toward biology, catalysis, and nanotechnology. *Chem Rev* **2004,** *104* (1), 293-346.
32. C. Scaiano, J.; Stamplecoskie, K.; McGilvray, K.; Pacioni, N., *A Paradigm for the Radical-Mediated Photochemical Synthesis of Metal Nanostructures*.In Encylopedia of Radical in Chemistry, Biology and Materials 2012.

33. Chen, H.; Shao, L.; Li, Q.; Wang, J., Gold nanorods and their plasmonic properties. *Chem Soc Rev* **2013,** *42* (7), 2679-724.

34. Hinman, J. G.; Stork, A. J.; Varnell, J. A.; Gewirth, A. A.; Murphy, C. J., Seed mediated growth of gold nanorods: towards nanorod matryoshkas. *Faraday Discuss* **2016,** *191* (0), 9-33.
35. Choi, H. S.; Frangioni, J. V., Nanoparticles for Biomedical Imaging: Fundamentals of Clinical Translation. *Molecular imaging* **2010,** *9* (6), 291-310.

36. Pericleous, P.; Gazouli, M.; Lyberopoulou, A.; Rizos, S.; Nikiteas, N.; Efstathopoulos, E. P., Quantum dots hold promise for early cancer imaging and detection. *Int J Cancer* **2012,** *131* (3), 519-28.

37. Wang, F.; Wang, Y. C.; Dou, S.; Xiong, M. H.; Sun, T. M.; Wang, J., Doxorubicin-tethered responsive gold nanoparticles facilitate intracellular drug delivery for overcoming multidrug resistance in cancer cells. *ACS Nano* **2011,** *5* (5), 3679-92.

38. Jain, P. K.; El-Sayed, I. H.; El-Sayed, M. A., Au nanoparticles target cancer. *Nano Today* **2007,** *2* (1), 18-29.

39. Silvero C, M. J.; Rocca, D. M.; de la Villarmois, E. A.; Fournier, K.; Lanterna, A. E.; Pérez, M. F.; Becerra, M. C.; Scaiano, J. C., Selective Photoinduced Antibacterial Activity of Amoxicillin-Coated Gold Nanoparticles: From One-Step Synthesis to in Vivo Cytocompatibility. *ACS Omega* **2018,** *3* (1), 1220-1230.

40. Loizou, A. Advantages and disadvantages of Catalysts in Industrial Reactions. https://getrevising.co.uk/grids/catalysts (accessed April 2018).

41. Scaiano, J. C.; Lanterna, A. E., Is Single-Molecule Fluorescence Spectroscopy Ready To Join the Organic Chemistry Toolkit? A Test Case Involving Click Chemistry. *J Org Chem* **2017,** *82* (10), 5011-5019.

42. Jiang, C.; Jia, J.; Zhai, S., Mechanistic Understanding of Toxicity from Nanocatalysts. *Int J Mol Sci* **2014,** *15* (8), 13967-13992.

43. Alivisatos, A. P., Perspectives on the Physical Chemistry of Semiconductor Nanocrystals. *J Phys Chem* **1996,** *100* (31), 13226-13239.

44. Oleg, A. Y. a. I. M. D. a. A. A. A. a. A. V. K., Surface plasmon as a probe for melting of silver nanoparticles. *Nanotechnology* **2010,** *21* (4), 045203.

45. Crites, C.-O. L.; Netto-Ferreira, J. C.; Hallett-Tapley, G. L.; Scaiano, J. C., AuNP@TiO_2 Catalyzed Peroxidation of Ethyl- and n-Propylbenzene: Exploring the Interaction Between Radical Species and the Nanoparticle Surface. *J Braz Chem Soc* **2016,** *27*, 334-340.

46. Dos Santos, C. G.; Marquez, D. T.; Crites, C.-O. L.; Netto-Ferreira, J. C.; Scaiano, J. C., Plasmon heating mediated Friedel-Crafts alkylation of anisole using supported AuNP@Nb_2O_5 catalysts. *Tetrahedron Lett* **2017,** *58* (5), 427-431.

47. Elhage, A.; Lanterna, A. E.; Scaiano, J. C., Light-Induced Sonogashira C–C Coupling under Mild Conditions Using Supported Palladium Nanoparticles. *ACS Sustainable Chem Eng* **2018,** *6* (2), 1717-1722.

48. Lanterna, A. E.; Elhage, A.; Scaiano, J. C., Heterogeneous photocatalytic C-C coupling: mechanism of plasmon-mediated reductive dimerization of benzyl bromides by supported gold nanoparticles. *Catal Sci Technol* **2015,** *5* (9), 4336-4340.

49. Elhage, A.; Lanterna, A. E.; Scaiano, J. C., Tunable Photocatalytic Activity of Palladium-Decorated TiO_2: Non-Hydrogen-Mediated Hydrogenation or Isomerization of Benzyl-Substituted Alkenes. *ACS Catalysis* **2017,** *7* (1), 250-255.

50. McTiernan Christopher, D.; Pitre Spencer, P.; Ismaili, H.; Scaiano Juan, C., Heterogeneous Light-Mediated Reductive Dehalogenations and Cyclizations Utilizing Platinum Nanoparticles on Titania (PtNP@TiO_2). *Adv Synth Catal* **2014,** *356* (13), 2819-2824.

51. Pitre, S. P.; Yoon, T. P.; Scaiano, J. C., Titanium dioxide visible light photocatalysis: surface association enables photocatalysis with visible light irradiation. *Chem Commun* **2017,** *53* (31), 4335-4338.

52. Wang, B.; Durantini, J.; Nie, J.; Lanterna, A. E.; Scaiano, J. C., Heterogeneous Photocatalytic Click Chemistry. *J Am Chem Soc* **2016,** *138* (40), 13127-13130.

53. Castellote, M.; Bengtsson, N., Principles of TiO2 Photocatalysis. In *Applications*

of Titanium Dioxide Photocatalysis to Construction Materials: State-of-the-Art Report of the RILEM Technical Committee 194-TDP, Ohama, Y.; Van Gemert, D., Eds. Springer Netherlands: Dordrecht, 2011; pp 5-10.
54. What is Photocatalyst? http://www.greenearthnanoscience.com/what-is-photocatalyst.php (accessed March 11, 2018).

55. Kuvarega, A. T.; Mamba, B. B., TiO_2-based Photocatalysis: Toward Visible Light-Responsive Photocatalysts Through Doping and Fabrication of Carbon-Based Nanocomposites. *Crit Rev Solid State Mater Sci* **2017,** *42* (4), 295-346.
56. Linsebigler, A. L.; Lu, G.; Yates, J. T., Photocatalysis on TiO_2 Surfaces: Principles, Mechanisms, and Selected Results. *Chem Rev* **1995,** *95* (3), 735-758.
57. Schneider, J.; Matsuoka, M.; Takeuchi, M.; Zhang, J.; Horiuchi, Y.; Anpo, M.; Bahnemann, D. W., Understanding TiO2 photocatalysis: mechanisms and materials. *Chem Rev* **2014,** *114* (19), 9919-86.
58. Hainer, A. S.; Hodgins, J. S.; Sandre, V.; Vallieres, M.; Lanterna, A. E.; Scaiano, J. C., Photocatalytic Hydrogen Generation Using Metal-Decorated TiO_2: Sacrificial Donors vs True Water Splitting. *ACS Energy Lett* **2018,** *3* (3), 542-545.
59. Photocatalysis Application of TiO_2. http://www.titaniumart.com/photocatalysis-ti02.html (accessed April 2018).
60. Microscopic techniques http://nptel.ac.in/courses/102103015/module3/lec2/2.html (accessed March 11, 2018).
61. 12 Differences between Scanning Electron Microscope and Transmission Electron Microscope (SEM vs TEM). https://www.majordifferences.com/2016/08/difference-between-sem-and-tem.html -

.Wqh0pWbMzEa (accessed March 11, 2018).
62. X-ray Photoelectron Spectroscopy. https://web.statler.wvu.edu/~wu/mae649/xps.pdf (accessed March 11, 2018).

63. Principle of ICP Optical Emission Spectrometry (ICP-OES). https://www.hitachi-hightech.com/global/products/science/tech/ana/icp/descriptions/icp-oes.html (accessed April 2018).
64. http://www.nuance.northwestern.edu/docs/keckii-pdf/what-is-diffuse-reflectance-spectroscopy.pdf (accessed March 11, 2018).
65. Jiao, Z.; Chen, T.; Xiong, J.; Wang, T.; Lu, G.; Ye, J.; Bi, Y., Visible-light-driven photoelectrochemical and photocatalytic performances of Cr-doped $SrTiO_3/TiO_2$ heterostructured nanotube arrays. *Sci Rep* **2013,** *3*, 2720.

Chapter 2
Bactericidal properties of silver nanostructures coated by small biomolecules. A persuasive case for the benefits of polymorphic and polydisperse nanomaterial compositions

2.1. Medical application of silver nanoparticles

In 1928, Alexander Fleming discovered the first antibiotic, which is known as Penicillin. Penicillin has saved millions of lives. In the 1900s, the major cause of death was infectious diseases such as Pneumonia, while after the discovery of the first antibiotic the leading cause of death became heart diseases. Shortly after, the problem of antibiotic resistance started to emerge and this forced the pharmaceutical companies to rush into developing a new beta lactam antibiotic such as Methicillin.

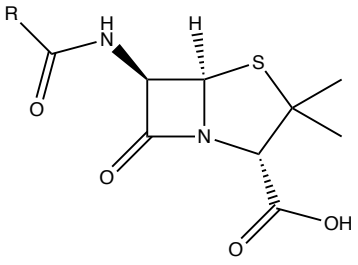

Penicillin

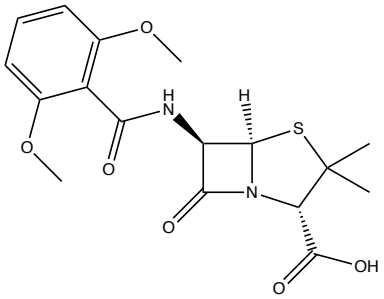

Methicillin

Despite all efforts, in 1968 the first case of methicillin-resistant *Staphylococcus aureus* (*MRSA*) was discovered. *MRSA* is known to kill more people than HIV, Parkinson and homicide combined. There was a great effort to develop new antibiotics between the period of 1960 and 1980.[3] Then the trend to develop new antibiotic drugs decreased due to diminished economic motivation and extensive regulation. The lack of development of new antibiotics has led to a health crisis when it comes to antimicrobial treatment.[4] Some of the factors that lead to antibiotic resistance are, the random use of antibiotics, the prescription of antibiotics for viral infections, and bacteria that is known not to be treated by antibiotics, the extreme use of

antibiotics for agriculture purposes and the lack of regulation for obtaining antibiotics especially in developing countries. There are two kinds of bacterial resistance to antibiotics; the first kind is intrinsic resistance where the bacteria is naturally resistant to the antibiotic, for instance gram negative bacteria are intrinsically resistant to Vancomycin, a well known antibiotic. The other type is acquired resistance where the bacterial cell gains the resistance to antibiotics by mutation, i.e. changing their outer structures where antibiotics will not be able to bind to the bacteria. Mutation could occur due to natural or induced methods. Natural causes of mutation are due to the very rapid rate of bacterial multiplication. Bacteria double every 20 minutes which translates to 30 times multiplication in 10 hours. During multiplication the DNA need to be duplicated by a process called DNA replication that is catalyzed by the enzyme polymerase III. Due to the fast rate of duplication, the enzyme can have some error when connecting the nucleic acid, which could cause mutation in the DNA, and therefore resistance. On the other hand, the induced method involves the inappropriate use of antibiotics. When the right amount of antibiotic is used, the bacteria will die; however, if the concentration of antibiotic is below the lethal dose, reactive oxygen species (ROS) will be generated which lead to mutation of the organism's DNA. In other words, ROS tend to increase the mutagenesis rate in organisms; therefore, the genetic information of bacteria is changed and the antibiotic will be ineffective toward the bacteria. [5]

The government has taken some steps to control the antibiotic crisis such as regulating the prescriptions of antibiotics and educating people about the crisis.[6-8] However, these efforts are not sufficient to put an end to the crisis. There remains an urgent demand for the development of novel antimicrobial therapies to treat infections that are caused by resistant and non–resistant bacteria.[9-11]

Silver has been known as an antimicrobial agent for a very long time. Hippocrates reported the use of silver to cure wounds, also the ancient Romans stored water in silver bottles. In 1884, a silver solution of $AgNO_3$ was first applied to a newborn's conjunctiva in order to prevent maternal transmission of *Neisseria gonorrhoeae*. Silver has been used in implants such as cardiac valves, and is also used in toothpaste, baby products, surgical equipment, wound care products and food storage. [12-15] On the other hand, silver nanoparticles (AgNP) are known to have a broad antimicrobial effect for over 650 strains of bacteria and viruses and to be non-toxic at small concentration toward the human body. As mentioned in the previous chapter, the properties of nanoparticles outperform the bulk material of the same metal.[16] The mechanism behind the ability of AgNP to inhibit bacteria remains under investigation.[17] Some of the proposed mechanisms include the ability of silver ion (Ag^+) to bind to the thiol group in the enzyme of the bacterial respiratory chain leading to the production of large amounts of ROS which promote cell death. Silver ions also increase the permeability of the cell

membrane allowing the silver ion to penetrate the cell wall, changing its structure and therefore leading cell death.[18, 19] On the other hand, the Scaiano group has demonstrated that AgNP outperform the role of silver ion as antimicrobial agents.[13] This proved that the antimicrobial properties of AgNP do not rely only on the release of silver ions and that they work through a different mechanism. The Scaiano group also demonstrated that the use of non-toxic and inexpensive materials such as sweeteners to increase the antimicrobial activity of AgNP and AuNP.[20]

AgNP can be synthesized by many different method which can result in different NP shape and size, changing their plasmonic properties,[21] and as a result changing the antimicrobial activity.[22, 23] In this chapter we demonstrate how sweetener and small molecule-coated polymorphic AgNS can inhibit the growth of common bacteria: *Staphylococcus aureus*, *Escherichia coli*, *Methicillin-Resistant Staphylococcus aureus* (MRSA), and *Pseudomona aeruginosa*. The minimum inhibition concentrations (MICs) and minimal biofilm eradication concentration ($MBEC_{80}$) based on silver content for the planktonic and biofilm assays are also reported. MIC is the lowest concentration of antibiotic that is needed to inhibit the bacterial growth in planktonic testing where the bacteria float and are not adhered to any surface. In planktonic testing the bacteria is incubated with the antibiotic at the same time. However $MBEC_{80}$ is the lowest concentration that is needed to eradicate 80% of biofilms. In biofilms the bacteria adhere to non-biological surfaces in wet environments. Biofilm is considered a protective mode for bacteria that achieve organism survival in harsh environments. In biofilm testing the biofilm is allowed to form before the antibiotic is introduced. [24]

The small molecules that are used are aspartame, sorbitol, sucralose and glucosamine. Glucosamine is not a sweetener but for the ease of use it will be referred to as a sweetener.

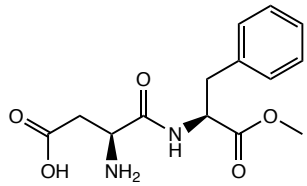

Aspartame

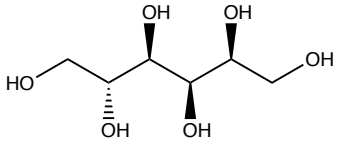

Sorbitol

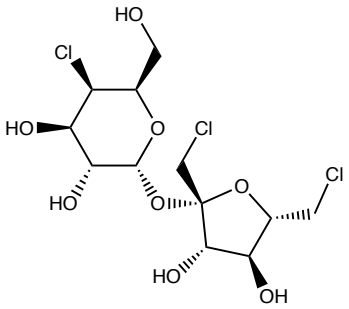

Sucralose

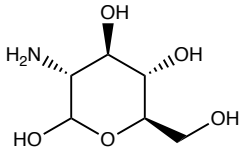

Glucosamine

The work shows how highly polydisperse and polymorphic nanostructures can be an asset rather than a disadvantage, simply because bacteria appear not to be able to adapt quickly to the multiple shapes of silver nanostructures (AgNS), facilitating the efforts in terms of synthesis and stabilization of AgNP. The surface protection with glucosamine and the various sweeteners tested has proven to lead to excellent particle stabilization in aqueous media and prolonged shelf life stability.[25, 26]

This project has been done in collaboration with summer student Caitlin Lazurko, Dr. Daniela Marquez (Department of Chemistry and Biomolecular Sciences and Centre for Advanced Materials Research, University of Ottawa), Dr. Jazmin Silvero (Department of Pharmaceutical Sciences, Faculty of Chemistry, National University of Cordoba-Argentina), Dr. Robert Slinger (Infectious Diseases/Medical Microbiology, Children's Hospital of Eastern Ontario) and under the supervision of Dr. Shaun Kilty (Department of Otolaryngology–Head and Neck Surgery, The Ottawa Hospital, University of Ottawa) and Dr. Juan Scaiano (Department of Chemistry and Biomolecular Sciences and Centre for Advanced Materials Research, University of Ottawa).

The work described in this chapter is the result of the efforts done by all people mentioned above. For completeness, I will include all the results in this thesis specifying who performed the experimental work. Thus, whereas I was in charge of the synthesis of coated silver nanoparticles and nanoplates and their characterization by SEM, TEM and UV- VIS, as well as the testing of bactericidal properties of sweeteners alone; synthesis of coated AgNS and their bactericidal properties were tested in collaboration with Caitlin Lazurko. She also

determined the gold nano-rods and silver nanoparticles bactericidal properties. Dr. Daniela Marquez did the synthesis of gold nanorods and characterized them by TEM, UV-VIS and Zeta potential. She also offered training for Caitlin Lazurko and me on the synthesis of the nanostructures. Dr. Jazmin Silvero and Caitlin Lazurko carried out the Hemolysis Test. Dr. Jazmin Silvero offered training for me and Caitlin Lazurko on the proper way of testing the bactericidal properties. Dr. Robert Slinger offered training on plating bacteria, and testing them at the Children's Hospital of Eastern Ontario.

2.2. Synthesis of silver nanostructures

Silver nanostructures (AgNS) have been used for wide range of applications such as biomedical, catalysis, and environmental. Synthesizing AgNS that are suitable for a specific application remains a challenge as different shapes, size and capping lead to completely different activity. This challenge has led scientists to work on developing different synthetic strategies to be able to control the size and shape of the AgNS. The most widely used methods are the photochemical approach and the seed mediated growth method described in the previous chapter. The seed mediated method remains as the most common way of synthesis for AgNS due to its ease and ability to control size and shape. The seed mediated method is considered bottom to top approach as it is based on the chemical reduction of the metal salt using a reducing agent. We have studied the antibacterial properties of coated AgNS that were synthesized by the seed mediated method.

2.2.1. Experimental

Reagents

Sodium borohydride ($NaBH_4$, 99%), silver nitrate ($AgNO_3$, >99%), ascorbic acid (99%), hexadecyltrimethylammonium bromide (C_{16}TAB, 96%), and sodium hydroxide (NaOH), sucralose, D-(+)-glucosamine hydrochloride, sorbitol, and aspartame were purchased from Sigma-Aldrich and used as received without further purification. Aqueous solutions were prepared using 18.2 MΩ cm^{-1} Milli-Q water obtained from a Millipore System equipped with a 0.22 μm filter. Mueller Hinton broth was used to prepare the planktonic and biofilm tests.

Synthesis of uncoated silver nanostructures

AgNS were synthesized based on a seed-mediated method reported by Hormozi-Nezhad *et al*.[27 28, 29] The seed solution was made by adding 5 mL of $AgNO_3$ (0.25 mM) to 15 mL of sodium citrate (0.25 mM). Next, a total of 0.6 mL of ice cold $NaBH_4$ (0.01 M) was added gradually in aliquots of 100 μL every 10 minutes. The solution was kept undisturbed for two hours at room temperature. Next, a growth solution was prepared by the successive addition of

0.25 mL $AgNO_3$ (10 mM), 0.50 mL of ascorbic acid (7.2 mM) to 9.5 mL of CTAB (0.05 M). Finally, 125 μL of seed solution were added into the growth solution immediately followed by addition of 0.1 mL of NaOH (1.00 M). The mixture was stirred for two days. Excess surfactant was removed by centrifugation (11,000 rpm; 10 min) and then the AgNS were resuspended in 2.5 mL of water.

Synthesis of coated silver nanostructures

Sweetener coated AgNS were prepared following a procedure similar to the synthesis of the uncoated AgNS. The sweetener was incorporated in the synthesis by mixing the corresponding sweetener and $NaBH_4$ in 10mL of Milli-Q water in order to obtain final concentrations of 1 mM and 0.01 mM, respectively. Four types of sweeteners –aspartame, sucralose, sorbitol and glucosamine– were used as coating agents for the AgNS.

Synthesis of coated silver nanoparticles

Silver nanoparticles (AgNP) were synthesized using a simple bench-top protocol [30] with some modification; $NaBH_4$ (aq) was used as the reducing agent and aspartame (Asp), glucosamine (GlcN) and sucralose (Suc) as the stabilizers. All glassware were cleaned by soaking in H_2O_2:H_2SO_4 (1:3). AgNP@Asp were synthesised as follows: 15 mL solution containing 3.0 mM $NaBH_4$ (aq) and 1.0 mM Asp was prepared and the AgNP synthesis was initiated with the addition of 15 mL of 0.5 mM $AgNO_3$ (aq) solution to the previous mixture under continuous stirring on a magnetic stir plate. The synthesis of AgNP@GlcN and AgNP@Suc were performed utilizing the 1.5 mM of GlcN and 1.5 mM of Suc, respectively. Particularly, the pH of the aqueous solution containing $NaBH_4$ and Asp was adjusted to 8.3, by adding 0.1 M HCl (aq) as needed prior to the addition of $AgNO_3$ (aq). The reaction mixtures were stirred for 2 h, leading to a bright yellow colour solution of AgNP. The AgNP were left in the dark for approximately 24 h for further stabilization.

Synthesis of silver nanoplates

Silver seeds were prepared as follows: 0.2 mM of Irgacure 2959 (I-2959), 0.2 mM of $AgNO_3$ and 1.0 mM of Trisodim citrate were mixed together and irradiated for 5 minutes under UVA illumination. Then the seeds were allowed to grow to nanoplates by illumination for 24 hours using 590 nm LED. [31]

Synthesis of gold nanorods

The synthesis of gold nanorods AuNR was based on a seed-mediated method reported by He *et al.* Briefly, the seed solution was made by the addition of 25 mL of $HAuCl_4$ (0.1 M) to 10 mL of $C_{16}TAB$ (0.1 M). Then, 0.6 mL of an ice-cold $NaBH_4$ aqueous solution (0.01

M) was added. The mixture was stirred vigorously for 2 minutes and aged at room temperature for 45 minutes. Next, a growth solution was made by dissolving 3.6 g of C_{16}TAB and 0.44 g of 5-bromosalicylic acids in 100 mL of warm MilliQ water (55 ^{o}C). Then, 1.92 mL of aqueous $AgNO_3$ was added and the solution was left undisturbed for 15 minutes at room temperature to further add 100 mL of a $HAuCl_4$: $3H_2O$. Upon gentle mixing of the solution for 15 minutes, 0.5 mL of 0.1 M ascorbic acid was added with vigorous stirring for 30 seconds until the mixture became colorless. Finally, 0.32 mL seed solution was added and the mixture was stirred for 30 seconds to then incubate it at 27 ^{o}C for 12 hours. The final AuNR solution was centrifuged at 11,000 rpm for 10 minutes and re-dispersed in water.

Instrumentation

Scanning Electron Microscopy (SEM) images were recorded using a JSM-7500F field emission scanning electron microscope from JEOL Ltd.

UV-visible Spectroscopy (UV-VIS) Absorption spectra were recorded by a CARY 100 UV-vis spectrometer.

Transmission Electron Microscopy (TEM) TEM analyses were carried out on a JEM-2010F microscope (JEOL, 200 kV, 0.14 nm resolution). For this purpose, samples were prepared by dipping the carbon-coated copper grid in the sonicated suspension of the material. The digital analysis of the TEM images were done using image J.

Zeta potential were measured with a Malvern Zetasizer (model Nano-S)

2.2.2. Results and discussion

Before assessing the antibacterial activity of the AgNS, It was important to understand the properties of the AgNS being tested. Therefore; they were characterized by multiple methods such as UV-VIS, SEM, TEM and zeta potential.

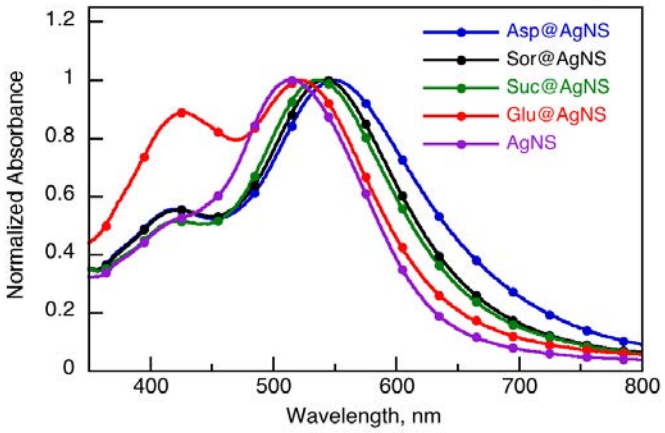

Figure 2.1. Absorption spectra of sweetener-coated AgNS solutions.

Two bands can be distinguished in the absorption spectra in figure 2.1, this is in agreement with the presence of metallic anisotropic nanostructures where the plasmon resonance is split into transversal plasmon at 410 nm and longitudinal plasmon at 540- 560 nm depending on the sweetener that is used for coating and the particle aspect ratio.[32, 33] It was noticed that the longitudinal plasmon has higher sensitivity than the transversal one with regard to aspect ratio and the refractive index of the environment. The variation of the maximum wavelength of the longitudinal plasmon band between 540-560 nm is due to the different particle aspect ratio. [23,34] Moreover, the presence of different sweeteners led to changes in the refractive index of the particle surrounding environment which in turn led to changes in the maximum wavelength of longitudinal plasmon.

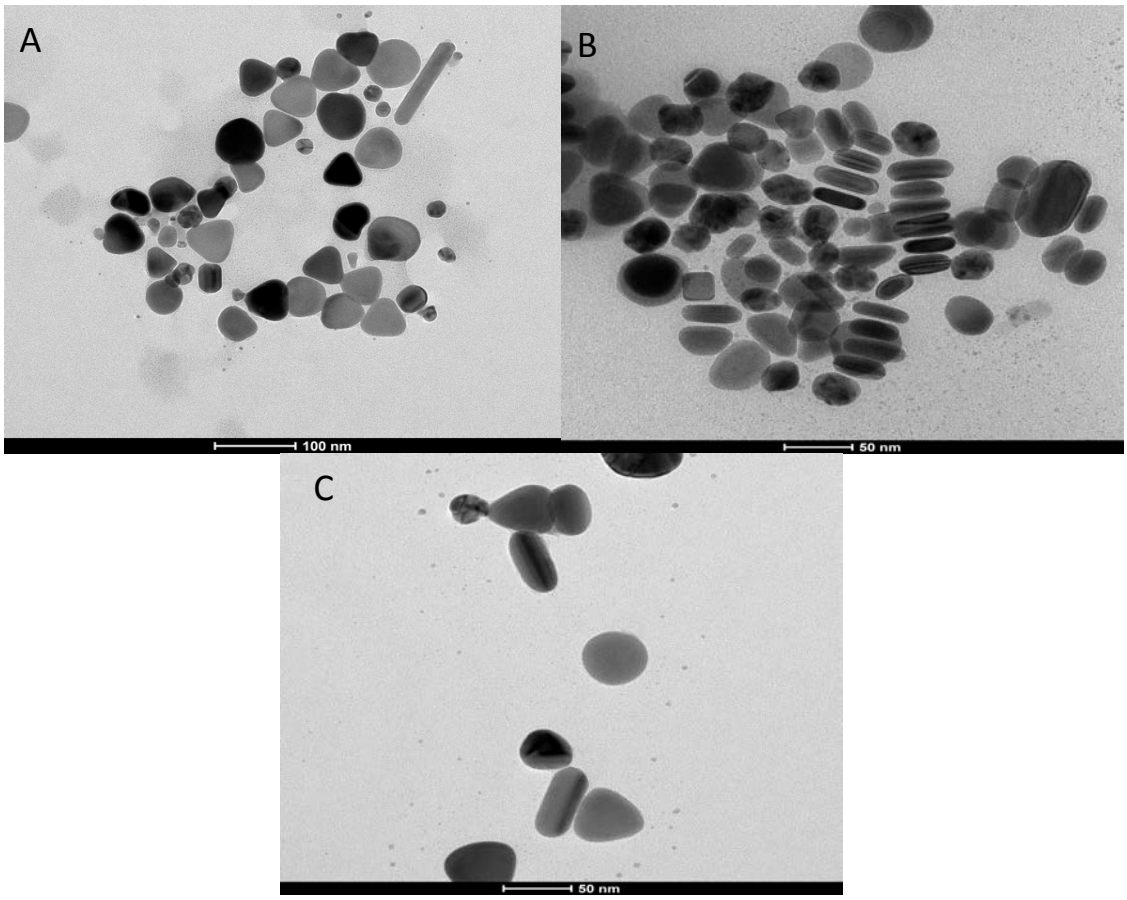

Figure 2.2.TEM image of a polydisperse and polymorphic A)Suc@AgNS solution, B) GlcN @AgNS, and C) Sor@AgNS

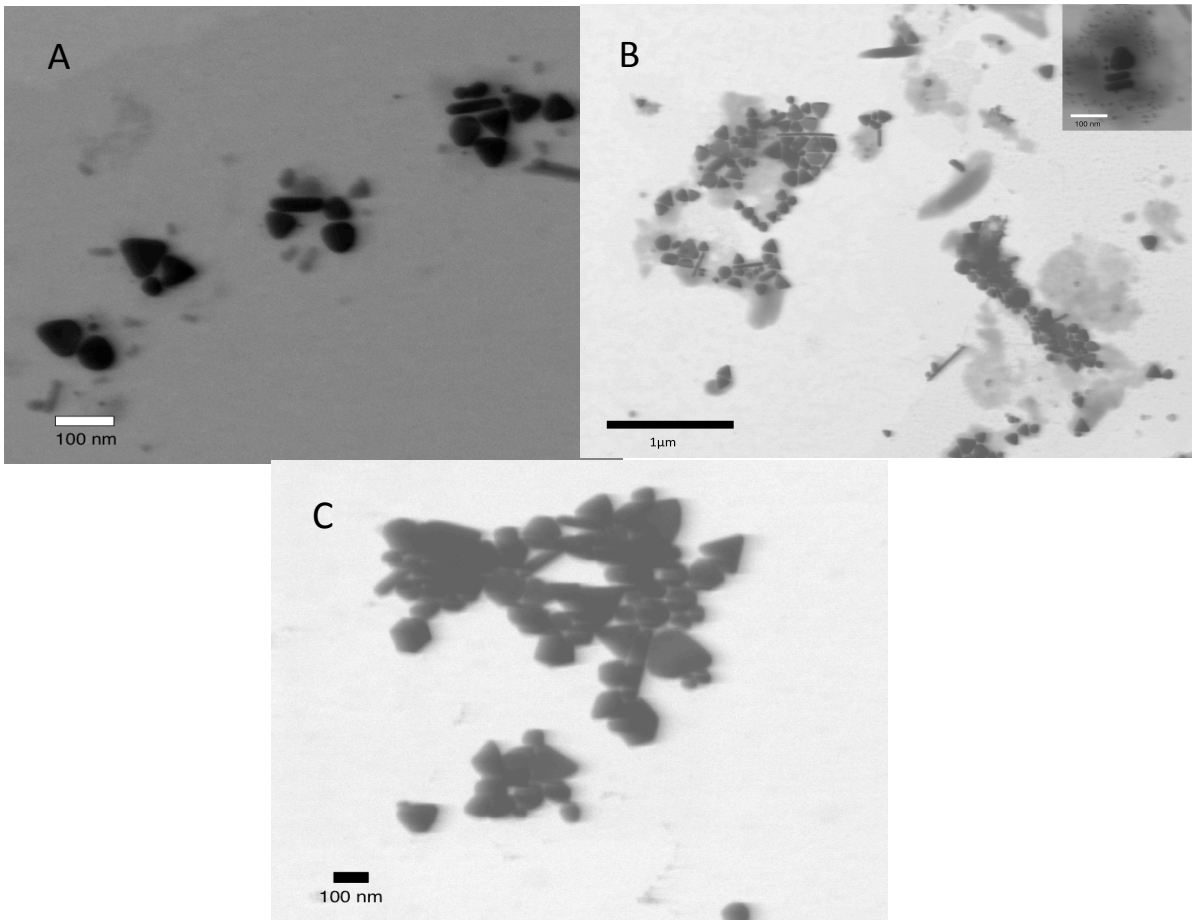

Figure 2.3**.** SEM image of a polydisperse and polymorphic A) Asp@AgNS solution, B) naked AgNS, and C) Sor@AgNS

The coated AgNS were characterized by TEM and SEM. The images obtained from SEM and TEM (Figures 2.2-2.3) show how sweetener-coated AgNS solutions are composed of spherical particles, nanoplates, and silver nanorods of varying size and aspect ratio – possessed highly polydisperse and polymorphic characteristics –. Extensive particle counting showed a higher percentage of spherical nanoparticles (~70%) with average particle size ~ 20nm compared to anisotropic nanorods (~20%) average particle size ~49 nm and nanoplates (~10%) average particle size ~31 nm in each one of the sweetener-coated nanostructure solutions. The analysis of 60 TEM and SEM images allowed us to estimate the distribution of the different shapes, as illustrated in Figure 2.4

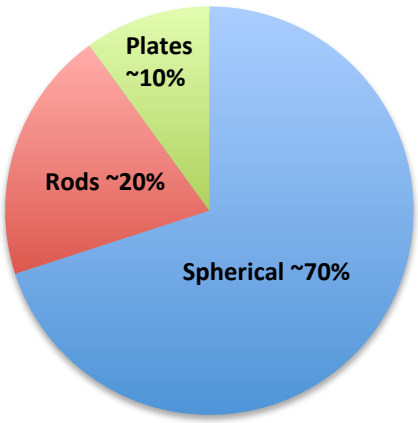

Figure 2.4. Distribution of different morphologies for AgNS stabilized with sucralose.

In addition all other nanomaterials that were synthesized were characterized by UV-VIS and TEM. Characterization of these materials is presented in figures 2.5-2.9

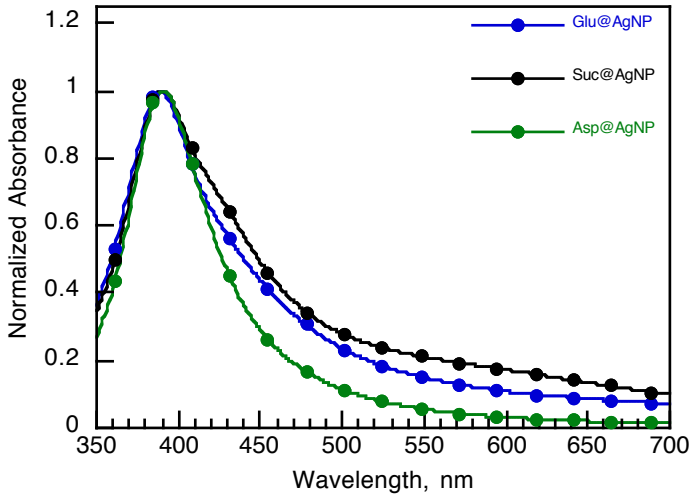

Figure 2.5. Absorption spectra of sweetener-coated silver nanoparticle solutions.

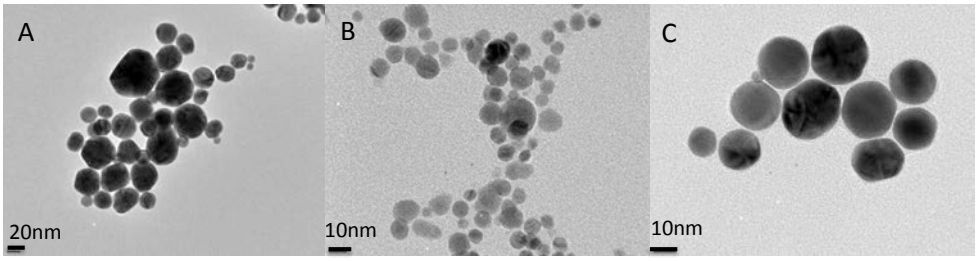

Figure 2.6**.** TEM image of **A** GlcN @AgNP, **B** Suc@AgNP, **C** Asp@AgNP.

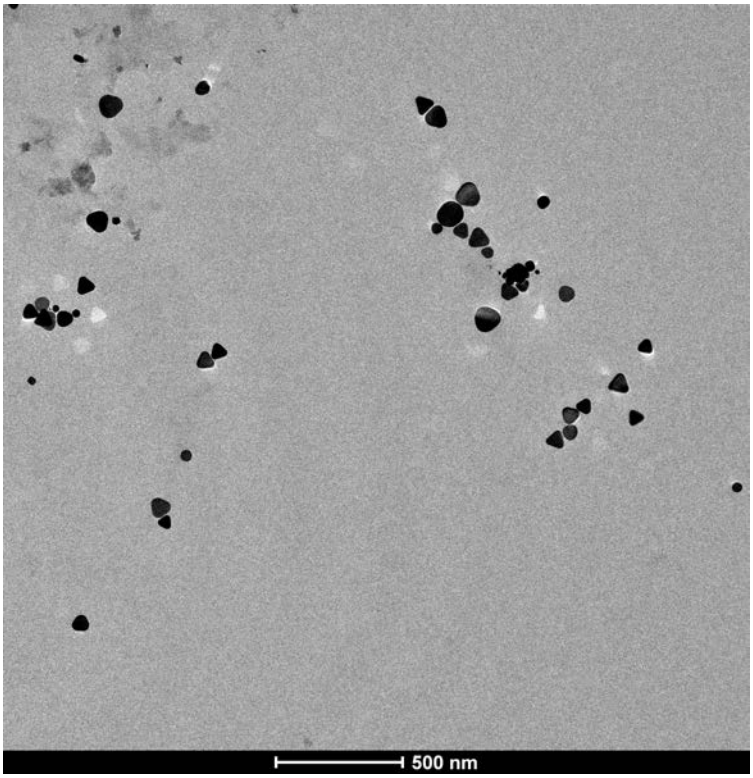

Figure 2.7**.** TEM image of citrate stablized silver nanoplates.

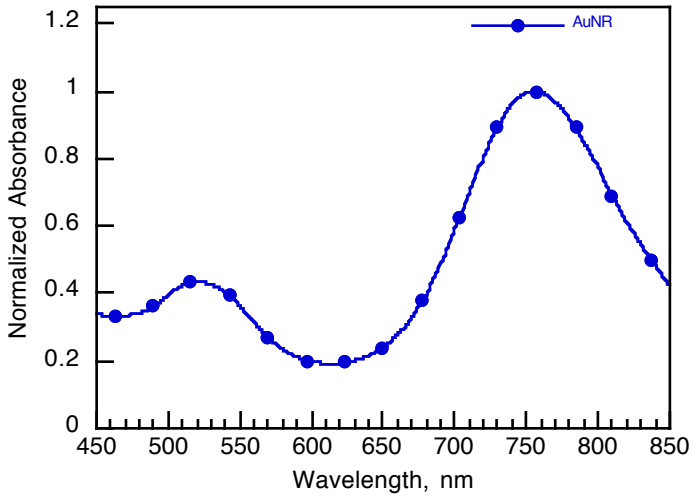

Figure 2.8. Absorption spectra of AuNR in water.

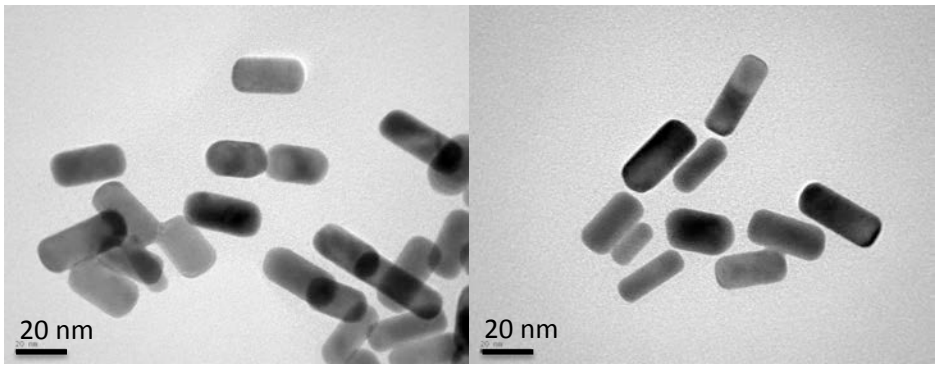

Figure 2.9. TEM image of AuNR in water.

Stability assay

The relative stability of each AgNS solution was also evaluated by measuring their corresponding zeta (ζ) potential. ζ Potential is related to the particle's dispersion, aggregation and flocculation in which aggregation is induced by the presence of a polymer. Colloids are usually stabilized via electrostatic repulsion – in the form of double electric layer – or by steric interaction – where the organic species attached to the surface of nanoparticles provides a layer that prevents aggregation. Electrostatic repulsion is the most prevalent way to stabilize the nanoparticles in aqueous solution and is done by adding surface bound ionisable species. Figure 2.10 shows the ion distribution around the nanoparticles. For negatively charged particles, the net charge at the surface of the particle affects the organization of the ions in the region that surrounds the particle, which leads to increased concentration of the counter ion close to the surface of the particle, creating a double layer. The environment around the particles consists of two layers, the Stern layer where the ions are firmly attached to the surface of the particles and the diffuse layer where ions are more weakly bound. The plane formed between these two layers is known as slipping plane and in this boundary the ζ potential is measured. When the absolute value of ζ potential is bigger than 30 mV the colloid is considered electrostatically stable. [35, 36]

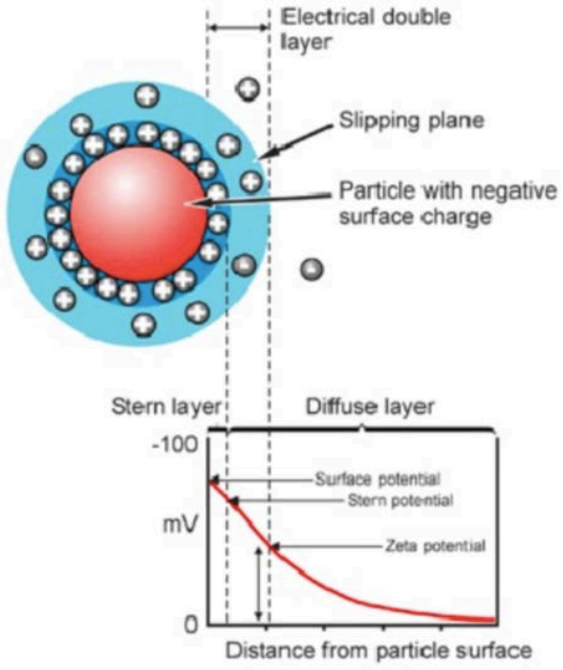

Figure 2.10. Schematic illustration of the double electric layer and the position at which the ζ potential is measured. Reprinted with permission from ref [37]

The ζ potentials of the coated silver nanostructures are summarized in table 2.1. The ζ potential values obtained indicate that these nanostructures form stable suspensions in water and possess a positively charged surface, which is consistent with the presence of positively charged quaternary amino groups on the surface of the nanostructures belonging to C_{16TAB} stabilizing molecules and important for their interaction with bacteria. The relatively large standard deviations (SD) obtained are likely due to the polydisperse and polymorphic nature of the samples. Nevertheless, the ζ potential values fall within the characteristic range of electrostatic stable colloidal nanoparticle suspensions (≥30mV).

Sample	ζ - Potential (mV)
Asp@AgNS	47 ± 14
Sor@AgNS	56 ± 16
Suc@AgNS	60 ± 14
GlcN@AgNS	58 ± 16
AgNS	51 ± 16

Table 2.1. ζ-potential values of polydisperse and polymorphic sweetener-coated AgNS

The optical properties of these coated AgNS were examined by taking the absorption spectra of the AgNS over time. The results were demonstrated in terms of the position of the longitudinal plasmon band (LSPR) with respect to its transverse counterpart (TSPR) as well as the absorbance ratio between them (LSPR/TSPR) with increasing storage times. A decrease in distance between longitudinal and transverse plasmon bands was observed for all sweetener-coated AgNS solutions due to a shift of the former to shorter wavelengths while the position of the latter remained constant at approximately 420 nm; Figure 2.15 shows these findings.

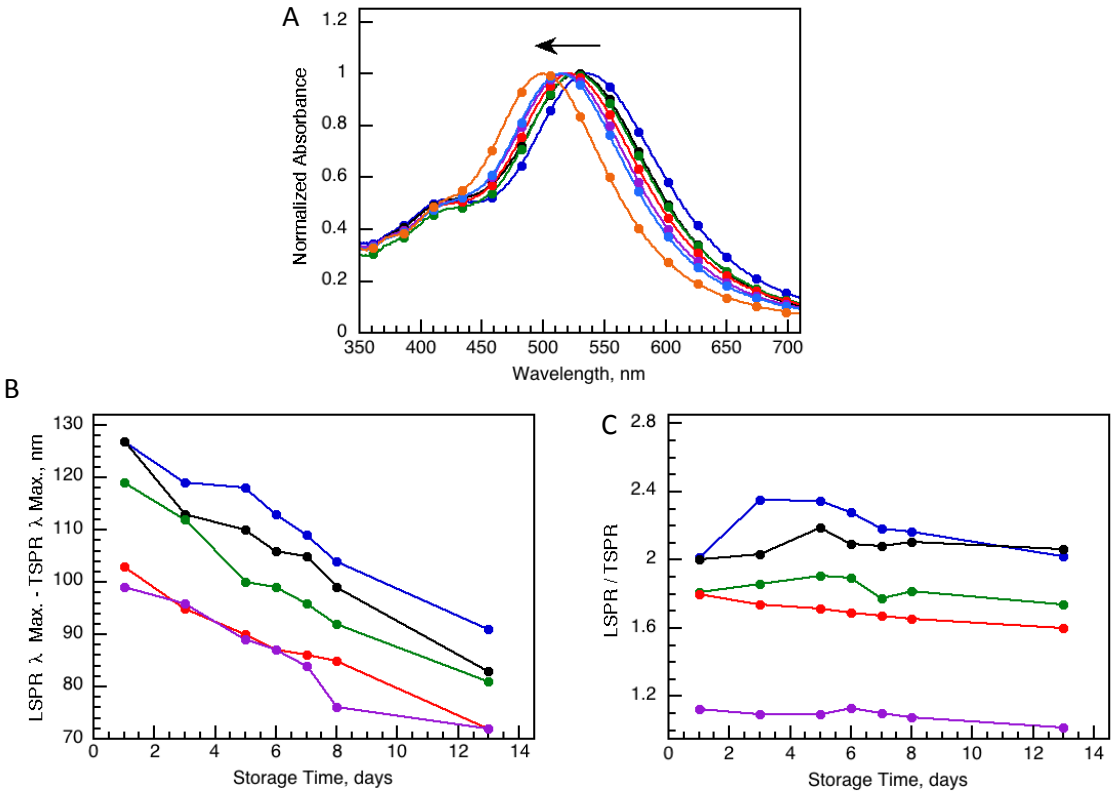

Figure 2.11 A) Absorption spectra of Suc@AgNS solutions for days 1, 3, 5, 6, 7, 8 and 13; B) LSPR band with respect to TSPR band and C) LSPR/TSPR ratio at different storage times. Blue naked AgNS, black Suc AgNS, green Sor AgNS, red Asp AgNS, purple GlcN AgNS

Figure 2.11 B shows variation in position of the LSPR with respect to the TSPR at consecutive storage times for each sweetener-coated AgNS solution. Similar slopes where obtained for these curves exhibiting the same trend in terms of changes in optical properties with time. Furthermore, the ratio between the plasmon bands (LSPR/TSPR), shown in Figure 2.11 C, stayed the same over time suggesting that the changes in optical properties mentioned above could be due to changes in refractive index of the immediate environment surrounding the AgNS rather than to changes in its shape or size. Moreover, these results are consistent with the high stability of the AgNS evidenced by the ζ potential measurements that are greater than +30 mV presented above.

2.3. Antibacterial Activity of Silver nanostructure

The sweetener coated AgNS were tested against gram-positive bacteria such as *Staphylococcus aureus,* and methicillin-resistant *Staphylococcus aureus* (MRSA), as well as on gram-negative bacteria such as *Escherichia coli* and *Pseudomonas aeruginosa.*

2.3.1. Experimental procedures

Bacterial strains and growth conditions

The bacterial strains used were *Staphylococcus aureus* ATCC 25923m, *Pseudomonas aeruginosa* ATTC 27853U, MRSA ATTC 29247m and *Escherichia coli* ATCC 25922U. Bacteria were cultured for 20-24 hours on an agar plate.

Planktonic Assay for MIC Determination

McFarland standard 0.5 bacterial suspensions were prepared by dissolving bacteria cultures in 0.9% saline solution. The bacterial suspensions were diluted to a factor of 100 using Mueller Hinton broth (MHB II; Becton Dickinson, Oakville, Ontario, Canada). The planktonic assay was then prepared in a 96 well round bottom microtiter plate (Nunc Inc., Rosklide, Denmark). Serial dilution was carried out to obtain a final range of 0.38μM-0.33mM silver content. Wells 11 and 12 were used as control wells where well 11 had bacteria with only sweetener and no AgNS. While well 12 was a sterility well, respectively. The prepared microtiter plate was gently shaken for 30 seconds and incubated for 18 hours at 37°C under ambient air. The bacteriostatic MIC end point was taken as the lowest concentration of AgNS with no visible bacterial growth. Each measurement was done in triplicate to ensure accuracy. Finally, the lack of bacterial growth and consequently the MIC, was confirmed by diluting 10 μL of such solution in 100 μL of PBS to further plate it on agar and incubate for 18 h at 37°C for colony counting.

Biofilm Assay for $MBEC_{80}$ Determination

The viability of microbial cells inhabiting the biofilm population was determined following a modified MTT colorimetric method based on the reduction of a tetrazolium salt previously reported by Kairo *et al.*[38] Briefly, biofilms were prepared in a 96 well round bottom microtiter plate (Nunc Inc., Roskilde, Denmark) by adding 50 μ L of bacterial suspension and 50 μ L of MH broth. A Nunc Microplate Peg Lid was placed on the plate and incubated on a rocker table for 16 hrs at 37°C in ambient air. Upon bacterial incubation, the Peg lid was treated with 10% N-acetyl-L-cysteine in order to disrupt the biofilm. Then, the bacterial suspension was removed and 200 μL of PBS and 50 μL of a 0.3 % MTT solution were added

and incubated for 2 h at 37°C. Then, the MTT solution was removed from the wells and 150 μL of DMSO and 25 μL of 0.1 M glycine buffer (pH 10.2) were immediately added to the wells in order to dissolve the formazan crystals formed. Finally, incubation was carried out for 15 min at room temperature and the absorbance of the solution was measured at a wavelength of 550 nm using a Microplate Reader Model 550 (BioRad). Experiments were done in triplicate to eliminate environmental errors and ensure accuracy.

Hemolysis Assay

The integrity of red blood cells from healthy human volunteers (from Córdoba, Argentina) incubated with sweetener-coated AgNS 1.5 mg/mL was evaluated following a modified version of a procedure previously reported by Choi J. *et al.*[21] Upon incubation, AgNS were removed by centrifugation –in order to avoid any possible spectral interference– followed by absorbance measurements at 541 nm, corresponding to free hemoglobin. Measurements were performed after 24 h of incubation. A solution of 0.9% NaCl and H_2O were used as negative and positive control of hemolysis, respectively.

2.3.2. Results and discussion

The sweetener coated AgNS were tested on *Staphylococcus aureus*, *Escherichia coli*, methicillin-resistant *Staphylococcus aureus* (MRSA) and *Pseudomonas aeruginosa*. The average minimum inhibition concentrations (MICs) and minimal biofilm eradication concentration ($MBEC_{80}$) based on silver content for the planktonic and biofilm assays are summarized in table 2.2.

Table 2.2. Average planktonic MICs and biofilm $MBEC_{80}$ (μg/mL) of sweetener-coated AgNS

Entry	Sample	*S. aureus*		*E. coli*	
		Planktonic MIC	Biofilm $MBEC_{80}$	Planktonic MIC	Biofilm $MBEC_{80}$
1.	AgNS	0.148	0.841	0.443	13.5
2.	Asp@AgNS	0.049	0.420	0.443	6.74
3.	Suc@AgNS	0.177	0.841	0.443	13.5
4.	Sor@AgNS	0.049	0.841	0.443	6.74
5.	GlcN @AgNS	0.006	0.210	1.33	13.5
Entry	Sample	MRSA		*P. aeruginosa*	
		Planktonic MIC	Biofilm $MBEC_{80}$	Planktonic MIC	Biofilm $MBEC_{80}$
6.	AgNS	0.443	1.68	11.9	N/I*
7.	Asp@AgNS	0.148	0.841	11.9	53.9
8.	Suc@AgNS	0.177	6.74	11.9	N/I*
9.	Sor@AgNS	0.049	1.68	11.9	N/I*
10	GlcN@AgNS	0.148	1.68	11.9	N/I*

*N/I = no inhibition

*N/I = no inhibition

The goal of this experiment was fulfilled as the planktonic and biofilm form of the tested bacteria were inhibited using sweetener-coated AgNS at minimum concentrations that ranged between 0.006 μg/mL and 13.5 μg/mL. Prior reports have outlined the need to use higher concentration of monodisperse AgNP solutions that ranged between 30 μg/mL and 200 μg/mL.[39, 40]

It was noticed that higher concentration of naked AgNS (CTAB- stabilized) were required compared to the coated AgNS, which emphasizes the importance of the sweetener in the inhibition of bacterial growth (table 2.2 entries 1-10).

Glucosamine and sorbitol-coated nanostructures were found to be the best sweeteners against *S. aureus*. Glucosamine could be increasing the nanoparticle's uptake as it is a well known nutrient for the bacteria.[25] In the case of *E. coli* and *MRSA* lower concentrations of sorbitol-coated AgNS were bactericidal to both planktonic and biofilm bacterial forms. It was found that *S. aureus* is more sensitive toward AgNS presenting overall lower MICs and $MBEC_{80}$ in comparison with the other bacteria. In contrast, *P. aeruginosa* has the highest resistance toward the bactericidal nanostructure solutions since it is one of the most highly adaptable microorganisms with a very complex and impenetrable membrane.[41]

In order to determine whether silver ions or AgNP are responsible for the inhibition of the bacterial growth, a control experiment was done using 1mM $AgNO_3$ solution. Results are summarized in table 2.3

Table 2.3. Average planktonic MICs and biofilm $MBEC_{80}$ (μg/mL) of 1.0 mM $AgNO_3$ solution

Entry	Sample	*S. aureus*		*E. coli*	
		Planktonic MIC	Biofilm $MBEC_{80}$	Planktonic MIC	Biofilm $MBEC_{80}$
1.	1.0 mM $AgNO_3$	0.443	13.5	1.33	N/I*
Entry	Sample	MRSA		*P. aeruginosa*	
		Planktonic MIC	Biofilm $MBEC_{80}$	Planktonic MIC	Biofilm $MBEC_{80}$
2.	1.0 mM $AgNO_3$	00.443	13.5	N/I*	N/I*

Higher MIC and $MBEC_{80}$ were required when 1.0 mM $AgNO_3$ solution was used (table 2.3 entry 1), this proves that AgNS are responsible for the inhibition of bacteria and not Ag^+ [42] The change in the longitudinal plasmon in the absorption spectra Figure (2.14) is due to the changes in the refractive index of the environment that surrounds the nanostructures, this change is likely due to the partial removal of the nanostructures' coating.[20, 26] In addition to that, AgNP have specific mechanisms that make them able to adhere to the microbial cell such as penetration, metabolic interference and free radical generation that have been found to play an important role.[41]

In order to evaluate the importance of the polydispersity of the nanostructures in the inhibition of the growth of bacteria, monodispersed nanostructures were tested against the bacteria. Table 2.4 summarizes these results

Table 2.4. Average planktonic MICs and biofilm MBEC80 (μg/mL) of monodisperse nanostructures

Entry	Sample	*S. aureus*		*E. coli*	
		Planktonic MIC	Biofilm $MBEC_{80}$	Planktonic MIC	Biofilm $MBEC_{80}$
1.	Asp@AgNP	35.6	N/I*	N/I*	N/I*
2.	Suc@AgNP	35.6	N/I*	53.9	N/I*
3.	Sor@AgNP	35.6	N/I*	107	N/I*
4.	Silver nanoplates	*11.9*	*N/I**	*11.9*	N/I*
5.	AuNR	N/I*	N/I*	N/I*	N/I*
6.	Core-shell Ag@AuNPs	N/I*	N/I*	N/I*	N/I*
Entry	Sample	MRSA		*P. aeruginosa*	
		Planktonic MIC	Biofilm $MBEC_{80}$	Planktonic MIC	Biofilm $MBEC_{80}$
7.	Asp@AgNP	35.6	N/I*	N/I*	N/I*
8.	Suc@AgNP	35.6	N/I*	53.9	N/I*
9.	Sor@AgNP	35.6	N/I*	N/I*	N/I*
10	Silver nanoplates	11.9	N/I*	11.9	N/I*
11	AuNR	N/I*	N/I*	N/I*	N/I*
12	Core-shell Ag@AuNPs	N/I*	N/I*	N/I*	N/I*

*N/I = no inhibition

Higher concentration of silver was required when monodisperse sweetener-coated AgNS solutions were tested (table 2.4 entries 1-3 and 7-9). When silver nanoplates were tested (table 2.4 entry 4 and 10) there was inhibition for the planktonic form only but higher concentration of silver was required. No inhibition was also observed when AuNRs, Core-shell Ag@AuNPs were tested (table 2.4 entries 5,6,11,12). These finding support the role and the importance of the polymorphism in improving the antibacterial efficiency.

A question that needed to be answered is whether the sweetener alone is responsible for the bactericidal properties of these structures or not. Table 2.5 present the results that were obtained when the sweeteners were tested alone. All sweeteners were innocuous to bacteria in the planktonic or biofilm form.

Table 2.5. Average planktonic MICs and biofilm $MBEC_{80}$ (**μ**g/mL) of sweetener in the absence of AgNS

Entry	Sample	*S. aureus*		*E. coli*	
		Planktonic MIC	Biofilm $MBEC_{80}$	Planktonic MIC	Biofilm $MBEC_{80}$
	Aspartam	N/I*	N/I*	N/I*	N/I*
	Sucralose	N/I*	N/I*	N/I*	N/I*
	Sorbitol	N/I*	N/I*	N/I*	N/I*
	Glucosamine	N/I*	N/I*	N/I*	N/I*
Entry	Sample	MRSA		*P. aeruginosa*	
		Planktonic MIC	Biofilm $MBEC_{80}$	Planktonic MIC	Biofilm $MBEC_{80}$
	Aspartam	N/I*	N/I*	N/I*	N/I*
	Sucralose	N/I*	N/I*	N/I*	N/I*
	Sorbitol	N/I*	N/I*	N/I*	N/I*
	Glucosamine	N/I*	N/I*	N/I*	N/I*

*N/I = no inhibition

In general the concentrations of AgNS that were found in this work are lower than those of AgNP previously reported in the literature.[32] these efficient low concentrations could be attributed to the polymorphic nature of the solutions tested, which is thought to impact the adaptability of bacteria related to the multiple morphologies of the AgNS.

Hemolysis Tests

Hemolysis is breakage of red blood cell and the liberation of their contents (cytoplasm). When this test is administered in mammals, nanomaterials will meet the blood cells. Therefore the study of the effect of nanostructures on blood cell is important. Red blood cells are the most sensitive as they don't have a nucleus. The damage of the membrane is an indicator of stress and can be measured by monitoring hemoglobin released upon such damage.

Free hemoglobin released into the serum after incubation of red blood cells with coated AgNS solutions and their MICs was monitored. Figure 2.12 illustrates that more than 63% of the erythrocytes maintained their integrity under these conditions. However, the amount of hemolysis observed might be due to the osmotic effect of water in which the nanoparticles are suspended.

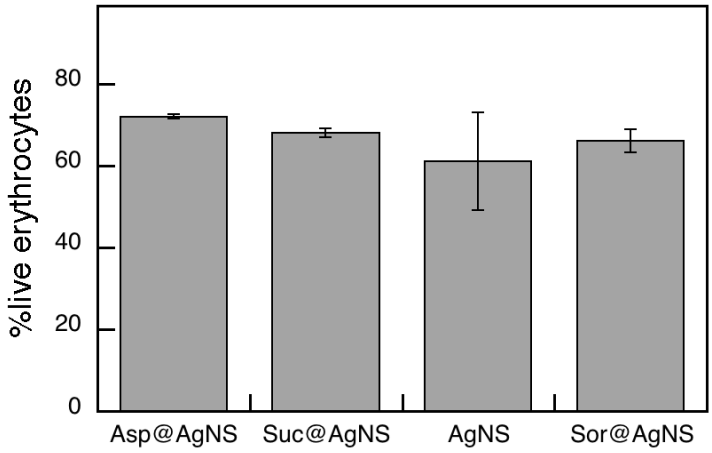

Figure 2.12. Values for erythrocytes preserving their integrity when exposed to polydisperse and polymorphic coated AgNS solutions.

2.4. Conclusion

The synthesis, characterization and bactericidal properties of sweetener coated AgNS were achieved. The seed mediated method at room temperature was the method of choice for the synthesis of the nanostructures.

SEM, TEM and UV-VIS spectroscopy were the method of choice for characterizing the AgNS. Zeta potential measurements were performed to evaluate the stability of these coated AgNS. The coated AgNS displayed great bactericidal properties against *Staphylococcus aureus, Escherichia coli, methicillin-resistant Staphylococcus aureus (MRSA) and Pseudomonas aeruginosa*. Polydispersed coated AgNS were proven to be more efficient than their monodispersed counterparts. This finding emphasizes the importance of the polymorphism character of these AgNS. The study how each shape and size of nanoparticle effect bacteria differently is well known [43]but the essence of polymorphism and polydispersity has not been established before. Glucosamine- and sorbitol-coated AgNS solutions have the best bactericidal effect for both *S. aureus* in planktonic and biofilm forms, while Sor@AgNS proved to be the most efficient against *E. coli* and *MRSA*.

2.6. Future work

Future work will involve the use of these coated AgNS on bacteria from human samples. The plasmonic properties of AgNS can allow us to use visible light to enhance the bactericidal properties these nanostructures. Moreover, The cytotoxicity of the coated AgNS needs to be assessed to determine whether these AgNS are safe for human consumption. The hemolysis effect can be minimized by changing the media that is used for the suspension of the nanostructures, as well as the use of binary coating that maximize biocompatibility.

Appendix

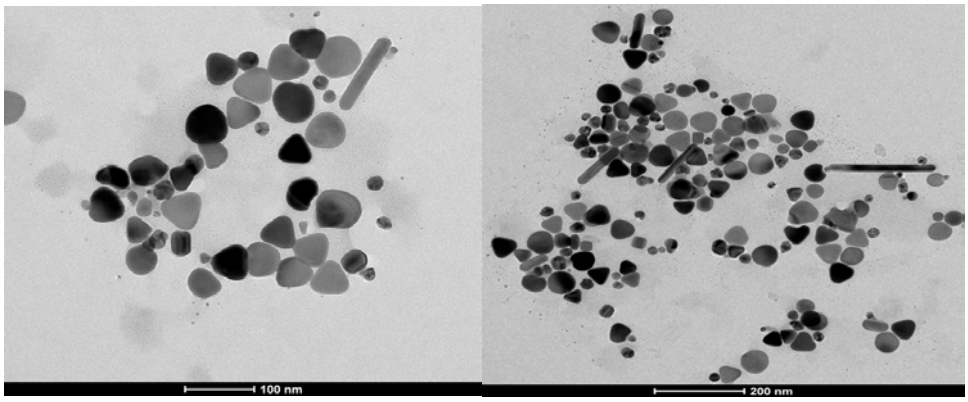

Figure 2.2.TEM images of a polydisperse and polymorphic Suc@AgNS solution.

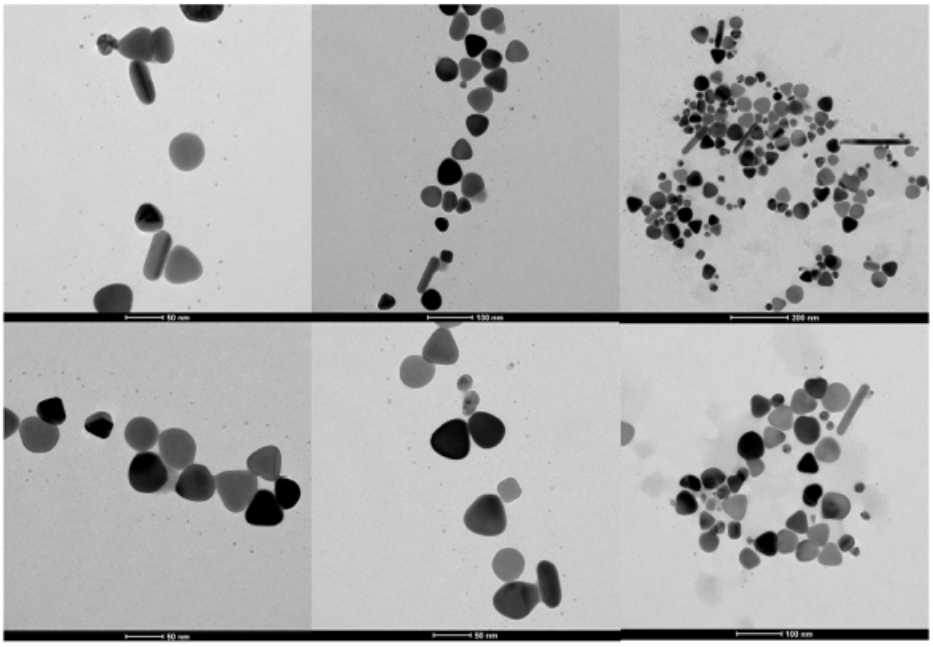

Figure 2.3.TEM images of a polydisperse and polymorphic Sor@AgNS solution.

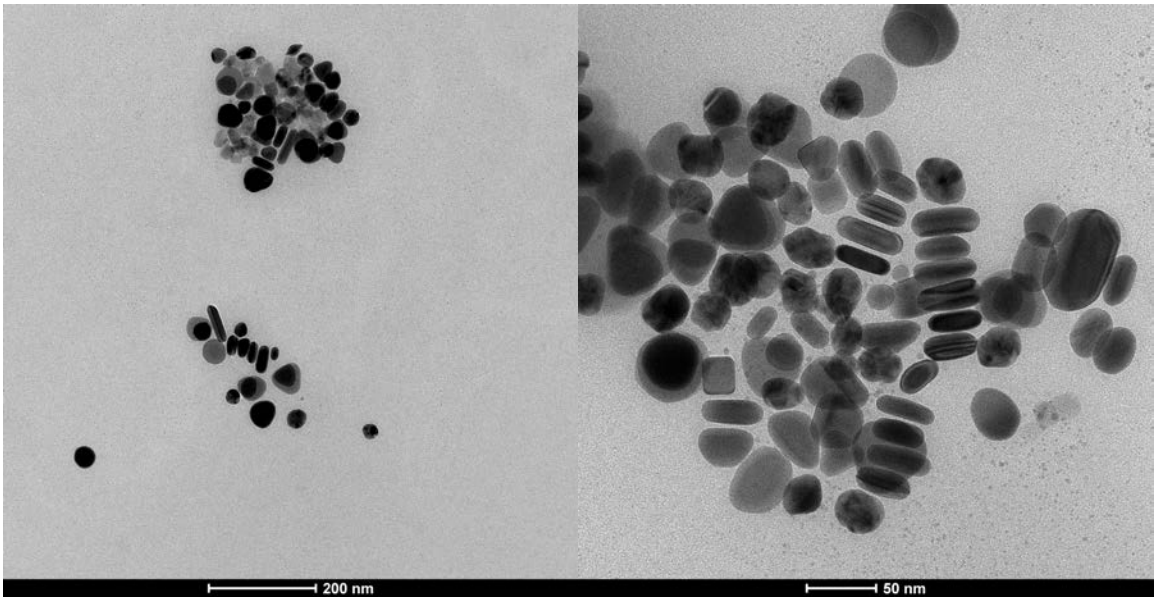

Figure 2.4.TEM images of a polydisperse and polymorphic GlcN @AgNS solution

References

1. Ventola, C. L., The Antibiotic Resistance Crisis: Part 1: Causes and Threats. *Pharm Ther* **2015,** *40* (4), 277-283.

2. Adeniji, F., Global analysis of strategies to tackle antimicrobial resistance. *Int J Pharm Pract* **2018,** *26* (1), 85-89.

3. Mrinal, B., Development of Resistance to Antibiotics. In *Chemistry of Antibiotics and Related Drugs*, 1 ed.; Springer International Publishing 2016; pp 27-48.

4. Pitiriga, V.; Vrioni, G.; Saroglou, G.; Tsakris, A., The Impact of Antibiotic Stewardship Programs in Combating Quinolone Resistance: A Systematic Review and Recommendations for More Efficient Interventions. *Adv Ther* **2017,** *34* (4), 854-865.

5. Theuretzbacher, U.; Årdal, C.; Harbarth, S., Linking Sustainable Use Policies to Novel Economic Incentives to Stimulate Antibiotic Research and Development. *Infect Dis Rep* **2017,** *9* (1), 6836.

6. Nagel, J. L.; Kaye, K. S.; LaPlante, K. L.; Pogue, J. M., Antimicrobial Stewardship for the Infection Control Practitioner. *Infect Dis Clin North Am* **2016,** *30* (3), 771-84.

7. Kuroda, T.; Ogawa, W., Search for Novel Antibacterial Compounds and Targets. *Yakugaku Zasshi* **2017,** *137* (4), 383-388.

8. Sharma, S.; Hameed, S.; Fatima, Z., Natural Compounds for Overcoming Multidrug Resistance in Mycobacteria. *Recent Pat Biotechnol* **2016,** *10* (2), 167-174.

9. Fields, F. R.; Lee, S. W.; McConnell, M. J., Using bacterial genomes and essential genes for the development of new antibiotics. *Biochem Pharmacol* **2017,** *134*, 74-86.

10. Ge, L.; Li, Q.; Wang, M.; Ouyang, J.; Li, X.; Xing, M. M., Nanosilver particles in medical applications: synthesis, performance, and toxicity. *Int J Nanomedicine* **2014,** *9*, 2399-407.

11. Salata, O., Applications of nanoparticles in biology and medicine. *J Nanobiotechnology* **2004,** *2* (1), 3.

12. Grunkemeier, G. L.; Jin, R.; Im, K.; Holubkov, R.; Kennard, E. D.; Schaff, H. V., Time-related risk of the St. Jude Silzone heart valve. *Eur J Cardiothorac Surg* **2006,** *30* (1), 20-7.

13. Saez, S.; Fasciani, C.; Stamplecoskie, K. G.; Gagnon, L. B.; Mah, T. F.; Marin, M. L.; Alarcon, E. I.; Scaiano, J. C., Photochemical synthesis of biocompatible and antibacterial silver nanoparticles embedded within polyurethane polymers. *Photochem Photobiol Sci* **2015,** *14* (4), 661-4.

14. Alarcon, E. I.; Udekwu, K.; Skog, M.; Pacioni, N. L.; Stamplecoskie, K. G.; González-Béjar, M.; Polisetti, N.; Wickham, A.; Richter-Dahlfors, A.; Griffith, M.; Scaiano, J. C., The biocompatibility and antibacterial properties of collagen-stabilized, photochemically prepared silver nanoparticles. *Biomaterials* **2012,** *33* (19), 4947-56.

15. Elechiguerra, J. L.; Burt, J. L.; Morones, J. R.; Camacho-Bragado, A.; Gao, X.; Lara, H. H.; Yacaman, M. J., Interaction of silver nanoparticles with HIV-1. *J Nanobiotechnology* **2005,** *3*, 6.

16. Dibrov, P.; Dzioba, J.; Gosink, K. K.; Häse, C. C., Chemiosmotic mechanism of antimicrobial activity of Ag(+) in Vibrio cholerae. *Antimicrob Agents Chemother* **2002,** *46* (8), 2668-70.

17. Holt, K. B.; Bard, A. J., Interaction of silver(I) ions with the respiratory chain of Escherichia coli: an electrochemical and scanning electrochemical microscopy study of the antimicrobial mechanism of micromolar Ag+. *Biochemistry* **2005,** *44* (39), 13214-23.

18. Fasciani, C.; Silvero, M. J.; Anghel, M. A.; Argüello, G. A.; Becerra, M. C.; Scaiano, J. C., Aspartame-stabilized gold-silver bimetallic biocompatible nanostructures with plasmonic photothermal properties, antibacterial activity, and long-term stability. *J Am Chem Soc* **2014,** *136* (50), 17394-7.

19. Stamplecoskie, K. G.; Scaiano, J. C., Light emitting diode irradiation can control the morphology and optical properties of silver nanoparticles. *J Am Chem Soc* **2010,** *132* (6), 1825-7.

20. Ivask, A.; Elbadawy, A.; Kaweeteerawat, C.; Boren, D.; Fischer, H.; Ji, Z.; Chang, C. H.; Liu, R.; Tolaymat, T.; Telesca, D.; Zink, J. I.; Cohen, Y.; Holden, P. A.; Godwin, H. A., Toxicity mechanisms in Escherichia coli vary for silver nanoparticles and differ from ionic silver. *ACS Nano* **2014,** *8* (1), 374-86.

21. Suresh, A. K.; Pelletier, D. A.; Wang, W.; Morrell-Falvey, J. L.; Gu, B.; Doktycz, M. J., Cytotoxicity induced by engineered silver nanocrystallites is dependent on surface coatings and cell types. *Langmuir* **2012,** *28* (5), 2727-35.

22. Andrews, J. M., Determination of minimum inhibitory concentrations. *J Antimicrob Chemother* **2001,** *48 Suppl 1*, 5-16.

23. Choi, J.; Reipa, V.; Hitchins, V. M.; Goering, P. L.; Malinauskas, R. A., Physicochemical characterization and in vitro hemolysis evaluation of silver nanoparticles. *Toxicol Sci* **2011,** *123* (1), 133-43.

24. Weerasekera, H. A.; Silvero, M. J.; Regis Correa da Silva, D.; Scaiano, J. C., A database on the stability of silver and gold nanostructures for applications in biology and biomolecular sciences. *Biomater Sci* **2016,** *5* (1), 89-97.

25. Hormozi-Nezhad, M. R.; Robatjazi, H.; Jalali-Heravi, M., Thorough tuning of the aspect ratio of gold nanorods using response surface methodology. *Anal Chim Acta* **2013,** *779*, 14-21.

26. Zheng, Z.; Tachikawa, T.; Majima, T., Single-particle study of Pt-modified Au nanorods for plasmon-enhanced hydrogen generation in visible to near-infrared region. *J Am Chem Soc* **2014,** *136* (19), 6870-3.

27. Abdel Rahim, K. A.; Ali Mohamed, A. M., Bactericidal and Antibiotic Synergistic Effect of Nanosilver Against Methicillin-Resistant Staphylococcus aureus. *Jundishapur J Microbiol* **2015,** *8* (11), e25867.

28. Polte, J.; Tuaev, X.; Wuithschick, M.; Fischer, A.; Thuenemann, A. F.; Rademann, K.; Kraehnert, R.; Emmerling, F., Formation mechanism of colloidal silver nanoparticles: analogies and differences to the growth of gold nanoparticles. *ACS Nano* **2012,** *6* (7), 5791-802.

29. Impellizzeri, S.; Simoncelli, S.; Hodgson, G. K.; Lanterna, A. E.; McTiernan, C. D.; Raymo, F. M.; Aramendia, P. F.; Scaiano, J. C., Two-Photon Excitation of a Plasmonic Nanoswitch Monitored by Single-Molecule Fluorescence Microscopy. *Chemistry* **2016,** *22* (21), 7281-7.

30. Murphy, C. J.; Sau, T. K.; Gole, A. M.; Orendorff, C. J.; Gao, J.; Gou, L.; Hunyadi, S. E.; Li, T., Anisotropic metal nanoparticles: Synthesis, assembly, and optical applications. *J Phys Chem B* **2005,** *109* (29), 13857-70.

31. Haes, A. J.; Van Duyne, R. P., A nanoscale optical biosensor: sensitivity and selectivity of an approach based on the localized surface plasmon resonance spectroscopy of triangular silver nanoparticles. *J Am Chem Soc* **2002,** *124* (35), 10596-604.

32. Jain, P. K.; Eustis, S.; El-Sayed, M. A., Plasmon coupling in nanorod assemblies: optical absorption, discrete dipole approximation simulation, and exciton-coupling model. *J Phys Chem B* **2006,** *110* (37), 18243-53.

33. Beck-Broichsitter, M.; Ruppert, C.; Schmehl, T.; Guenther, A.; Betz, T.; Bakowsky, U.; Seeger, W.; Kissel, T.; Gessler, T., Biophysical investigation of pulmonary surfactant surface properties upon contact with polymeric nanoparticles in vitro. *Nanomedicine* **2011,** *7* (3), 341-50.

34. Doane, T. L.; Chuang, C. H.; Hill, R. J.; Burda, C., Nanoparticle ζ -potentials. *Acc Chem Res* **2012,** *45* (3), 317-26.

35. Characterization techniques. https://nanocomposix.com/pages/characterization-techniques - zeta-potential (accessed September 2018).

36. Kairo, S. K.; Bedwell, J.; Tyler, P. C.; Carter, A.; Corbel, M. J., Development of a tetrazolium salt assay for rapid determination of viability of BCG vaccines. *Vaccine* **1999,** *17* (19), 2423-8.

37. Agnihotri, S.; Mukherji, S.; Mukherji, S., Size-controlled silver nanoparticles synthesized over the range 5–100 nm using the same protocol and their antibacterial efficacy. *RSC Adv* **2014,** *4* (8), 3974-3983.

38. Lara, H. H.; Ayala-Núñez, N. V.; Ixtepan Turrent, L. d. C.; Rodríguez Padilla, C., Bactericidal effect of silver nanoparticles against multidrug-resistant bacteria. *World J Microbiol Biotechnol* **2010,** *26* (4), 615-621.

39. Dakal, T. C.; Kumar, A.; Majumdar, R. S.; Yadav, V., Mechanistic Basis of Antimicrobial Actions of Silver Nanoparticles. *Frontiers Microbiol.* **2016,** *7*, 1831.

40. Alarcon, E. I.; Udekwu, K.; Skog, M.; Pacioni, N. L.; Stamplecoskie, K. G.; Gonzalez-Bejar, M.; Polisetti, N.; Wickham, A.; Richter-Dahlfors, A.; Griffith, M.; Scaiano, J. C., The biocompatibility and antibacterial properties of collagen-stabilized, photochemically prepared silver nanoparticles. *Biomaterials* **2012,** *33* (19), 4947-4956.

41. Sadeghi, B.; Garmaroudi, F. S.; Hashemi, M.; Nezhad, H. R.; Nasrollahi, A.; Ardalan, S.; Ardalan, S., Comparison of the anti-bacterial activity on the nanosilver shapes: Nanoparticles, nanorods and nanoplates. *Adv Powder Techn* **2012,** *23* (1), 22-26.

Chapter 3
Expanding the Color Space in the Two-Color Heterogeneous Photocatalysis of Ullmann C-C Coupling Reactions

3.1 Background

The carbon-carbon bond is one of the most important building blocks for pharmaceutical and biological compounds.[1] Due to the essence of this type of bond there has been lot of effort to perform C-C coupling reactions under milder conditions. The use of transition metals to catalyze C-C coupling reactions is considered a very important step that revolutionized the field of organic synthesis. [2, 3] One of the most widely studied transition metals utilized to catalyze this type of reactions is palladium (Pd(0)). There are plenty of examples in literature involving Heck, Sonogashira, Miyaura, and Suzuki couplings.[4] Before Pd^0 became a popular metal for the formation of C-C bonds, copper was the catalyst of choice for C-C coupling reactions such as Ullmann coupling. [1, 5]

In 1901 Ullmann and Goldberg reported the first Ullmann reaction, which involved the formation of symmetrical biaryl compounds.[5, 6] The initial Ullmann reaction required the use of copper salt, high temperature (>180 ºC), and high loading of metal catalyst; in addition to that, the reaction suffered from low functional group tolerance and long reaction time. A general scheme for Ullmann coupling is shown in scheme 1. As shown, the Ullmann reaction can involve a C-C coupling (A) or C-Y coupling (B), the latter also known as Ullmann coupling.

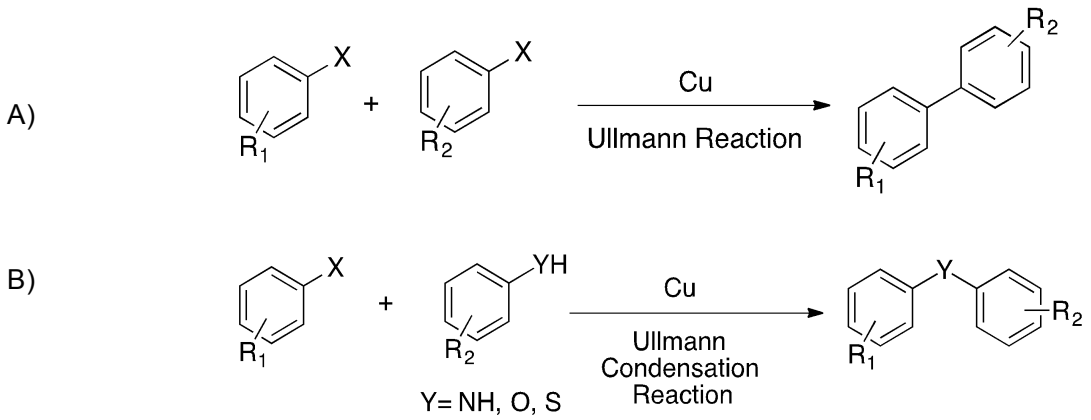

Scheme 3.1. General Ullmann reaction: A) Ullmann C-C coupling or B) Ullmann condensation.

The initial efforts for performing the Ullmann coupling under milder conditions focused on increasing the solubility of the copper catalyst. In 1964, Weingarten [7] observed that the presence of a diester impurity in the solvent he used led to increase of the reaction rate for the coupling between potassium phenoxide and bromobenzene. It was concluded that the diester impurity in the solvent has increased the solubility of the catalyst and therefore increased reaction rate. Later on, in 1975, Cohen described the synthesis of symmetrical biaryls starting from *o*-bromonitrobenzene at room temperature with copper (I) that was soluble in the reaction mixture of acetone and ammonia.[8] In addition to that Buchwald in 1997 demonstrated that phenols could be coupled with aryl bromides in toluene at 100 ºC using soluble copper (I) trifluoromethanesulfonate–benzene with 1-naphthoic acid and ethyl acetate as additives and Cs_2CO_3 as a base. [9] Homogenously, Ullmann cross-coupling reaction could be favored by selecting the right mix of bi-metallic homogenous catalyst where the reagents interact sequentially with each metal center based on their different reactivity. [10]

The mechanism of the Ullmann reaction remained ambiguous, the traditional well accepted mechanism described the formation of an aryl-cuprate intermediate, that after oxidative addition of a second aryl halide can form the final product through reductive elimination.[6, 11]

Several attempts to use heterogeneous catalysts and milder conditions have been done for many years. Ullmann on surface reaction is known to happen on Cu, Ag, and Au, usually by breaking the C-X bonds, then the C-metal coordination bonds form.[12] It is known that the de-halogenation of aryl halides can be performed at room temperature over different metals, including Pd.[12-14]

Natarajan *et al.* had used photo- activated Ullmann coupling on copper surfaces to synthesize a highly conjugated oligothiophene where basically the C-I bond is selectively photo-dissociated to generate a thienyl radical that produces a reactive thienyl-Cu intermediate.[15] Moreover, surface Ullmann coupling of chloropyridines was reported to be catalyzed by poly (N- vinylpyrrolidone) (PVP) stabilized bimetallic Pd-Au nanoclusters under milder conditions. [16, 17] Niu *et al.* demonstrated that Cu_2O supported on hydroxyl group rich TiO_2 precursor can thermally catalyze the C-O bond formation via Ullmann type cross-coupling reaction. Although the study has not been extended to different substrates, it gives up to 95 % yields working at 150 ºC. [18] Supported Palladium based catalyst was found to be effective for Ullmann type couplings for N-arylation of indoles using TEA as base. Additionally, the versatility and cheap production of aryl-chlorides make them suitable candidates for Ullmann reactions. Due their very low reactivity, many attempts to improve their reactivity were made using Pd heterogeneous catalysts.[19]

The development of powerful, inexpensive and commercially available light emitting diodes (LED) and a wide range of photocatalysts, mainly transition metals, has led to increased popularity of the use of light to carry out chemical reactions in the field of homogeneous catalysis.[20-22] In order to expand the use of light for heterogeneous catalysis, there was a need to develop a photo-responsive material that is easily separated and reused. Combining heterogeneous catalysis and light offers a way to carry out the reactions under milder and greener conditions.[23, 24]

The Scaiano group has reported that heterogeneous photo-responsive materials, in specifically palladium-doped titania ($Pd@TiO_2$), can react differently upon UV or visible light irradiation yielding different products with different wavelengths for the same reaction mixture.[25, 26]

During this thesis, we were able to demonstrate that Ullmann reaction can be heterogeneously photocatalyzed by dual UV-visible excitation of Pd@TiO_2, an easy to separate and reuse material. We show here that visible light alone does not initiate the reaction, however, combining UV light with 465 nm visible light leads to improved activity, yields, and selectivity towards cross-combination products. The reaction involves photoresponsive intermediate that is associated to the catalyst, where Pd nanostructures can absorb visible radiation, while UV absorption is dominated by the TiO_2. Therefore, a hybrid photo-responsive material shows different reactivity when irradiated with two color light sources. By selecting the optimal light wavelengths, one can tune the selectivity toward different products.

3.2 Results and Discussion

In the first attempt to perform coupling between two aryl halides, reaction conditions were inspired from a different publication that reported C-C coupling. [25] Pd@TiO_2 was chosen as catalyst as it has been known to catalyze many reactions that involves C-C coupling. Results of the first attempted Ullmann coupling are reported in table 3.1

Table 3.1. First attempted Ullmann Coupling

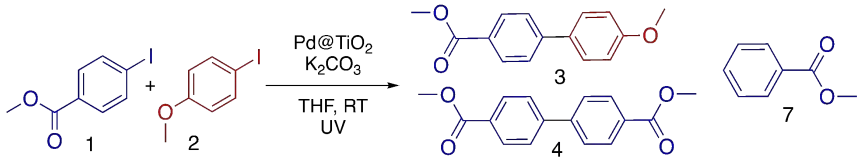

Entry	Solvent	Time (h)	1 (%Conv)	3 (%Yield)	4 (%Yield)	7 (%Yield)
i	THF	3	100	42	48	15

Reaction conditions: 0.1 mmol **1**, 0.2 mmol of **2**, 0.5 mmol of K_2CO_3 and 20 mg of Pd@TiO_2 catalyst in 5 mL of THF under Argon. Samples were irradiated using 368 nm LED working at 0.4 W cm^{-2}. Yields and conversions were calculated by GC-FID using t-butylbenzene as external standard.

Having found that the reaction is possible under these conditions, we aimed to improve the selectivity toward the cross coupling product by changing one variable at a time. The first thing that was done is testing the reaction with different solvents table 3.2.

It was found that the solvent plays a very essential role in the reaction. THF was found to be the only solvent that offer coupling products (table 3.2, entry I), while methanol

yielded only the reduction product 7 due to the formation of strongly reducing •CH_2OH that produces H_2 (table 3.2, entry ii). [25-28] Moreover, MeCN and DCE were shown to be inert solvents as no reaction happens after 24 hours irradiation, (table 3.2, entries iii, and IV).

Table 3.2. Screening of solvents for C-C coupling

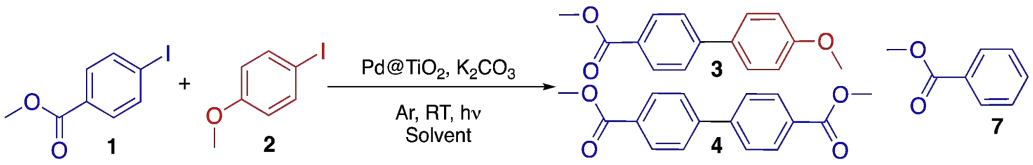

Entry	Solvent	Time (h)	1 (%Conv)	3 (%Yield)	4 (%Yield)	7 (%Yield)
i	THF	3	100	42	48	15
ii	MeOH	24	100	ND	ND	100
iii	MeCN	24	0	ND	ND	ND
iv	DCE	24	0	ND	ND	ND

Reaction conditions: 0.1 mmol **1**, 0.2 mmol of **2**, 0.5 mmol of K_2CO_3 and 20 mg of Pd@TiO_2 catalyst in 5 mL of solvent under Argon. Samples were irradiated using 368 nm LED working at 0.4 W cm^{-2}. Yields and conversions were calculated by GC-FID using t-butylbenzene as external standard.

Furthermore, running the reaction with inert solvents such as MeCN, then adding 1 equivalent of THF was enough to get the reaction to proceed with acceptable yields in less than 5 hours (Table 3.3). THF is able to form tetrahydrofuranyl radical (vide infra).[29] as confirmed using TEMPO as a radical trapping agent (Table 3.4 and Figure 3.1).

Table 3.3. Ullmann reaction in the absence and presence of THF

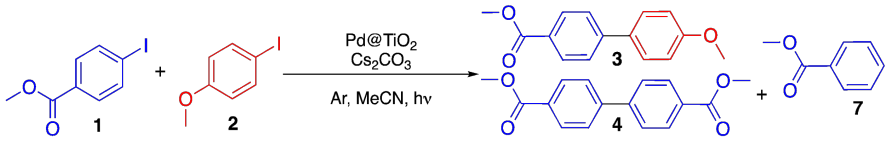

Entry	Solvent	Eq THF	Time (h)	1(%Conv)	3 (%Yield)	4 (%Yield)
i	MeCN	0	0	ND	ND	ND
ii	MeCN	1.5	1.5	31	31	ND
iii	MeCN	1.5	4.5	57	50	7

Reaction conditions: 0.1 mmol **1**, 0.2 mmol of **2**, 20 mg of Pd@TiO_2 catalyst, 2 eq. of Cs_2CO_3 in 5 mL of MeCN upon irradiation at 368 nm (0.4 Wcm^{-2}) and 465 nm (1.0 Wcm^{-2}). Yields and conversions were calculated by GC-FID using t-butylbenzene as external standard.

Table 3.4. Ullmann reaction in the presence of TEMPO

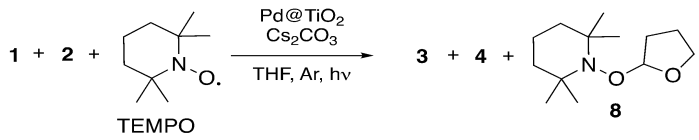

Entry	mmol of reagents			Time (h)	% yield		
	1	**2**	TEMPO		**3**	**4**	**8**
i	0.1	0.2	0.2	1	ND	ND	39
ii	0.1	0.2	0.2	4	12	6	70
iii	0.1	0.2	0.2	7	73	29	>99
iv	0	0	0.2	7	--	--	>99

Reaction conditions: 20 mg of Pd@TiO_2 catalyst, 2 eq. of Cs_2CO_3 in 5 mL of THF upon irradiation at 368 nm (0.4 Wcm^{-2}) and 465 nm (1.0 Wcm^{-2}). Yields and conversions were calculated by GC-FID using t-butylbenzene as external standard.

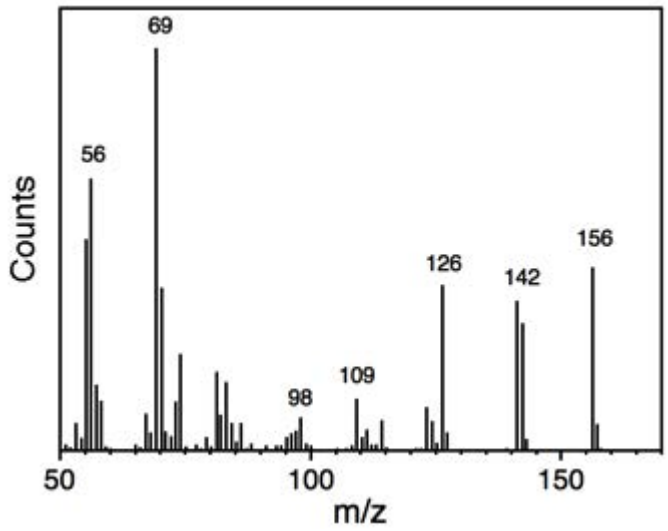

Figure 3.1. Mass spectrum of TEMPO-THF radical trapping adduct (Table 3.4, product **8**)

The presence of TEMPO inhibited the Ullmann reactions (Figures 3.2). [30] A preliminary initial rate calculation suggests the formation of tetrahydrofuranyl radical is around 4.4 10^{-5} M s^{-1} under our conditions, and therefore, it is the rate-limiting step for the reaction.

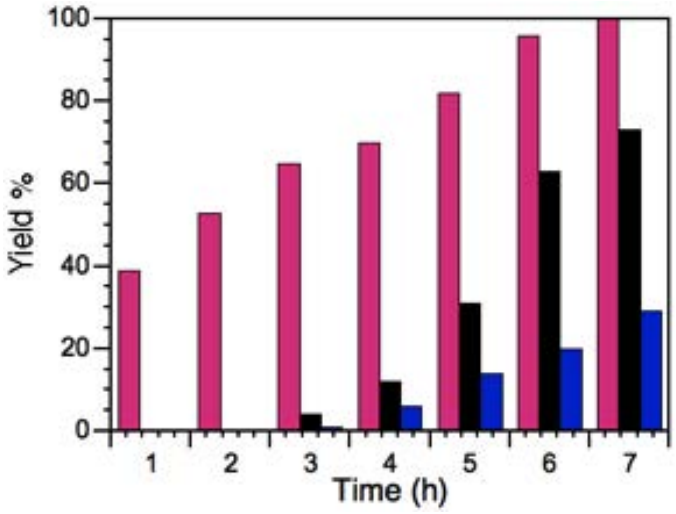

Figure 3.2. Kinetics of the Ullmann reaction in the presence of TEMPO showing the yield of TEMPO-THF adduct **8** (pink), cross-coupling product **3** (black) and homo-coupling product **4** (blue). Reaction is performed under irradiation at 368 nm (0.4 Wcm^{-2}) and 465 nm (1.0 Wcm^{-2}).

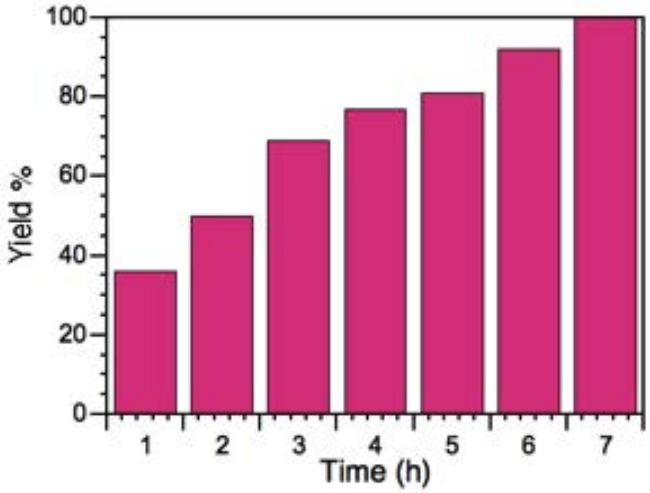

Figure 3.3. Kinetics of the formation of TEMPO-THF adduct **8.** Reaction is performed under irradiation at 368 nm (0.4 Wcm^{-2}) and 465 nm (1.0 Wcm^{-2}).

Having understood the important role of THF for the Ullmann reaction, different bases were evaluated in order to improve selectivity toward coupling (Table 3.5). In the absence of base, only reductive product 7 was observed. Using TEA and DABCO as bases led to zero conversion after 24 hours irradiation time. Both K_2CO_3 and Cs_2CO_3 proved to be efficient for the Ullmann coupling; however, Cs_2CO_3 favors the coupling product and shows negligible amount of reductive product.

Table 3.5. Screening of different bases

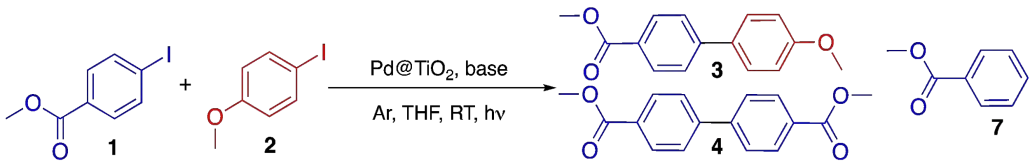

Entry	Base	Light (nm)	Equivalents	Time (h)	1 (%Conv)	3 (%Yield)	4 (%Yield)	7 (%Yield)
i	none	368	-	24	100	ND	ND	100
ii	K_2CO_3	368	1.5	3	92	6	11	75
iii	K_2CO_3	368	3	3	100	9	36	60
iv	K_2CO_3	368	5	3	100	42	48	15
v	DABCO	368	5	24	0	ND	ND	ND
vi	TEA	368	5	24	0	ND	ND	ND
vii	Cs_2CO_3	368	5	3	100	50	48	traces
viii	Cs_2CO_3	368+465	5	1	100	77	22	ND
ix	Cs_2CO_3	368+465	2	1	100	80	20	ND

Reaction conditions: 0.1 mmol Methyl-Iodobenzoate, 0.2 mmol of Iodoanisole, 20 mg of Pd@TiO_2 catalyst in 5 mL of THF under Ar atmosphere upon irradiation at 368 nm (0.4 Wcm^{-2}). Yields and conversions were calculated by GC-FID using t-butylbenzene as external standard. DABCO: 1,4-Diazabicyclo[2.2.2]octane . TEA: triethylamine.

In order to assess the importance of light on the Ullmann coupling, the reaction was carried out under different conditions summarized in table 3.6 and Figure 3.5. The reaction was completed in a very short time (100% conversion in 1h) when UV+ Blue lights were used simultaneously. The UV light alone is able to initiate the reaction but it favors homocoupling product 4, the mix of UV and Blue is required to achieve the high selectivity toward the cross- coupling product 3 as the Blue light is responsible for this selectivity. Irradiating with blue light at high power for long time led to some products with obvious selectivity toward the cross coupling 3. Carrying out the reaction in the dark or under reflux for 24 hours led to no conversion. Emission spectra of the UVA and 465 nm are shown is figure 3.4

Table 3.6. Light screening

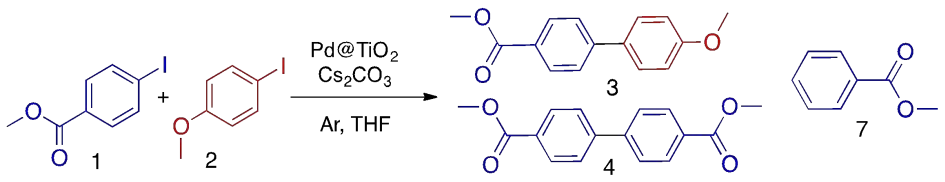

Entry	Light (nm)	Temperature (ºC)	Time (h)	**1** (Conv%)	**3**(%Yield)	**4**(%Yield)	**7**(%Yield)
i	UV	50	1	60	10	20	28
ii	UV + Blue	60	1	100	80	20	ND
iii	Blue	50	24	<5	traces	ND	ND
iv	Blue*	60	24(48)	39(65)	33(52)	8(15)	ND
v	Dark	50	24	0	ND	ND	ND
vi	Dark	60	24	0	ND	ND	ND
vii	Dark	77 (Reflux)	24	0	ND	ND	ND

Reaction conditions: 0.1 mmol Methyl-Iodobenzoate, 0.2 mmol of Iodoanisole, 20 mg of Pd@TiO_2 catalyst, 2 eq. of base in 5 mL of THF under Ar atmosphere. Yields and conversions were calculated by GC-FID using t-butylbenzene as external standard. Irradiation at 368 nm = 0.4 Wcm^{-2} and at 465 nm = 1.0 Wcm^{-2}. *1.6 Wcm^{-2}

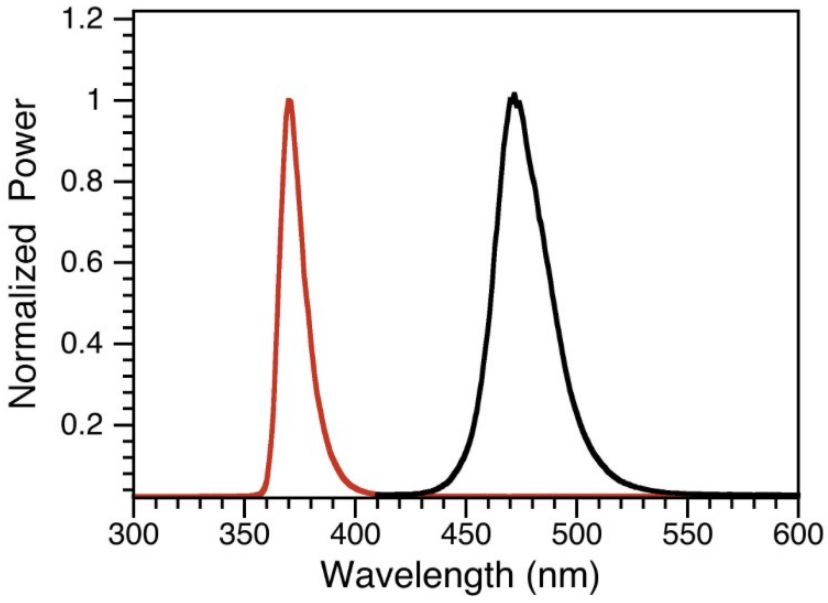

Figure 3.4. Emission spectra of light-emitting diodes centered at 368 nm (red) and 465 nm (black). Normalized power.

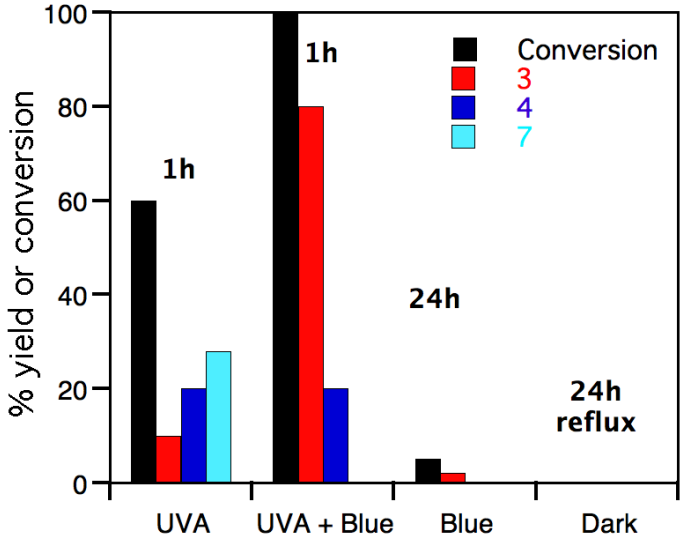

Figure 3.5. Screening of light conditions using reaction in Scheme 1. **UVA**: irradiation for 1 h using 368 nm LED at 0.4 Wcm^{-2}; **UVA + blue**: irradiation for 1 h using 368 nm LED at 0.4 Wcm^{-2} and 465 nm LED at 1.0 Wcm^{-2}; **blue:** Irradiation for 24 h using 465 nm LED at 1.6 Wcm^{-2}; and **dark:** Reflux at 77 ºC for 24 h.

Having found that the usage of 465 nm improved the selectivity toward the cross coupling we tested different visible lights to find the best combination of UV and visible light. Action spectra were obtained by carrying out the test reaction using different wavelengths of visible light. The light source screening was performed using UVA light (368 nm LED) combined to different visible light sources, namely 465 nm, 500 nm, 525 nm, 590 nm, and 630 nm; with adjusting all irradiation sources to the same power,i.e. 0.2 W/cm^2 (Figure 3.6). Table 3.7 shows the yields obtained after one hour of irradiation under the conditions described.

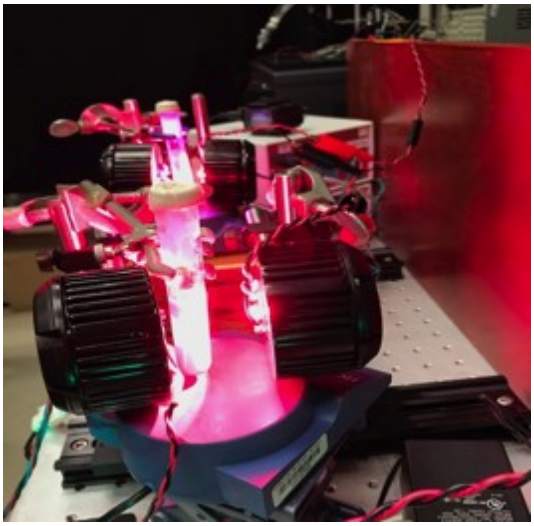

Figure 3.6 Reaction setup showing the 2 LED sources (illustrated with 368 and 590 nm) pointing into the sample, ensuring same irradiance (0.2 Wcm^{-2}) and vigorous stirring

Table 3.7. Percentage yield for cross-coupling product 3 and homo-coupling product 4 of the reaction run with two-color light working at 0.2 W/cm^2

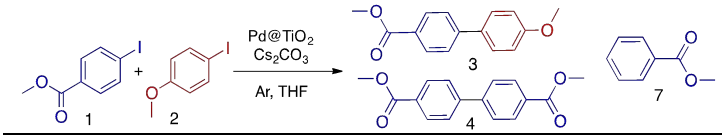

Entry	λ_1	λ_2	Yield % 3	Yield % 4
i	368	368	19±5	52±1
ii	368	465	42±1	36±2
iii	368	500	25±7	52±9
iv	368	525	30±6	48±1
v	368	590	24±6	43±7
vi	368	630	27±4	51±8

It was found that the optimal results are obtained when a mix of 368nm and 465 nm is used (table 3.5, entry ii). Moreover, it was found that the intensity of the lights has a great effect on the reaction. If the intensity of the blue light is kept constant at 1.0 W cm^{-2}, and the intensity of the UV light is increased, both conversion and yield are increased. However, when UV light is kept constant at 0.4 Wcm^{-2} the change of the blue light intensity not only increases the conversion and yield of the reaction, it also favors cross- coupling product formation. (Figure 3.7)

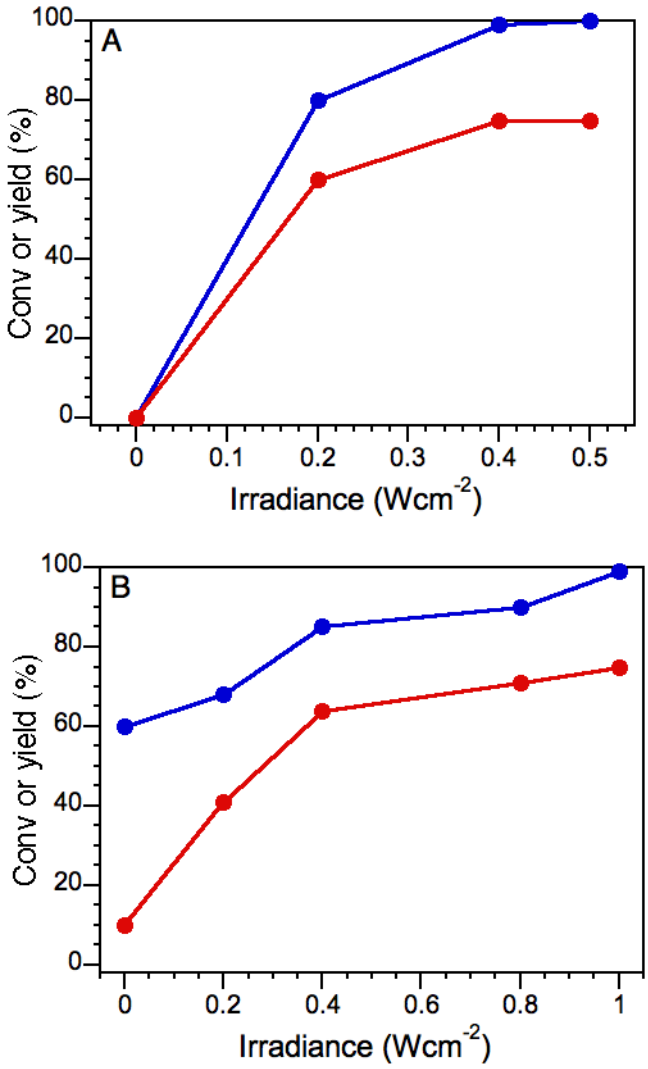

Figure 3.7 Conversion (blue) and yield (red) of cross-coupling product versus light intensity obtained after 1 h exposure: (A) keeping 465 nm working at 1.0 W/cm^{-2} and 368 nm at various intensities; (B) keeping 368 nm working at 0.4 W/cm^{-2} and 465 nm at various intensities

In an attempt to generalize these observations, we evaluated the use of different catalysts such as Au or Cu- decorated TiO_2, bimetallic materials and the use of different supports such as Nb_2O_5 or nano-diamonds (CND). It was found that both TiO_2 and Pd are essential for the reaction to proceed (table 3.8). Whereas Pd@TiO_2 can serve as catalyst for aryl iodide derivatives, bimetallic systems, such as Pd@Au@TiO_2, can extend the scope towards other aryl halides such as bromides.

Table 3.8. Catalyst Screening

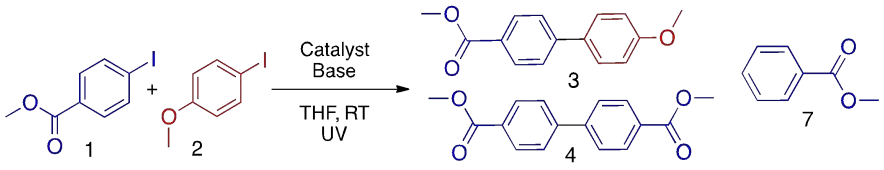

10	Catalyst	Atm	Time (h)	**1** (% Conv)	**3** (%Yield)	**4** (%Yield)	**7** (% Yield)
i	$Pd@TiO_2$	Ar	2[a]	100	20	54	23
ii	$Pd@TiO_2$	Ar	1	100	80	20	ND
iii	$Pd@TiO_2$	Air	2	100	40	60	ND
iv	$Cu@TiO_2$	Air	24	0	ND	ND	ND
v	$Cu@TiO_2$	Ar	24	0	ND	ND	ND
vi	$Au@TiO_2$	Air	24	0	ND	ND	ND
vii	$Au@TiO_2$	Ar	24	0	ND	ND	ND
viii	$Cu@Pd@TiO_2$	Air	2	100	56	29	5
ix	$Cu@Pd@TiO_2$	Ar	5	0	ND	ND	ND
x	$Cu@Au@TiO_2$	Ar	24	0	ND	ND	ND
xi	$Cu@Au@TiO_2$	Air	24	0	ND	ND	ND
xii	$Pd@Au@TiO_2$	Ar	1.5	100	77	10	13
xiii	$Pd@Au@TiO_2$	Air	1.5	100	50	40	7
xiv	TiO_2	Ar	1	0	ND	ND	ND
xv	TiO_2	Ar	24	100	ND	ND	100
xvi	Pd@CND	Ar	24	0	ND	ND	ND
xvii	$Pd@Nb_2O_5$	Ar	24	0	ND	ND	ND

Reaction conditions: 0.1 mmol Methyl-Iodobenzoate, 0.2 mmol of Iodoanisole, 20 mg of catalyst, 2 eq. of Cs_2CO_3 in 5 mL of THF upon irradiation at 368 nm (0.4 Wcm^{-2}) and 465 nm (1.0 Wcm^{-2}). Yields and conversions were calculated by GC-FID using t-butylbenzene as external standard. [a]Irradiation with only 368 nm LED.

The scope of the reaction can be evaluated by dividing the products into two systems The first system is push-pull where one aryl group is substituted with an electron donating group (EDG) and the other one with an electron withdrawing group (EWG). The second system is pull-pull or push-push where substituents on the aryl halides are both EWG or EDG. It was found that for push-pull systems with moderate EWG such as 4-methyl iodobenzoate the cross-coupling reaction is favored under the conditions studied here. Interestingly, no condensation products were found when substituents such as $–NH_2$ were used.[31] EDGs in *ortho* positions usually favor the homo-coupling product of the *para*-substituted aryl iodide. However, when a strong EWG was used the selectivity towards the homo-coupling product increased. While the pull-pull system seemed to be inactive under the conditions studied, the push-push systems offered a great conversion and yields in 2-3 h. Scheme 2 and table 3.9 present these finding and a comprehensive characterization of the product scope is shown in the Appendix

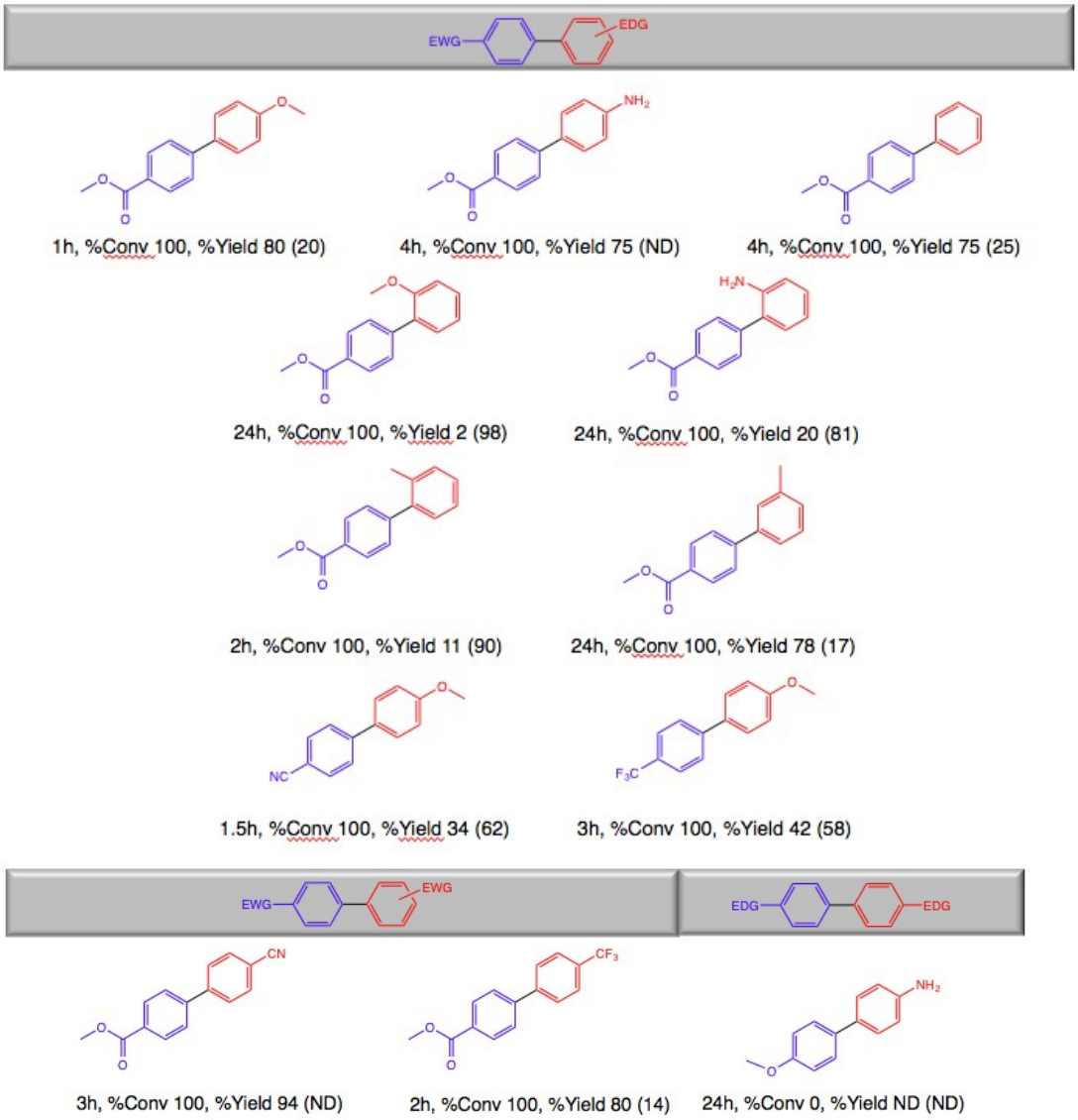

Scheme 2: Scope of the Ullmann reaction under two-color heterogeneous photocatalysis. Yields and conversions were calculated by GC-FID using t-butylbenzene as external standard. Values between brackets correspond to the yield of the homo- coupling product of limiting reagent (blue).

Table 3.9. Scope of the reaction

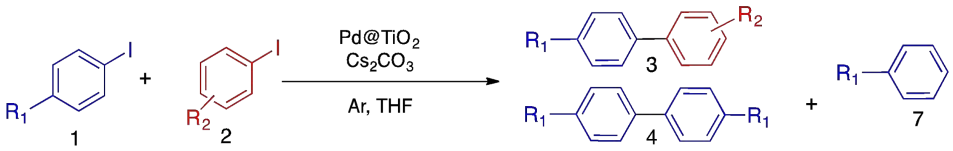

Entry	R_1	R_2	Time (h)	1 (% Conv)	3 (%Yield)	4 (%Yield)	7 (% Yield)
R_1=EWG & R_2=EDG							
i	-C(O)OCH_3	-*p*-OCH_3	1	100	80 (67)	20 (12)	ND
ii	-C(O)OCH_3	-*p*-NH_2	4	100	75	ND	22
iii	-C(O)OCH_3	-H	4	100	75 (70)	25 (17)	ND
iv	-C(O)OCH_3	-*o*-OCH_3	24	100	2	98 (80)	ND
v	-C(O)OCH_3	-*o*-NH_2	24	100	20	80 (65)	ND
vi	-C(O)OCH_3	-*o*-OH	24	15	ND	ND	10
vii	-C(O)OCH_3	-*o*-CH_3	2	100	11	90 (83)	ND
viii	-C(O)OCH_3	-*m*-CH_3	24	100	78 (71)	17	ND
ix	-CN	-*p*-OCH_3	1.5	100	34 (27)	62 (50)	ND
x	-CF_3	-*p*-OCH_3	3	100	42 (31)	58 (53)	ND
R_1=EWG & R_2=EWG							
xi	-C(O)OCH_3	-*p*-CN	3	100	94 (75)	ND	ND
xii	-C(O)OCH_3	-*p*-CF_3	2	100	80 (57)	14 (9)	ND
xiii	-C(O)OCH_3	-*p*-NO_2	24	0	ND	ND	ND
xiv	-C(O)OCH_3	-*o*-NO_2	24	20	ND	5	15
R_1=EDG & R_2=EDG							
xv	-OCH_3	-*p*-NH_2	24	0	ND	ND	ND

Values between brackets correspond to isolated yields

The reusability of the catalyst shows 100 % conversion after the 4 cycles tested. The catalyst kept its great selectivity towards cross-coupling product **3** for at least 3 cycles then the selectivity toward the cross coupling has diminished due to change in the oxidation state of Pd. (Figure 3.8).

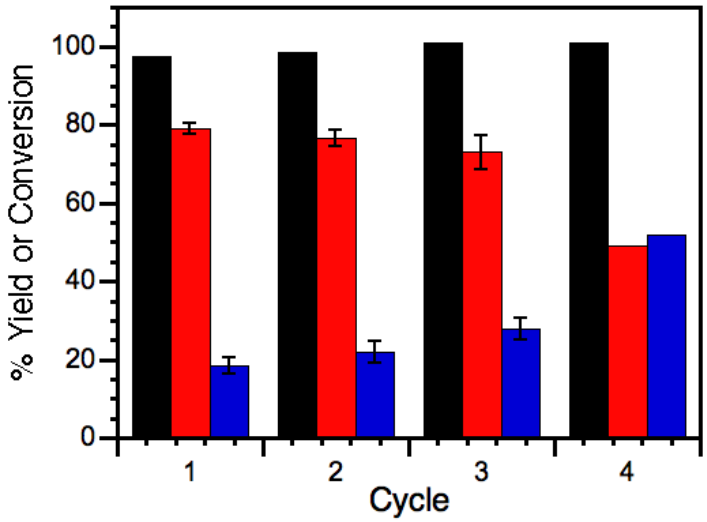

Figure 3.8. Conversion (black) and yields for cross-coupling product **3** (red) and homo- coupling product **4 (**blue) after several catalytic cycles.

Moreover, leaching tests was performed to determine whether the reaction happens in the homogeneous or heterogeneous phase. The leaching test was done as follows, after photo-initiation of the reaction in the presence of the catalyst, the solids were separated by filtration, and the filtrate further irradiated under the same conditions. The reaction stops after removal of the solid catalyst suggesting that no catalytic species leaks into the homogeneous phase. From figure 3.9 it can be concluded that the reaction happens in the heterogeneous phase as the reaction stopped immediately after the solid catalyst was removed, confirming that no catalytic species have leached to the homogeneous phase.

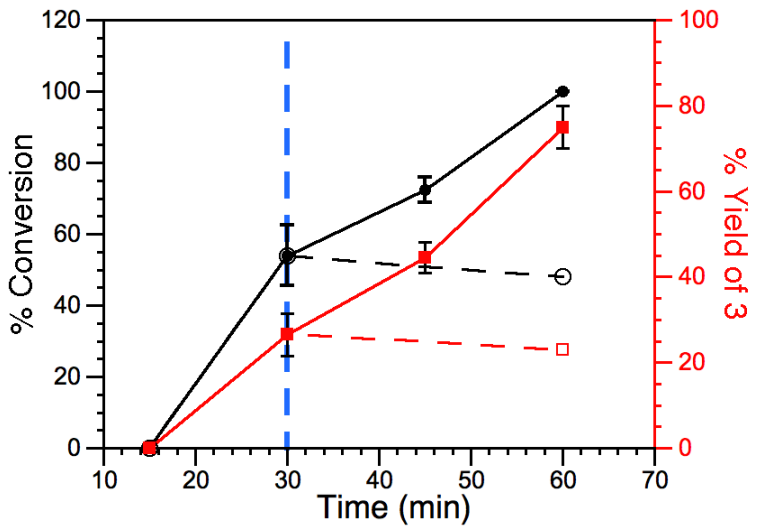

Figure 3.9. Leaching test of Pd@TiO_2: Catalytic reaction is performed in the presence of catalyst. After 30 min of irradiation (blue dash-line), the reaction mixture is separated from the catalyst and the filtrate is irradiated for another 30 min. The figure shows the % conversion and yield obtained in the presence of catalyst (full markers) and in the filtrate (hollow markers). No catalytic species in the filtrate are detected while the non-filtered reaction continues to complete conversion.

Based on the results that were obtained we propose the reaction mechanism shown in Scheme 3. Upon UVA excitation an electron gets promoted from the valence band VB to the conduction band CB creating electron- hole pair on the TiO_2.[26, 32] PdNP, traps the electron from the conduction band (CB) and extends the lifetime of the electron- hole pair through energy and spatial separation. [33] THF quenches the hole in the valence band (VB) forming tetrahydrofuranyl radical **I** (step **A**) [29, 34] and a proton. The base then captures the proton (Cs_2CO_3 in this system, step **B**). When the base is not present, the proton can be reduced on the Pd surface yielding surface Pd-H species,[26] yielding the reduction product 7 (Table 3.5 entry i) .The formation of radical **I** as a true, free and mobile radical is proved by adding TEMPO that quantitatively traps the radical to produce **8** (Table 3.4). These reactions are known to occur with rate constants exceeding 10^8 $M^{-1}s^{-1}$. [35] It was noticed that the Ullmann reaction is inhibited until the TEMPO runs out (Table 3.4 and Fig 3.2). In the absence of TEMPO, radical **I** can transfer its electron to either of the two aryl iodides present in the system. As both aryl iodides exist in comparable concentrations, it is acceptable to hypothesize that the one with electron withdrawing substitution (EW) will normally be favored in the competition

illustrated in step **C**. Note the formation of H^+, a strong acid is again scavenged by base (step **B**). The aryl radical anion formed (**III**) is expected to live very shortly [36] and loses iodide before, or simultaneously, with the aryl radical associating with the Pd@TiO_2 surface (step **D**). The kinetics of phenyl radical with THF are known to be around 5 x 10^6 $M^{-1}s^{-1}$, or about 1000 times slower than diffusion control and thus, even a free aryl radical has a reasonable chance of finding the Pd@TiO_2 surface. The aryl iodide with electron donating (ED) substituents is more likely the favored aromatic species to associate with the Pd@TiO_2 surface, as other electron rich aromatics are known to do.[37] It is possible that this association occurs at both the TiO_2 and the Pd surface, but the latter is more important from a mechanistic point of view (step **E**). The oxidative addition of the second aryl halide (assisted by tetrahydrofuranyl radical **I**) can furnish product through a photo reductive elimination.[38] Thus, visible light makes the final stage of electron transfer from the PdNP to the remaining iodide possible, paving the way for cross-coupling product formation (step **F**).

It is important to note that when the 465 nm LED is absent the selectivity shift toward the homocoupling. Even though that the Pd is not playing a catalytic activity when only UVA LED is used, the Pd will slow down the electron- hole recombination which is important for the formation of the homocoupling product.

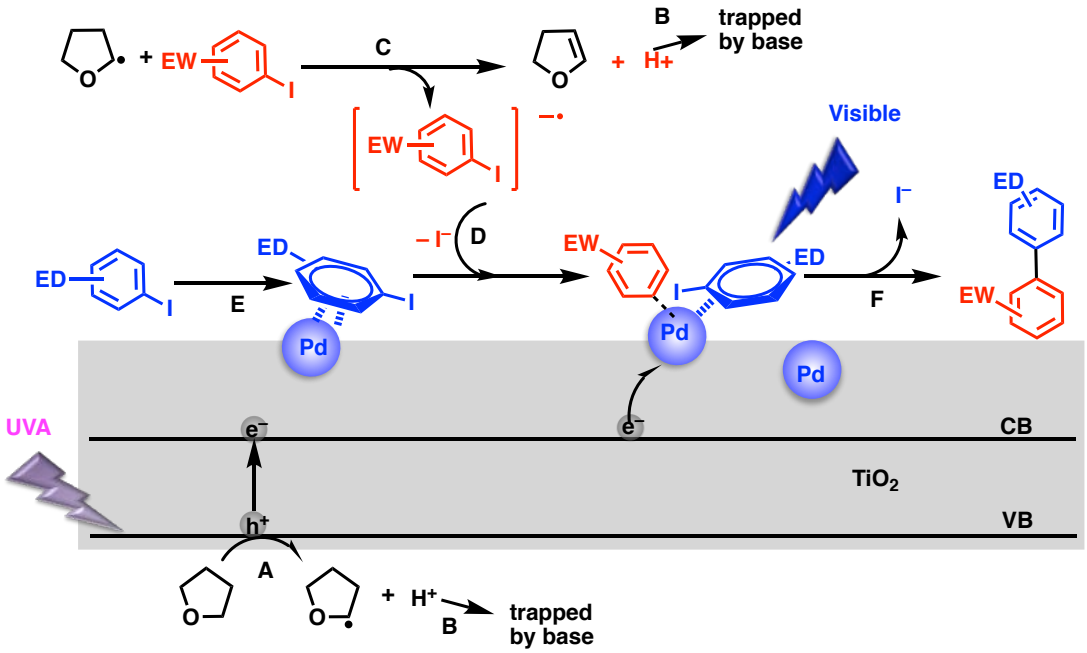

Scheme 3: Proposed mechanism of the photocatalytic Ullmann cross-coupling reaction shows the expected formation of the electron-hole pair on the TiO_2 surface upon UVA excitation. Under the reaction conditions THF can easily form the tetrahydrofuranyl radical **I** (**A**) – a very good electron donor – and H^+ – more likely scavenged by base (**B**).This radical can easily donate an electron to the aryl iodide and assist the formation of the intermediate **III** (**C**), which finds its way to Pd surface through **D**. On the other hand, electron can be trapped by Pd, which in turn can form the Aryl-Pd intermediate (**E**), possibly with the most electron donor substituted aryl iodide. The oxidative addition of the second aryl halide (assisted by tetrahydrofuranyl radical I) can furnish Aryl-Pd-Aryl structure, to finally give rise to product through photo reductive elimination (F).

The importance of visible light deserves some comment. Recent work by Zhu and coworkers has demonstrated that non-plasmonic NPs, such as PdNP, can induce photocatalysis in the visible region by hot-electron processes.[38] Also, the efficiency of visible light in those processes not only depends on the nature of the photocatalyst, but also in the orbital energy of the reagents involved in the reaction,[38] which for the same type of reaction can differ drastically depending on electronic substitution of the reagents. [39] In the context of these seminal studies, the formation of C-C bonds in this system and the role of the visible irradiation fall in line with observations in a variety of other photoactive systems. Thus, visible light can catalyze the reductive elimination (**F**) favoring cross- or homo-coupling products according to the electronic substitution of the reagents. Finally, the fate of iodide in the system is also interesting, as it can find its way to yield iodine, readily detectable with a conventional starch test Figure 3.10 The required oxidation is likely to occur by TiO_2 hole scavenging by iodide,[40] a process that may gain some importance as iodide accumulates towards the end of the reaction.

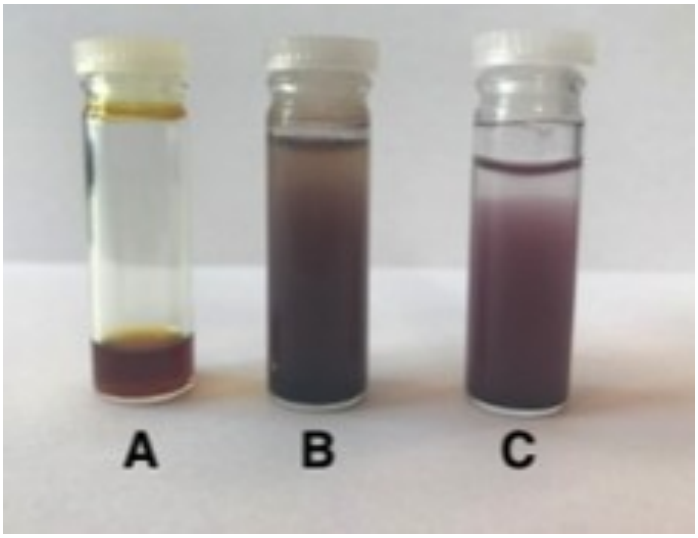

Figure 3.10. Starch-Iodine test. A) Reaction mixture; B) Reaction mixture plus starch; C) iodine solution plus starch.

3.3 Experimental section

3.3.1 Materials and instruments

Unless otherwise specified, all chemicals were purchased from Sigma-Aldrich or Fisher Scientific and used without further purification. TiO_2 P25 was purchased from Univar Canada. 1% AuNP@TiO_2 was purchased from Strem Chemicals and ground using a mortar prior to use. Irgacure-2959 (I-2959) was a gift from BASF.

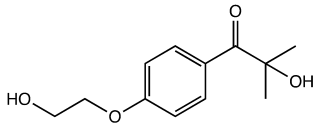

I-2959

Transmission electron microscopy (TEM) images and Energy-dispersive X-ray spectroscopy (EDS) were performed on a JEM-2100F FETEM (JEOL) operating at 200 kV. Samples were prepared by drop casting a water dispersion of the material onto a 200 mesh copper grid coated with a carbon film. X-ray photoelectron spectroscopy (XPS) was recorded using Kratos analytical model Axis Ultra DLD, using monochromatic aluminum Ka X-rays at 140 W. XPS data was analyzed using CasaXPS software, Version 2.3.15 and all fittings obtained using a Gaussian 30% Laurentian and a Shirley baseline. Diffuse reflectance (DR) measurements were carried out in VARIAN Cary 7000 UV-VIS Spectrophotometer coupled with an integrating sphere accessory. UV irradiation used for catalyst synthesis was performed in a Luzchem photoreactor equipped with UVA bulbs (typically operated with 14 bulbs, corresponding to ~75 Wm^{-2} with ~ 4% spectral contamination). Light-emitting diodes (LEDs) of 10 W from LedEngin were used for the photocatalytic C-C coupling in the UV (centered at 368 nm) and visible region (centered at 465 nm) working at 700 mA (Figure 3.4).

Quantification was carried out in a Perkin Elmer, Claurus Gas Chromatograph coupled to a Flame Ionization Detector (FID) and a DB-5 column (30 m length, 0.320 mm diameter, 0.25 μm film) using Helium as a carrier gas and t-Butyl benzene or Stilbene as external standard.

Isolation of the products was performed by preparatory thin layer chromatography (PTLC) using 1000 μm thick glass baked TLC plates. All ^{1}H NMR and the ^{13}C NMR spectra were recorded on a Bruker AVANCE 400 spectrometer expressing the chemical shifts in ppm relative to the H-signal of the tetramethylsilane (TMS) and to the C-signal of the

deuterated chloroform as internal standard, respectively. Steady-state absorbance and fluorescence measurements were recorded on a CARY-60 spectrophotometer and a Photon Technology International (PTI) fluorimeter, respectively. Mass spectra were collected in an Agilent 6890-N Gas Chromatograph with an Agilent 5973 mass selective detector calibrated with acetophenone.

3.3.2. Catalyst preparation

Pd@TiO_2: Palladium supported on TiO_2 was prepared by photodeposition of PdNP onto TiO_2 (P25) as previously reported. In brief, TiO_2 (500 mg) and $PdCl_2$ (11 mg, for 2 wt% Pd@TiO_2) were dispersed in 200 mL of Milli-Q water, sonicated for 20 minutes and irradiated in a Luzchem photoreactor equipped with 14 UVA bulbs for 8 hours with vigorous stirring. The brownish slurry was centrifuged and washed with Milli-Q water at least five times to remove unreacted $PdCl_2$ and dried overnight in a desiccator under vacuum. The resulting dark-gray powder was characterized by TEM, XPS, and DR. The catalyst was kept under argon to ensure reliable activity.

Cu@TiO_2: The copper supported on TiO_2 was prepared by photodeposition of Cu utilizing Irgacure-2959 (I-2959) following the reported procedure.[32] Briefly, TiO_2 (160 mg), $CuCl_2.2H_2O$ (64 mg, for 5 wt% Cu@TiO_2) and I-2959 (11.2 mg) were dispersed in 100 mL of milliQ water. The mixture was purged with Argon for 20 min, sonicated and then irradiated in a Luzchem photoreactor equipped with 14 UVA bulbs for 5 h under vigorous stirring. The bluish slurry was centrifuged and washed with Milli-Q water at least five times and then dried in a desiccator overnight under vacuum. The resulting light-blue powder was characterized by TEM, XPS, and DR. The catalyst was kept under argon to ensure reliable activity.

Cu@Pd@TiO_2: Copper supported on Pd@TiO_2 was prepared following the same strategy used for the synthesis of Cu@TiO_2, photodeposition of Cu onto the as prepared Pd-TiO_2. In brief, Pd@TiO_2 (160 mg), $CuCl_2$ (21 mg) and I-2959 (56 mg) were dispersed in 100 mL of Milli-Q water, purged with Argon for 20 minutes then sonicated for 20 minutes and irradiated in a Luzchem photoreactor equipped with 14 UVA bulbs for 5 hours with vigorous stirring. The grey slurry was centrifuged and washed with Milli-Q water at least five times and dried overnight in a desiccator under vacuum. The resulting dark-gray powder was characterized by TEM, XPS, and DR. The catalyst was kept under argon to ensure reliable activity

Pd@Au@TiO_2: Palladium supported on commercial Au@TiO_2 was prepared following the procedures described for Pd@TiO_2 preparation. Thus, Au@TiO_2 (200 mg) and $PdCl_2$ (10.2 mg, for 1% Pd@Au@TiO_2, w/w%) were dispersed in 80 mL of Milli-Q water, sonicated for 30 minutes and irradiated in a Luzchem photoreactor equipped with 14 UVA bulbs for 3 hours with vigorous stirring. The grey slurry was centrifuged and washed with Milli-Q water at least five times to remove unreacted $PdCl_2$ and dried overnight in a desiccator under vacuum. The resulting dark-gray powder was characterized by TEM, XPS, and DR. The catalyst was kept under argon to ensure reliable activity.

3.3.3 Catalytic activity

After an extensive screening of conditions the catalytic reaction was carried out utilizing the following general procedure: 20 mg of catalyst, 0.1 mmol of **1**, 0.2 mmol of **2**, 0.2 mmol base, 5 mL THF were sonicated for 10 min to ensure uniform dispersion. The reaction mixture was then purged with Ar for another 10 min and irradiated with a 368 nm and a 465 nm LEDs working at 0.4 Wcm^{-2} and 1.0 Wcm^{-2}, respectively, until complete conversion of **1**, or up to 24 h. After reaction was complete the catalyst was filtered out and the solvent completely evaporated in a rota-vapor system at 60 ºC. The reaction mixture was re-dissolved in ethyl acetate and the base extracted with water. The solvent was evaporated and the products dissolved in DCM. Quantification of the products was done by GC-FID. Finally, the cross-coupling product was separated by preparative TLC and characterized by ^{1}H and ^{13}C NMR, Mass spectrometry and UV-Vis and fluorescence spectroscopy.

Light source screening

The light source screening was performed using UVA light (368 nm LED) combined to different visible light sources, namely 465 nm, 500 nm, 525 nm, 590 nm, and 630 nm; adjusting both irradiation sources to the same power, i.e. 0.2 Wcm^{-2}. Table

3.7 shows the yields obtained after one hour of irradiation under the conditions described.

Radical trapping reaction

The presence of the tetrahydrofuranyl radical was determined by using (2,2,6,6-Tetramethylpiperidin-1-yl)oxyl (TEMPO) as a radical trapping agent. In brief, 2 eq. of TEMPO were added to the reaction conditions described above and the reaction followed until complete conversion. Products were characterized by GC-MS Figure 3.1 and quantified by GC-FID Figure 3.2.

Leaching test

The reaction mixture was prepared as described above. After 30 min of irradiation the catalyst was filtered off and the reaction mixture filtrate was purged with Argon and irradiated for another 30 min. figure 3.9 shows no increase in the conversion and yield percentages following filtration confirming that no catalytic species are present in the homogeneous phase.

Starch test conditions

An aqueous solution of iodine (0.1 M) was prepared by mixing 1.5 g of KI and 1.27 g of Iodine to the moistened KI and adding 50 mL of water gradually while the solution is stirring till the Iodine is fully dissolved. This solution was mixed with aqueous starch solution (1 w/v %) to give the dark blue/violet solution shown in Fig 3.10, C. The same was performed for the reaction mixture solution (Fig 3.10, B). Similar results were found when homocoupling conditions were favored.

Catalyst Recyclability

The Pd@TiO_2 was tested for reusability after 4 catalytic cycles. Following irradiation, the samples were placed in a 15 mL centrifuge tube, and centrifuged at 6500 rpm for 15 min to recover the catalyst. The catalyst was subjected to centrifugation- rinsed-stirring steps five times using THF as rinsing solvent.

3.4 Catalyst characterization

Each one of the designed catalysts was characterized by TEM, EDS, DR, XPS and ICP

Transmission electron micrographs

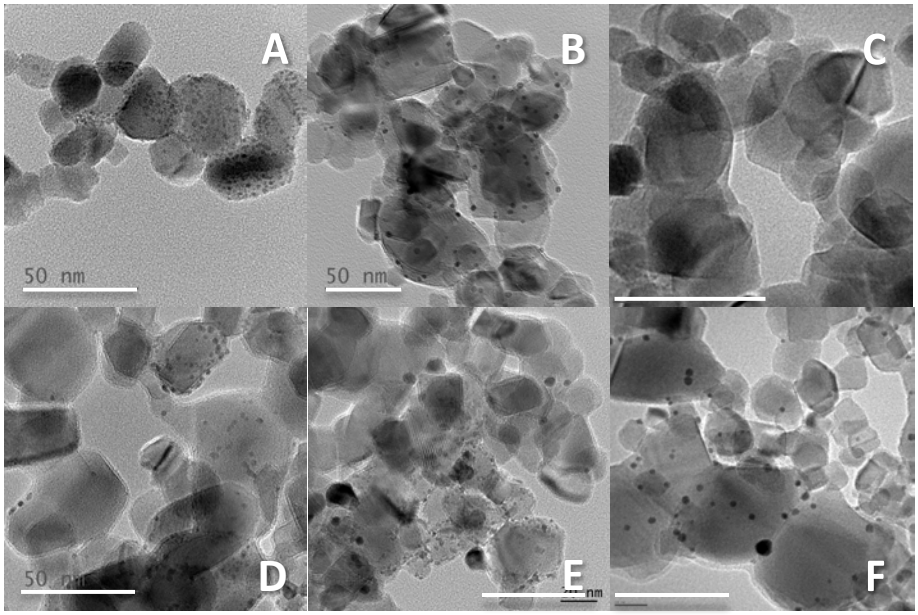

Figure 3.11. TEM image (A) Pd@TiO_2, (B) commercial Au@TiO_2, (C) Cu@TiO_2, (D) Cu@Pd@TiO_2; (E) Pd@Au@TiO_2, and (F) Cu@Au@TiO_2. Scale bars: 50 nm. Notice the gray 25-50 nm particles correspond to TiO_2 P25 and dark dots to metallic nanoparticles (MNP) deposited on the TiO_2 surface. Average MNP sizes are indicated in Table 3.10.

EDS analysis

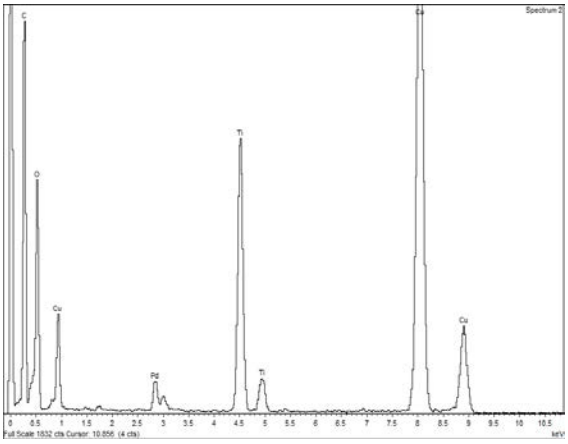

Figure 3.12**.** EDS spectrum for Pd@TiO_2 (Cu signals belong to the sample holder).

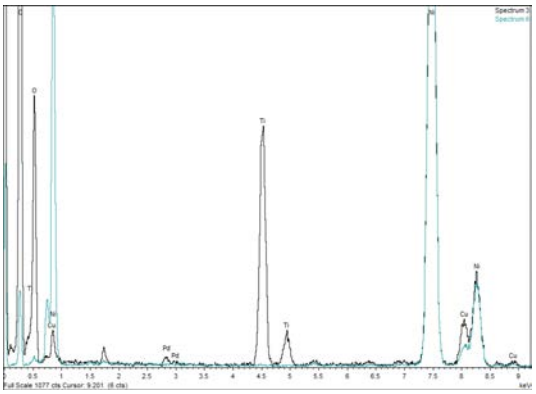

Figure 3.13**.** EDS spectrum for Cu@Pd@TiO_2. Notice that Ni signals belong to the sample holder and they interfere with the Cu signals. Cu presence was later confirmed by ICP-OES (See below).

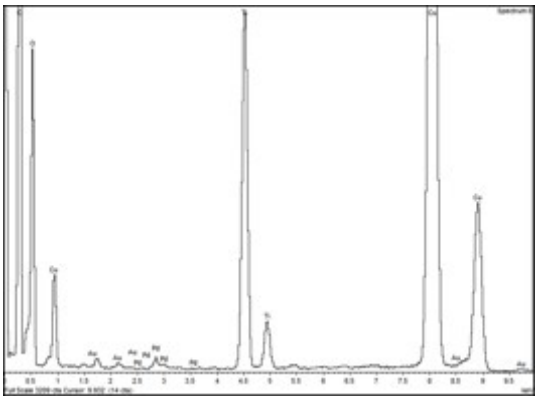

Figure 3.14. EDS spectrum for Pd@Au@TiO_2 (Cu signals belong to the sample holder).

XPS analysis

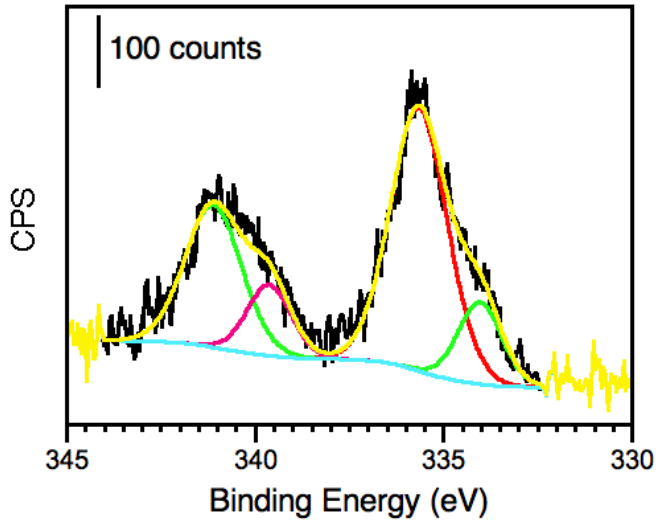

Figure 3.15. Deconvoluted Pd 3d HR-XPS spectra for Pd@TiO_2 catalyst. The curve fitting of the Pd 3d core-level spectrum is performed by using two spin-orbit split Pd $3d_{5/2}$ and Pd $3d_{3/2}$ components, separated by ~5.2 eV.

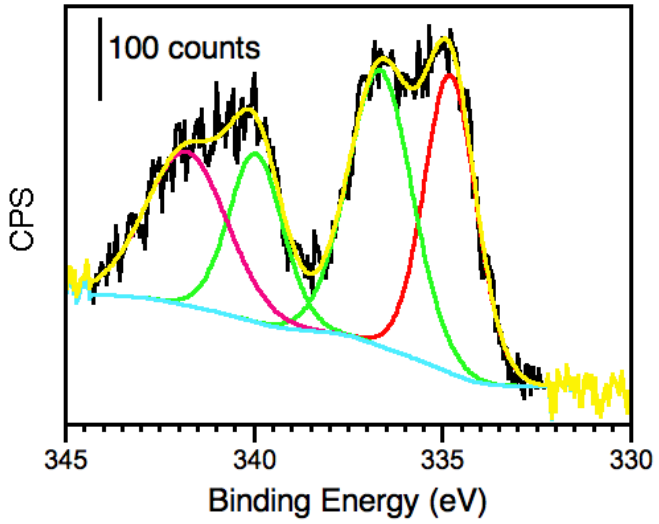

Figure 3.16. Deconvoluted Pd 3d HR-XPS spectra for Pd@Au@TiO_2 catalyst. The curve fitting of the Pd 3d core-level spectrum is performed by using two spin-orbit split Pd $3d_{5/2}$ and Pd $3d_{3/2}$ components, separated by ~5.2 eV.

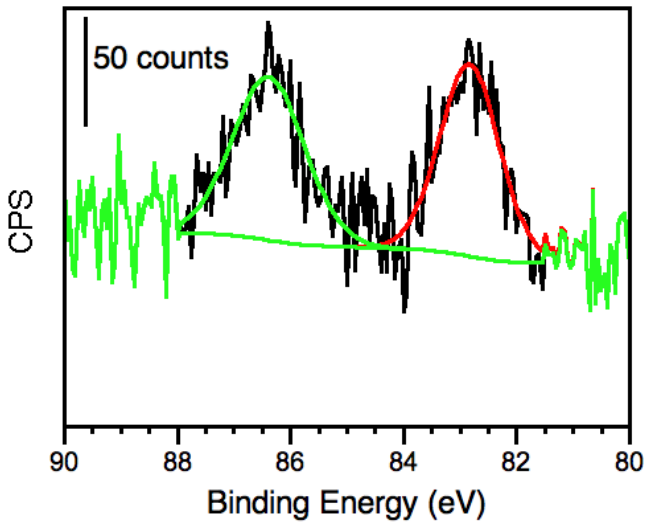

Figure 3.17. Deconvoluted Au 4f HR-XPS spectrum for Pd@Au@TiO_2 catalyst. The curve fitting of the Au 4f core-level spectrum is performed by using two spin-orbit split Au $4f_{7/2}$ and Au $4f_{5/2}$ components, separated by ~4.5 eV

DR spectra

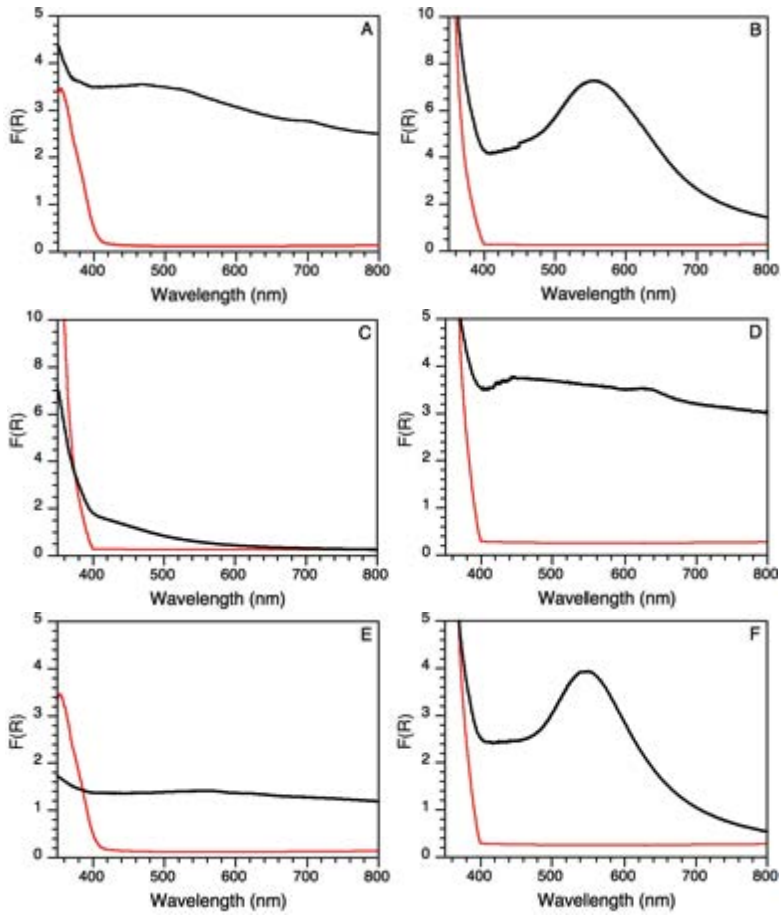

Figure 3.18. Diffuse reflectance spectra of TiO_2 in red and in black (A) Pd@TiO_2, (B) commercial Au@TiO_2, (C) Cu@TiO_2, (D) Cu@Pd@TiO_2; (E) Pd@Au@TiO_2, and (F) Cu@Au@TiO_2.

Metal loading analysis

Table 3.10. Main characterization features of the catalysts used in this work

	M_i-M_{ii}@TiO_2		Metal amount (wt%) [a]		Particle size (nm)	
	M_i	M_{ii}	M_i	M_{ii}	M_i	M_{ii}
i	Au	--	1.02	--	2.3 ± 0.9	--
ii	Cu	--	0.15	--	ND	--
iii	Pd	--	1.28	--	1.6 ± 0.9	--
iv	Pd	Au	1.66	1.03	0.94 ± 0.4	4.6 ± 1.5
v	Cu	Pd	0.13	0.94	ND	4.6 ± 0.9
vi	Cu	Au	0.17	1.03	ND	3.6 ± 1.5

[a] Determined by ICP-OES.

3.5 Conclusion

In conclusion, we have demonstrated how two-color irradiation of Pd@TiO_2 photocatalyst can tune the selectivity of the Ullmann reaction toward the cross coupling product by using the corresponding aryl iodide derivative. The reaction proceeds under mild conditions and with excellent yields. It was proven that the system is heterogeneous and reusable. We believe that using different wavelengths of light open the road to many organic synthesis.

We believe that the light should be thought of as a reagent that needs to be considered and optimized in a chemical reaction in order to selectively favor one product over the other. For instance, using two lights for Ullmann coupling allowed us to achieve high selectivity toward the cross coupling whereas a monochromatic light failed to do so.

3.6 Future Work

Future work will focus on finding the optimal conditions that allow us to expand the scope of the reaction to include both aryl bromides and aryl chlorides. Moreover, the field of using different wavelengths of lights can be applied in order to tune the selectivity for different organic reactions such as cross coupling between two vinyl halides or vinyl halides and aryl halides.

3.7 Appendix

Reaction scope and product characterization

1. **Methyl 4'-methoxy-[1,1'-biphenyl]-4-carboxylate.**

^{1}H NMR (400 MHz, $CDCl_3$): δ 8.1 (dt, 2 H), 7.6 (m, 4H), 7.0 (dt, 2 H), 3.9 (s, 3H), 3.8 (s, 3H); ^{13}C NMR (100 MHz, $CDCl_3$): δ 167.1 (C14), 159.9 (C3), 145.2 (C8), 132.4 (C6), 130.2-130.1 (C11), 129.7(C10, C12), 128.4-128.3 (C5, C7), 126.5 (C9, C13), 114.4-114.2 (C2, C4), 55.4 (C17), 52.1 (C1) .

MS calculated for $C_{15}H_{14}O_3$: 242.09

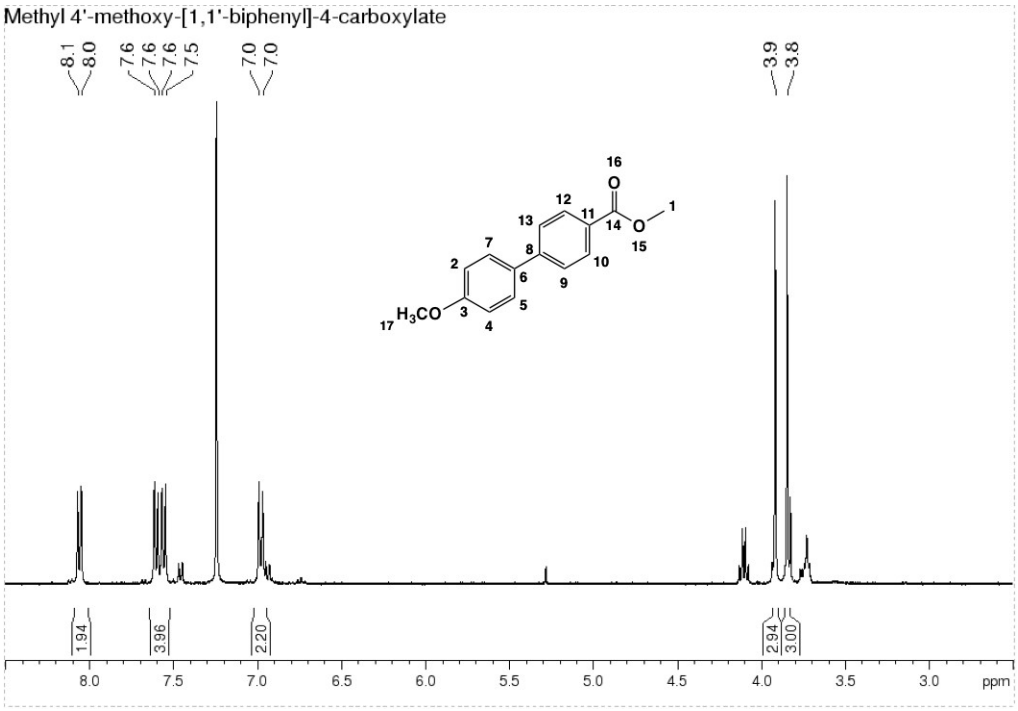

Figure 3.19. ^{1}H NMR of Methyl 4'-methoxy-[1,1'-biphenyl]-4-carboxylate.

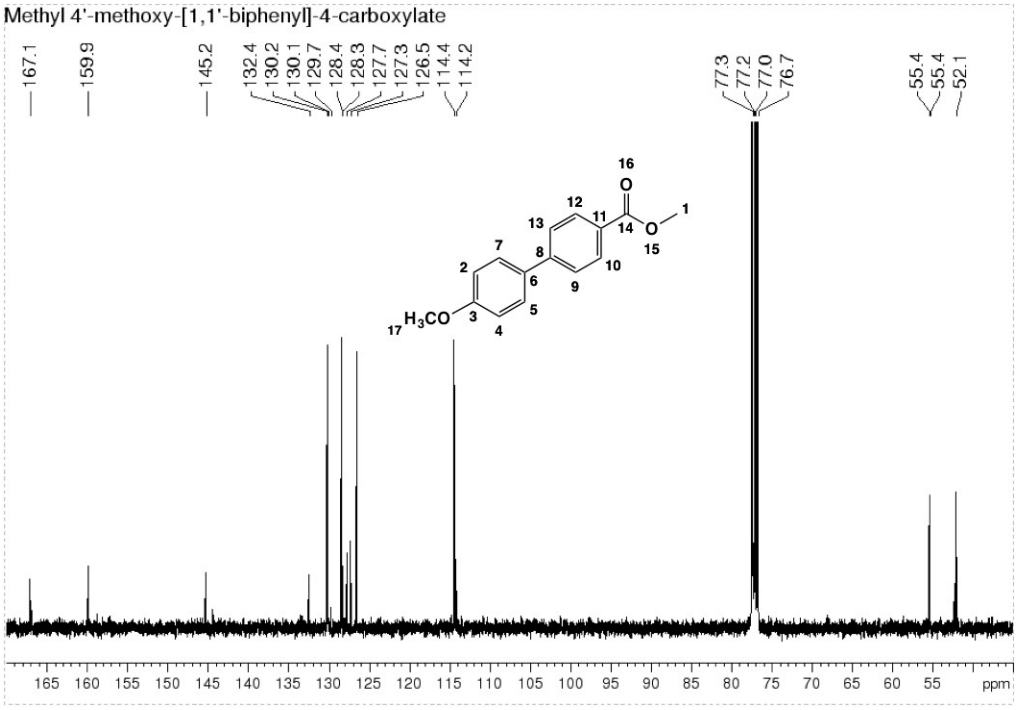

Figure 3.20. ^{13}C NMR of Methyl 4'-methoxy-[1,1'-biphenyl]-4-carboxylate.

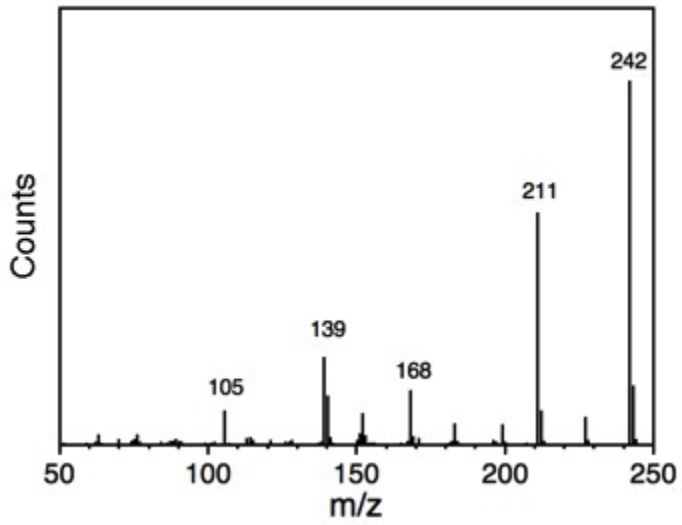

Figure 3.21. MS spectrum of Methyl 4'-methoxy-[1,1'-biphenyl]-4-carboxylate

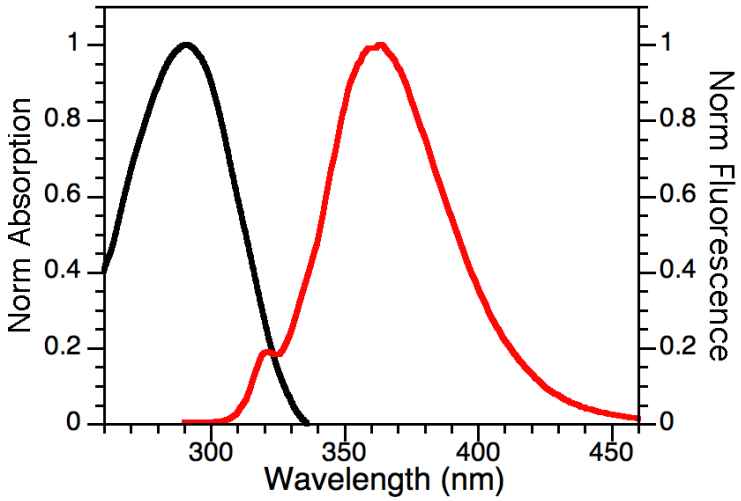

Figure 3.22. UV-Vis (black) and fluorescence (red) spectra (λ_{exc} 278 nm) of Methyl 4'- methoxy-[1,1'-biphenyl]-4-carboxylate

2. **Methyl 4'-amino-[1,1'-biphenyl]-4-carboxylate**.

MS calculated for $C_{14}H_{13}NH_2$: 227.26

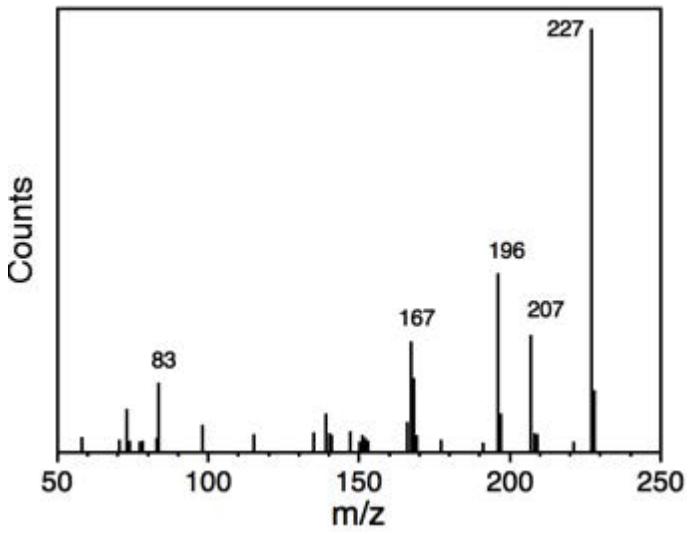

Figure 3.23. MS spectrum of Methyl 4'-amino-[1,1'-biphenyl]-4-carboxylate

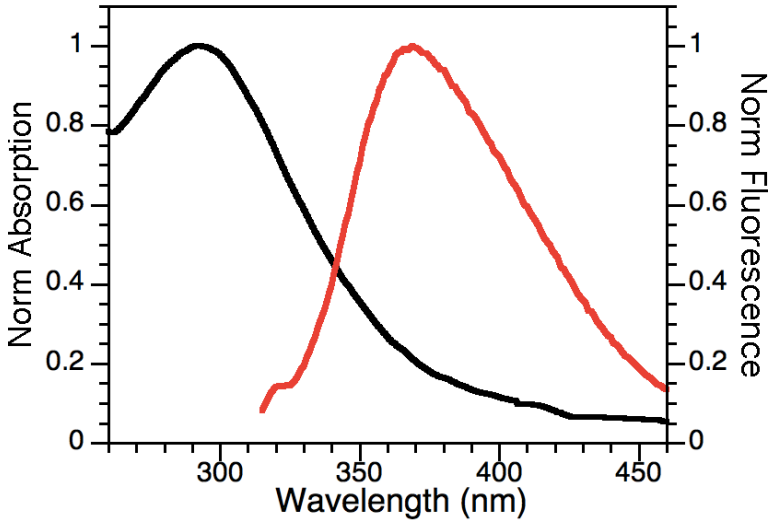

Figure 3.24. UV-Vis and fluorescence spectra (λ_{exc} 275 nm) of Methyl 4'-amino-[1,1'-biphenyl]-4-carboxylate (non-isolated).

3. **Methyl [1,1'-biphenyl]-4-carboxylate**.

^{1}H NMR (400 MHz, $CDCl_3$): δ 8.1 (dt, 2 H), 7.6 (m, 4H), 7.5-7.4 (m, 3 H), 3.9 (s, 3H); ^{13}C NMR (100 MHz, $CDCl_3$): δ 167.0 (C14), 145.7 (C8), 140.0 (C6), 130.1(C3-11), 128.9 (C2-4), 128.2 (C5-7), 127.3(C10-12), 127.1 (C9-13), 52.1 (C1).

MS calculated for $C_{14}H_{12}O_2$: 212.25

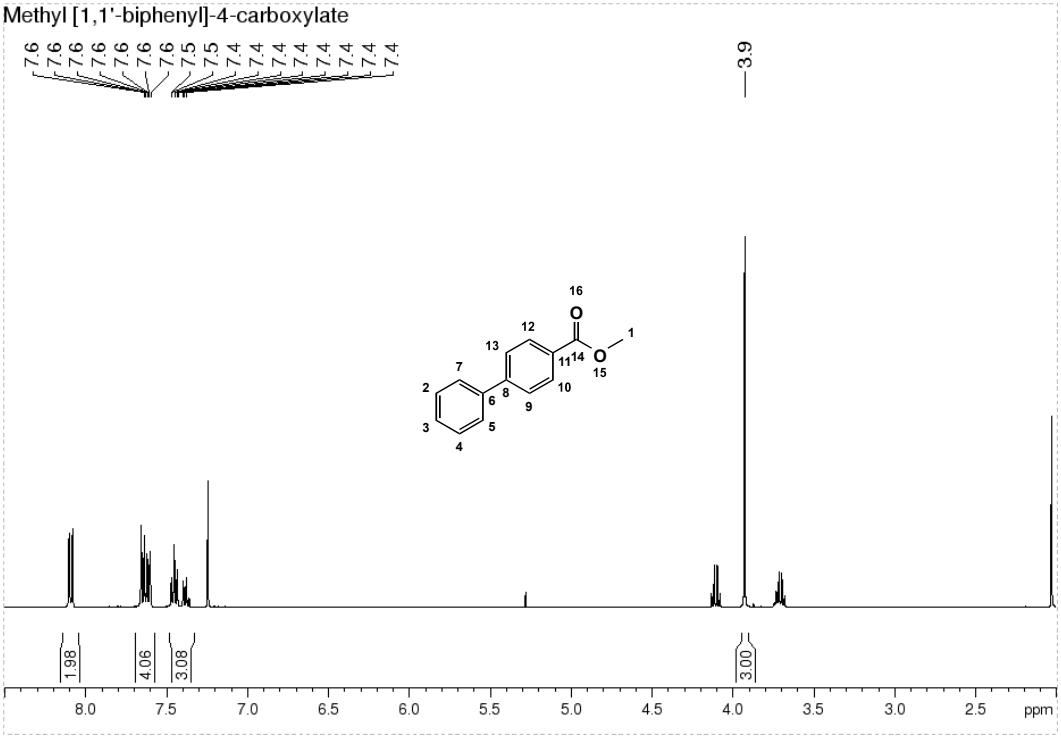

Figure 3.25. ^{1}H NMR of Methyl [1,1'-biphenyl]-4-carboxylate.

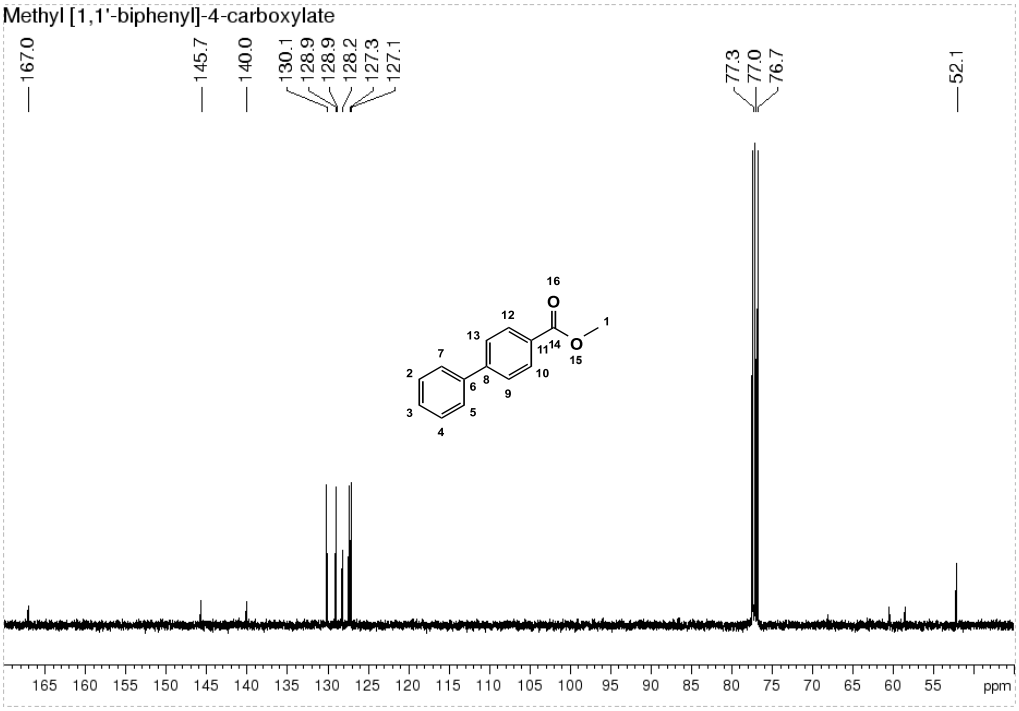

Figure 3.26. ^{13}C NMR of Methyl [1,1'-biphenyl]-4-carboxylate.

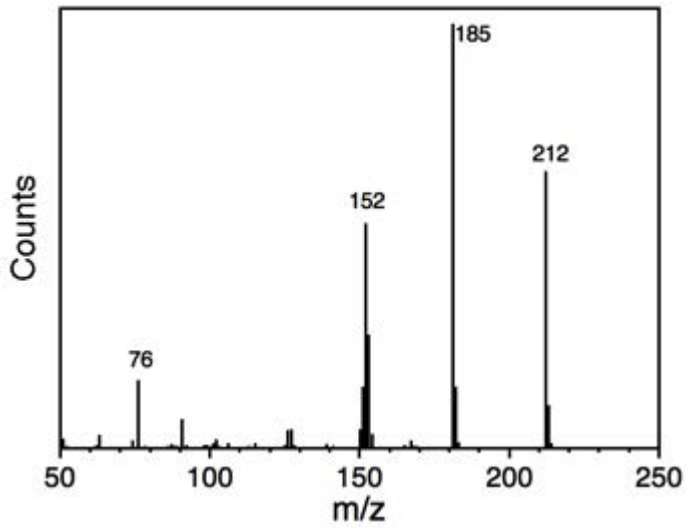

Figure 3.27. MS spectrum of Methyl [1,1'-biphenyl]-4-carboxylate

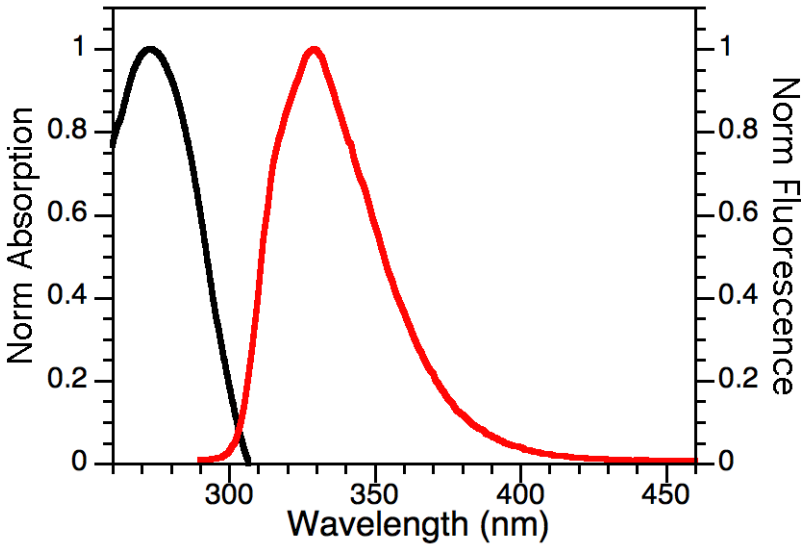

Figure 3.28. UV-Vis and fluorescence spectra (λ_{exc} 275 nm) of Methyl [1,1'-biphenyl]-4- carboxylate

4. **Methyl 3'-methyl-[1,1'-biphenyl]-4-carboxylate.**

^{1}H NMR (400 MHz, $CDCl_3$): δ 8.1 (dt, 2 H), 7.6 (dt, 2H), 7.4 (m, 2 H), 7.3 (td, 1H), 7.2 (m, 1H); ^{13}C NMR (100 MHz, $CDCl_3$): δ 167.1 (C14), 145.8 (C8), 140.0 (C6), 138.6(C2), 130.1(C11), 128.9 (C3), 128.8 (C10-12), 128.1(C4), 127.7 (C7), 127.1 (C5), 124.4 (C9-13), 52.1 (C1), 21.5 (C17).

MS calculated for $C_{15}H_{14}O_2$: 226.28

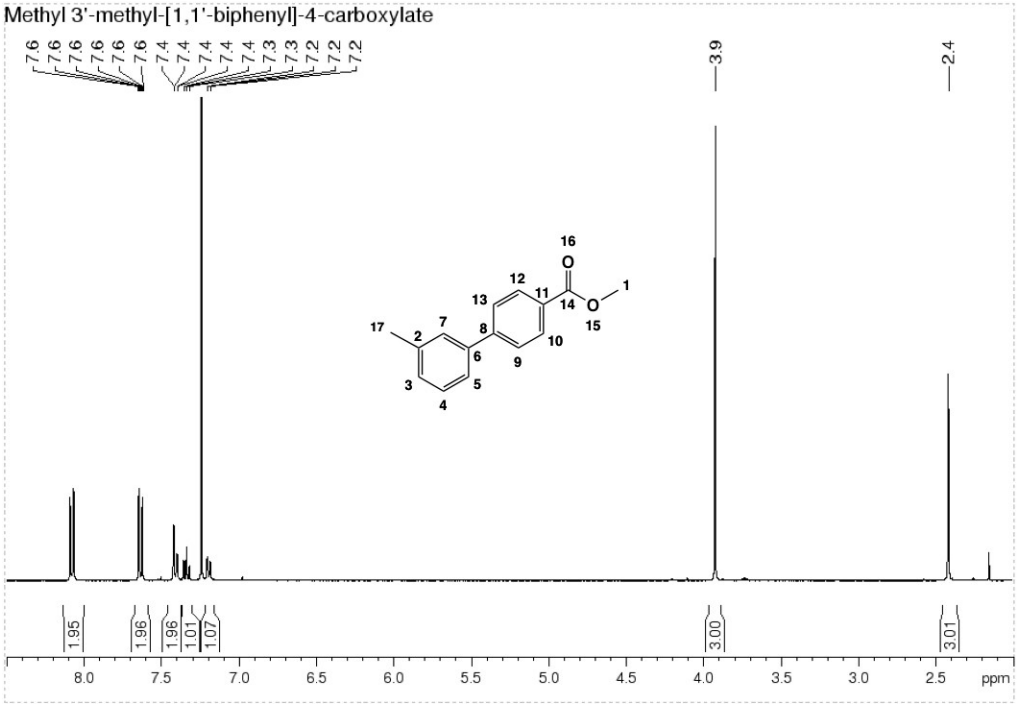

Figure 3.29. ^{1}H NMR of Methyl 3'-methyl-[1,1'-biphenyl]-4-carboxylate.

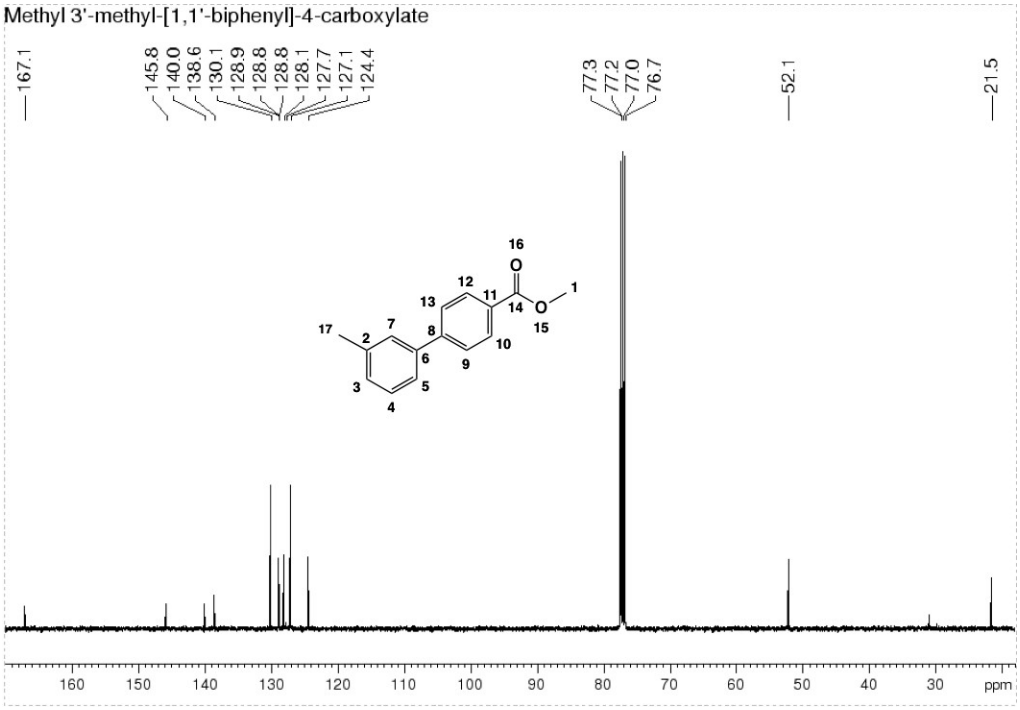

Figure 3.30. ^{13}C NMR of Methyl 3'-methyl-[1,1'-biphenyl]-4-carboxylate.

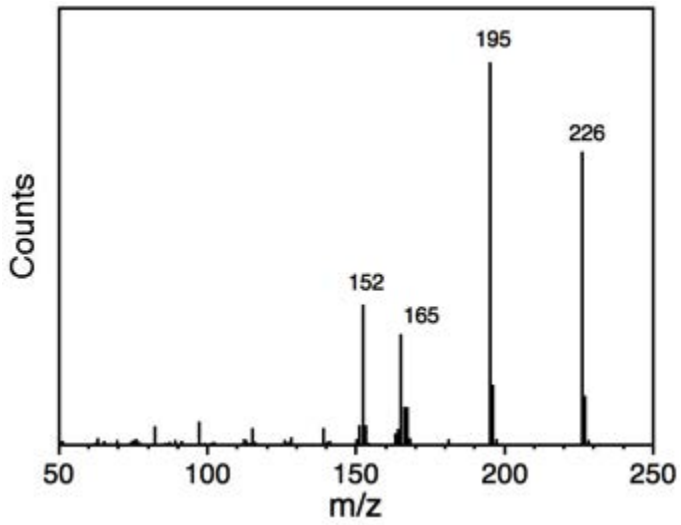

Figure 3.31. MS spectrum of Methyl 3'-methyl-[1,1'-biphenyl]-4-carboxylate

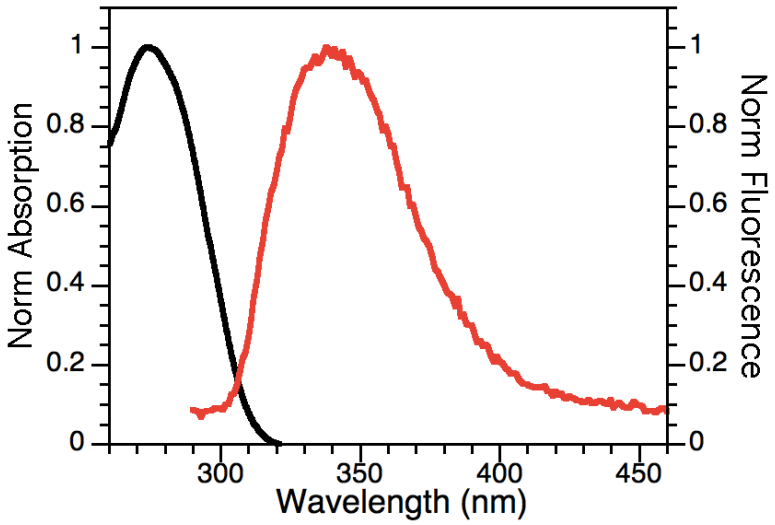

Figure 3.32. UV-Vis and fluorescence spectra (λ_{exc} 275 nm) of Methyl 3'-methyl-[1,1'- biphenyl]-4-carboxylate

5. **Methyl 4'-cyano-[1,1'-biphenyl]-4-carboxylate.**

^{1}H NMR (400 MHz, $CDCl_3$): δ 8.1 (dt, 2 H), 7.7 (m, 4H), 7.6 (dt, 2 H), 3.9 (s, 3H); ^{13}C NMR (100 MHz, $CDCl_3$): δ 166.6 (C14), 144.5 (C8), 143.4 (C6), 132.7 (C2-4), 130.4 (C10-12), 130.2 (C11), 128.0 (C5-7), 127.3 (C9-13), 118.7 (q, C17), 111.9 (C3), 52.2 (C1).

MS calculated for $C_{15}H_{11}NO_2$: 237.26

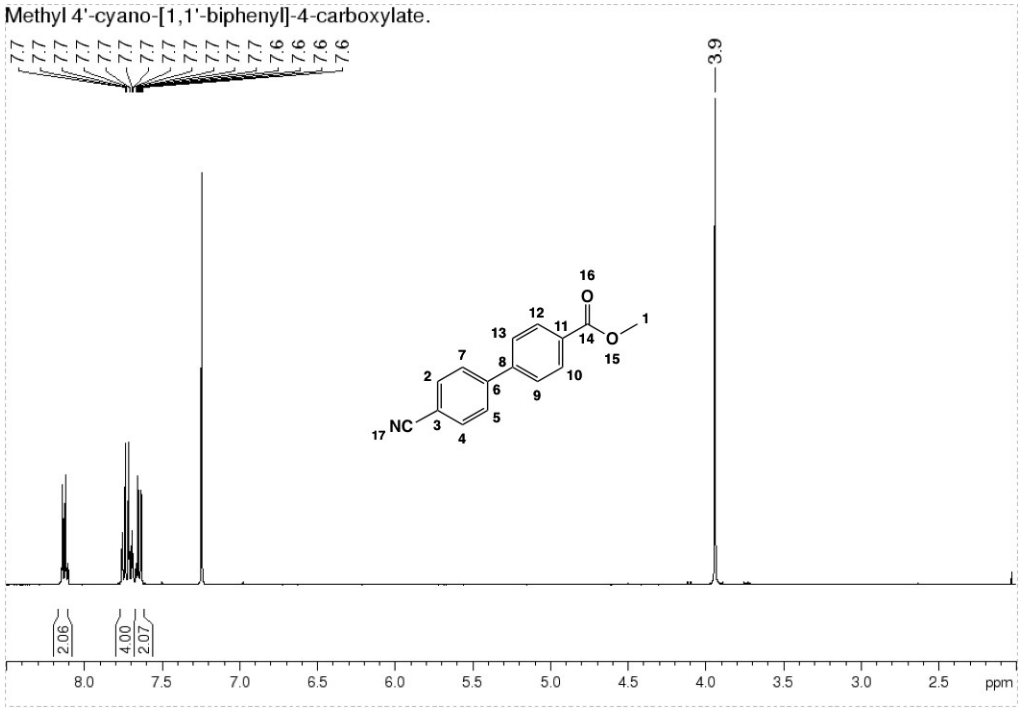

Figure 3.33. ^{1}H NMR of Methyl 4'-cyano-[1,1'-biphenyl]-4-carboxylate

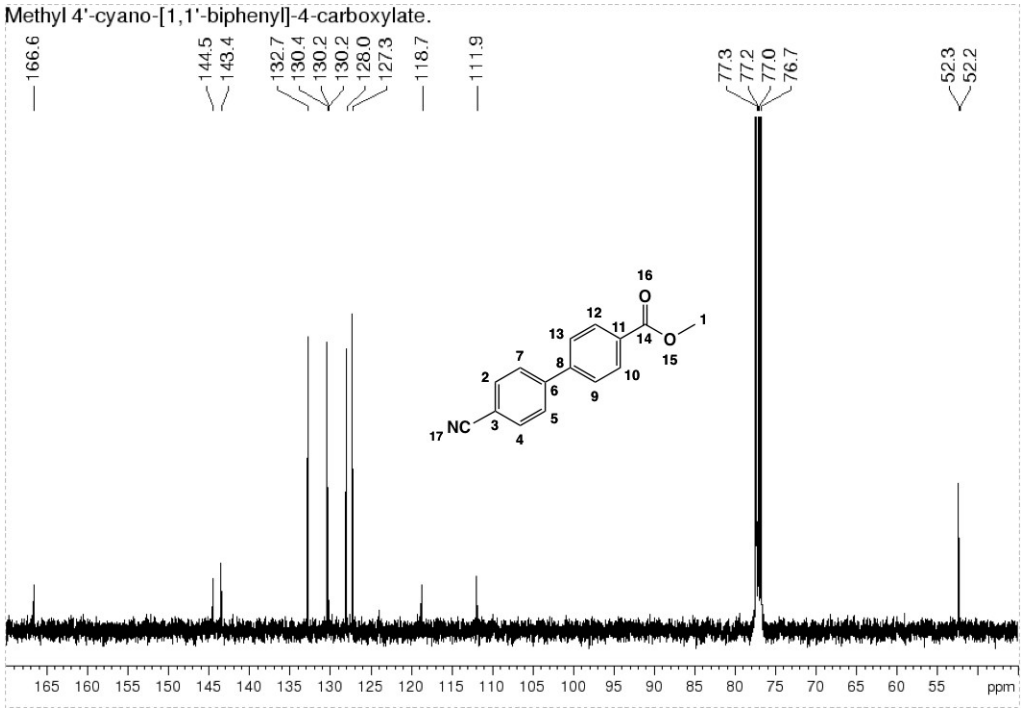

Figure 3.34. ^{13}C NMR of Methyl 4'-cyano-[1,1'-biphenyl]-4-carboxylate

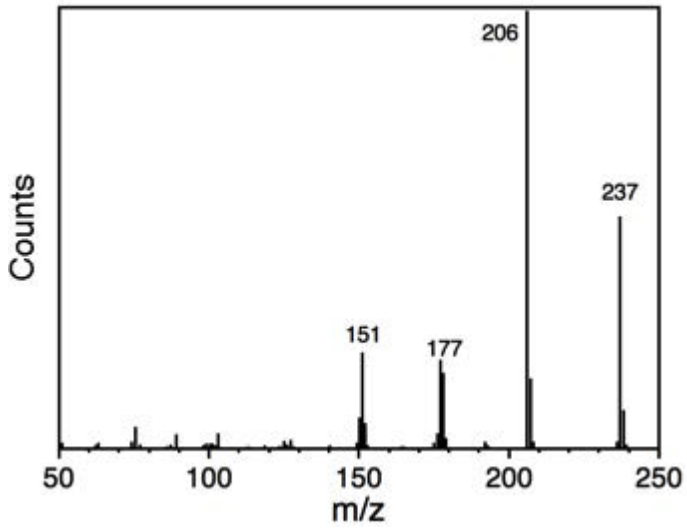

Figure 3.35. MS spectrum of Methyl 4'-cyano-[1,1'-biphenyl]-4-carboxylate.

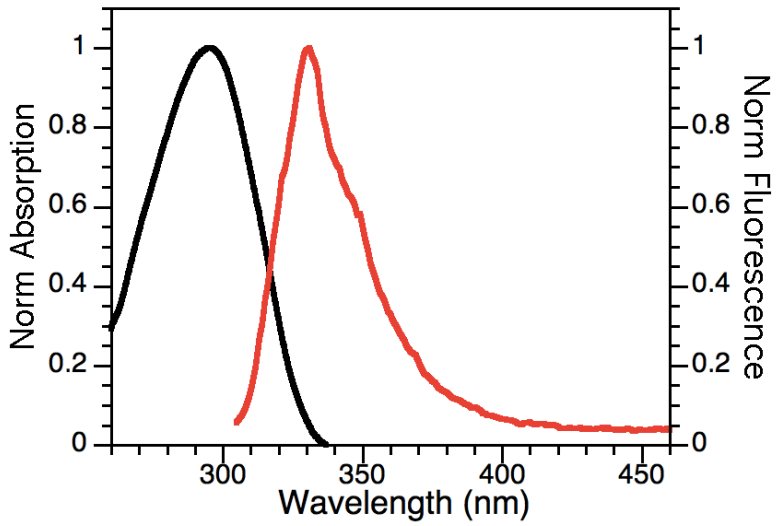

Figure 3.36. UV-Vis and fluorescence spectra (λ_{exc} 290 nm) of Methyl 4'-cyano-[1,1'-biphenyl]-4-carboxylate.

6. **Methyl 4'-(trifluoromethyl)-[1,1'-biphenyl]-4-carboxylate**.

^{1}H NMR (400 MHz, $CDCl_3$): δ 8.1 (dt, 2 H), 7.7 (s, 4H), 7.6 (dt, 2 H), 3.9 (s, 3H); ^{13}C NMR (100 MHz, $CDCl_3$): δ 166.8 (C14), 144.1 (C8), 143.5 (C6), 130.3(C3-11), 129.8 (C10-12), 127.6 (C5-7), 127.3 (C9-13), 125.9 (C2-4), 125.8 (q, C17), 52.2 (C1).

MS calculated for $C_{15}H_{11}F_3O_2$: 280.25

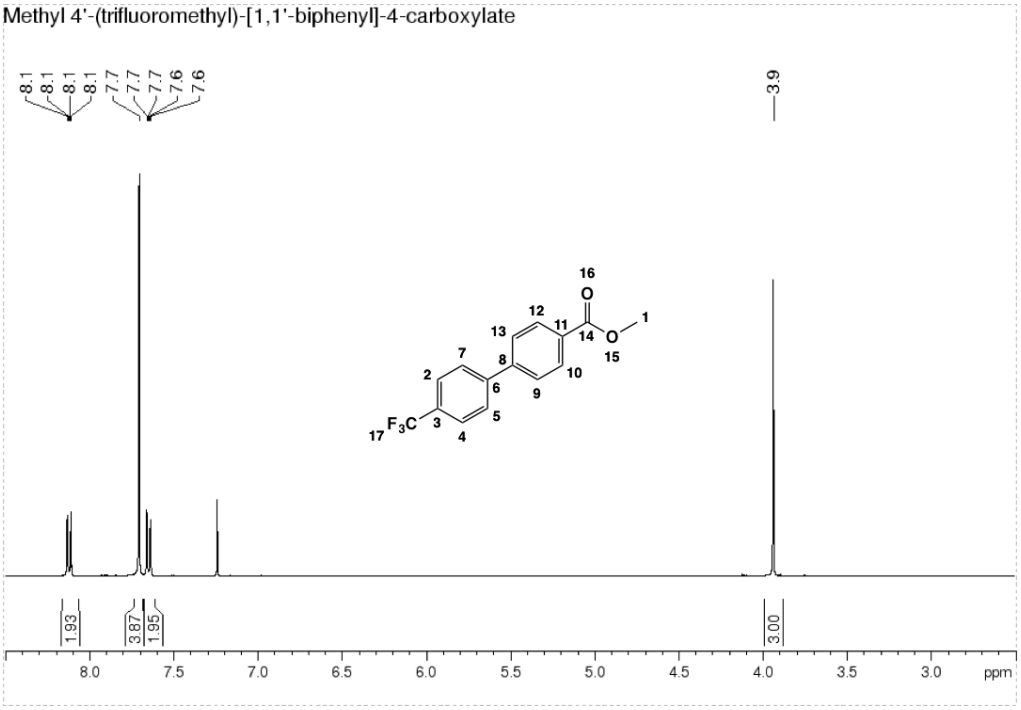

Figure 3.37. ^{1}H NMR of Methyl 4'-(trifluoromethyl)-[1,1'-biphenyl]-4-carboxylate

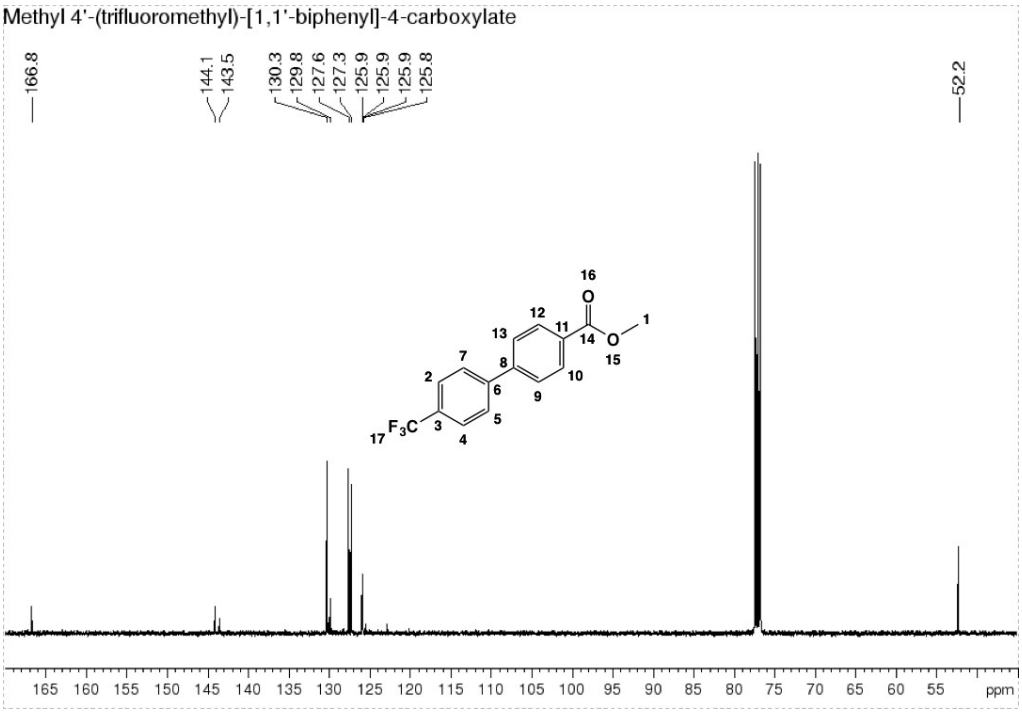

Figure 3.38. ^{13}C NMR of Methyl 4'-(trifluoromethyl)-[1,1'-biphenyl]-4-carboxylate

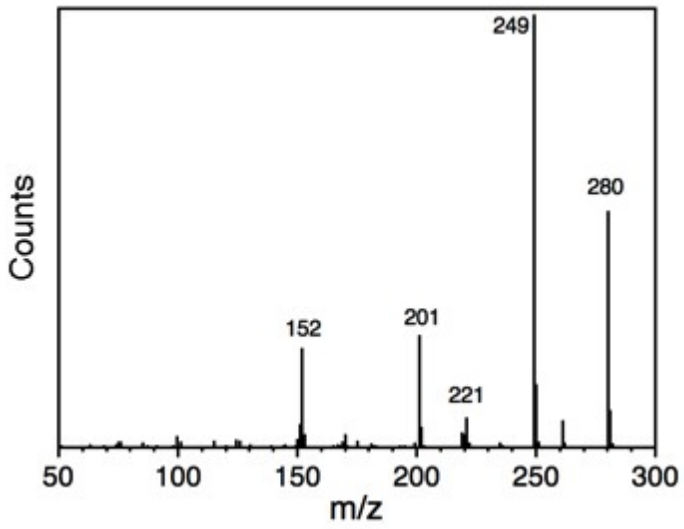

Figure 3.39. MS spectrum of Methyl 4'-(trifluoromethyl)-[1,1'-biphenyl]-4-carboxylate

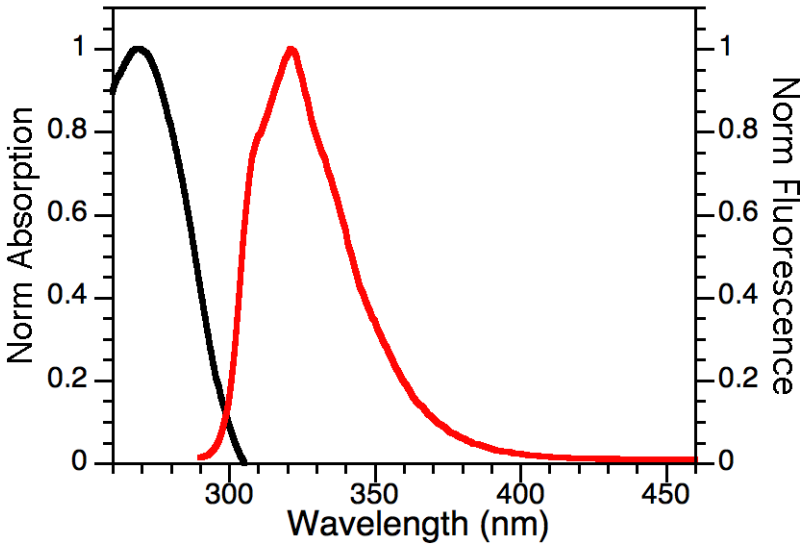

Figure 3.40. UV-Vis and fluorescence spectra (λ_{exc} 278 nm) of Methyl 4'-(trifluoromethyl)-[1,1'-biphenyl]-4-carboxylate

7. **4'-methoxy-[1,1'-biphenyl]-4-carbonitrile**.

^{1}H NMR (400 MHz, $CDCl_3$): δ 7.7-7.6 (m, 4H), 7.5 (dt, 2 H), 7.0 (dt, 2H), 3.8 (s, 3H); ^{13}C NMR (100 MHz, $CDCl_3$): δ 160.2 (C3), 145.3 (C8), 132.6 (C10-12), 131.5 (C6) 128.4 (C5-7), 127.1 (C9-13), 119.1 (C14), 114.6 (C2-4), 110.1 (C11), 55.4 (C15).

MS calculated for $C_{14}H_{11}NO$: 209.08

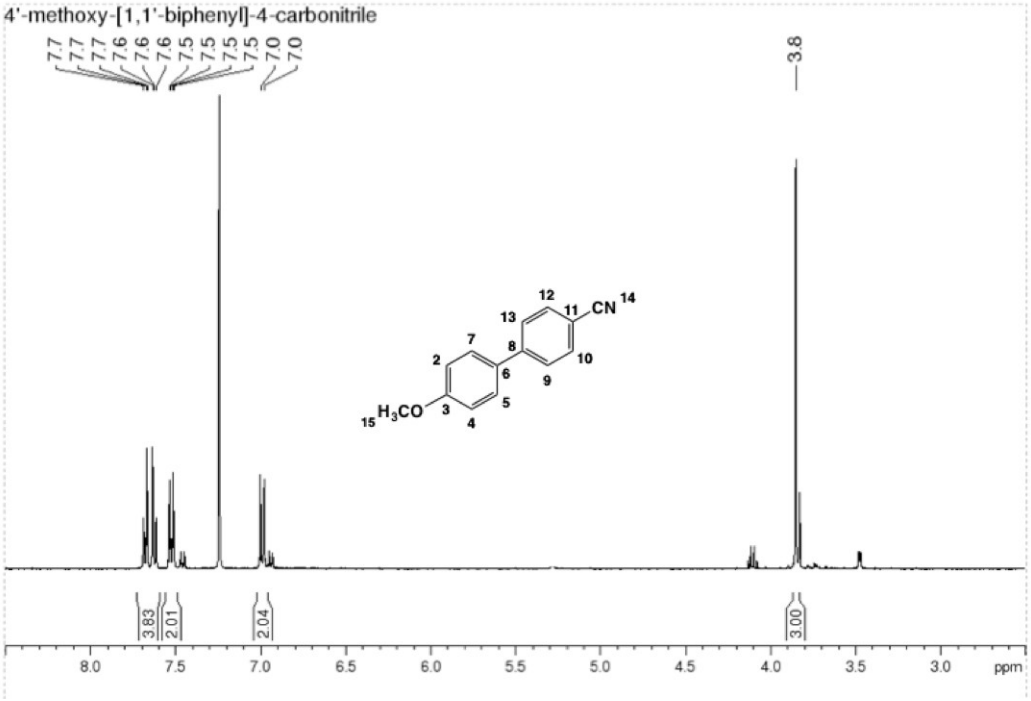

Figure 3.41. ^{1}H NMR of 4'-methoxy-[1,1'-biphenyl]-4-carbonitrile.

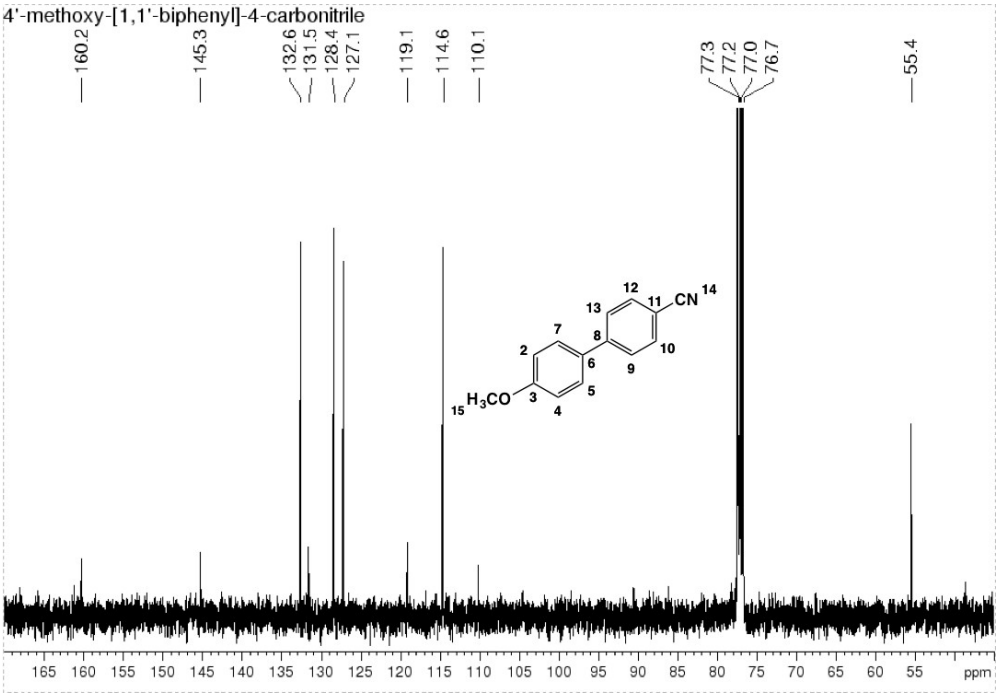

Figure 3.42. ^{13}C NMR of 4'-methoxy-[1,1'-biphenyl]-4-carbonitrile

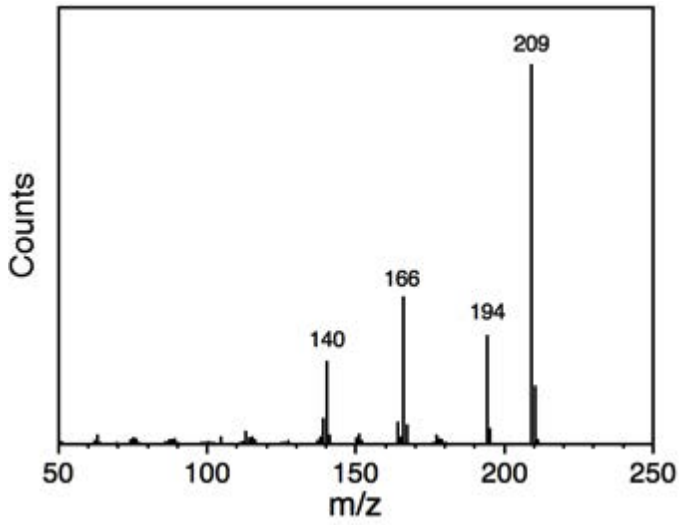

Figure 3.43. MS spectrum of 4'-methoxy-[1,1'-biphenyl]-4-carbonitrile

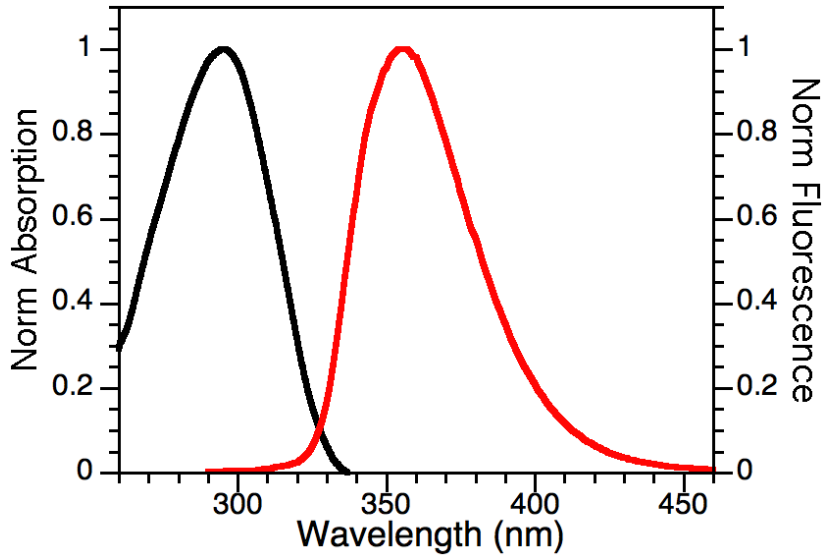

Figure 3.44. UV-Vis and fluorescence spectra (λ_{exc} 295 nm) of 4'-methoxy-[1,1'-biphenyl]-4-carbonitrile

8. **4-methoxy-4'-(trifluoromethyl)-1,1'-biphenyl.**

^{1}H NMR (400 MHz, $CDCl_3$): δ 7.6 (m, 4H), 7.5 (dt, 2 H), 7.0 (dt, 2 H), 3.8 (s, 3H); ^{13}C NMR (100 MHz, $CDCl_3$): δ 159.9 (C3), 144.3 (C8), 132.2 (C6-11), 128.4 (C5-7), 126.9 (C9-10-12-13), 125.7 (q, C14), 114.4 (C2-4), 55.4 (C15).

MS calculated for $C_{14}H_{11}F_3O$: 252.08

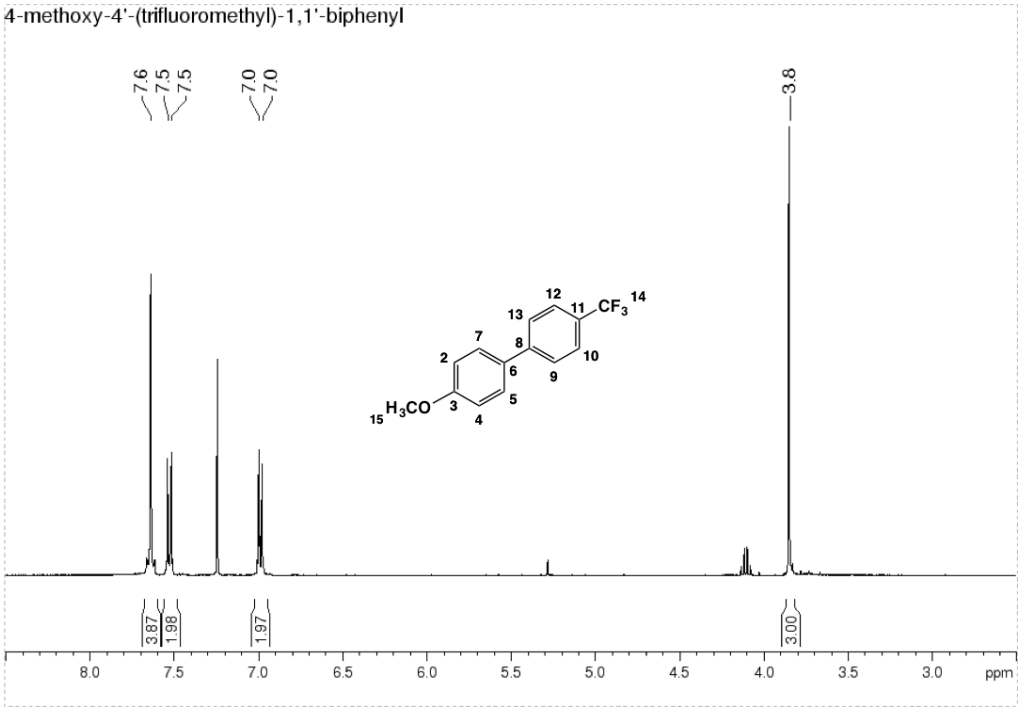

Figure 3.45. ^{1}H NMR of 4-methoxy-4'-(trifluoromethyl)-1,1'-biphenyl.

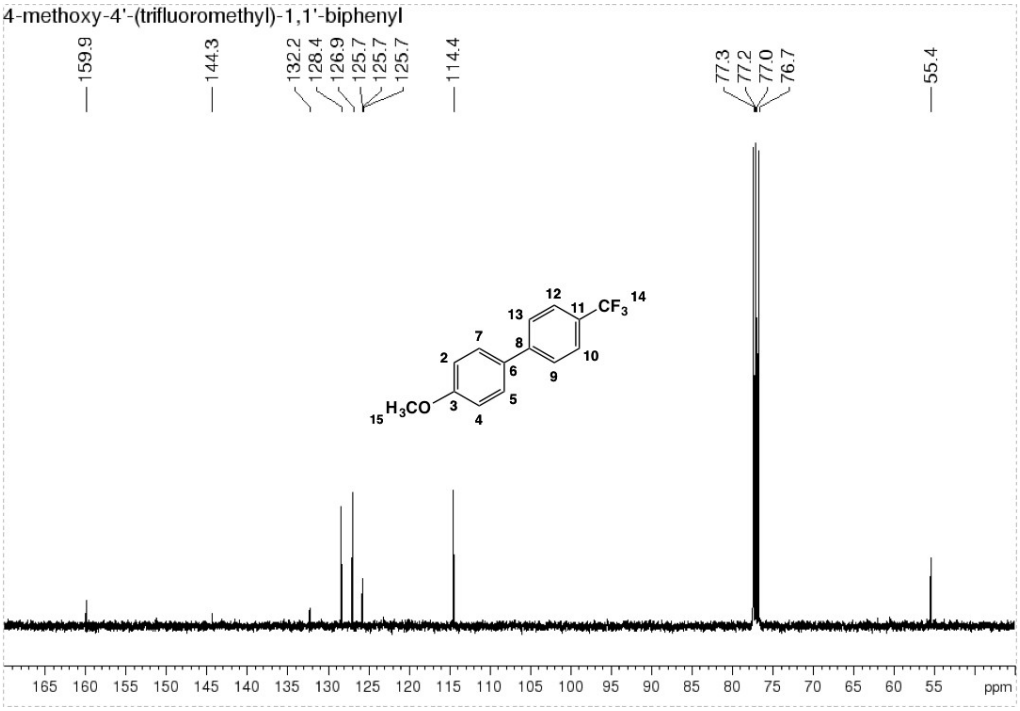

Figure 3.46. ^{13}C NMR of 4-methoxy-4'-(trifluoromethyl)-1,1'-biphenyl.

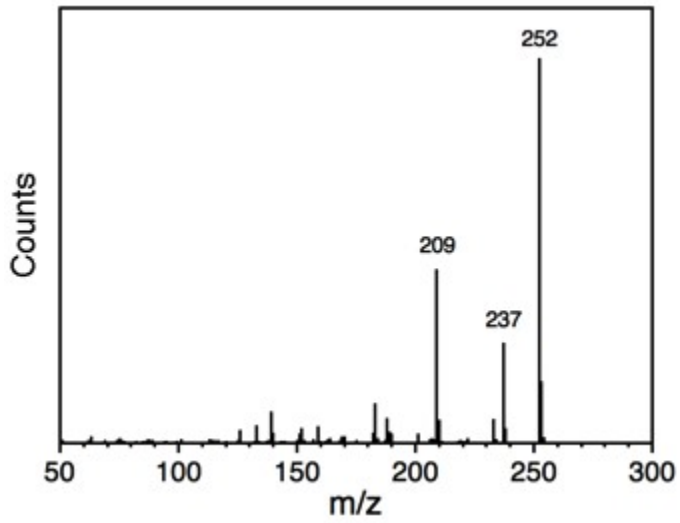

Figure 3.47. MS spectrum of 4-methoxy-4'-(trifluoromethyl)-1,1'-biphenyl

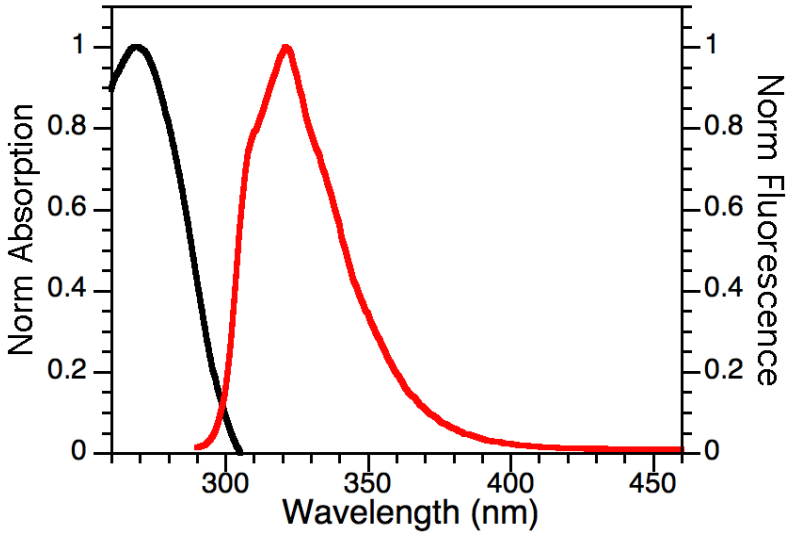

Figure 3.48. UV-Vis and fluorescence spectra (λ_{exc} 278 nm) of 4-methoxy-4'-(trifluoromethyl)-1,1'-biphenyl

9. **[1,1'-Biphenyl]-4,4'-dicarbonitrile.**

^{1}H NMR (400 MHz, $CDCl_3$): δ 7.8 (m, 4H), 7.7 (m, 4 H); ^{13}C NMR (100 MHz, $CDCl_3$): δ 143.6 (C6-8), 132.9 (C2-4-10-12), 128.0 (C5-7-9-13), 118.4 (C14-17), 112.5 (C3-11).

MS calculated for $C_{14}H_8N_2$: 204.07

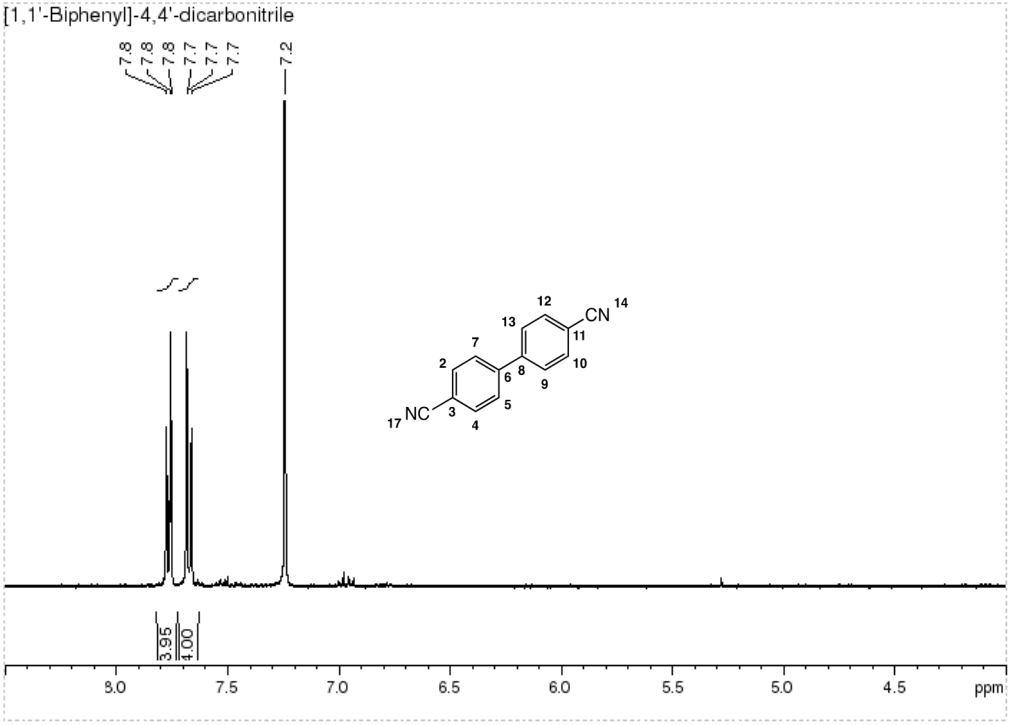

Figure 3.49. ^{1}H NMR of [1,1'-Biphenyl]-4,4'-dicarbonitrile.

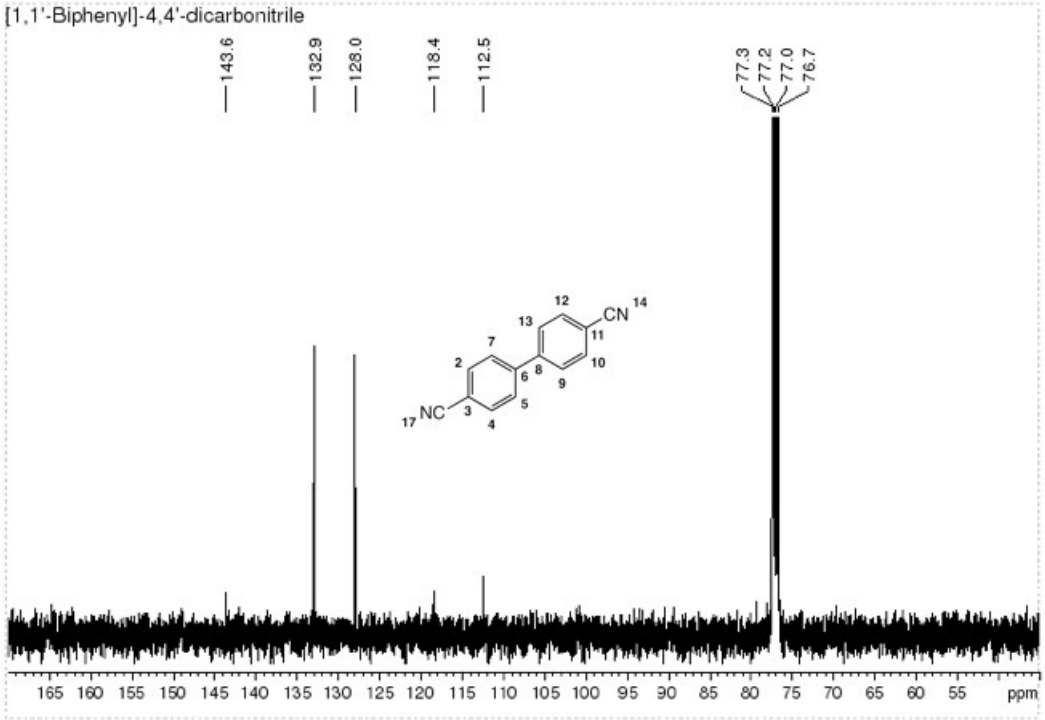

Figure 3.50. ^{13}C NMR of [1,1'-Biphenyl]-4,4'-dicarbonitrile.

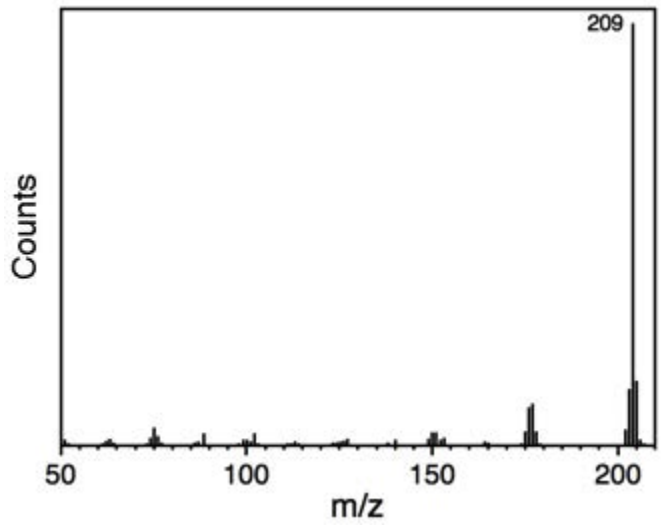

Figure 3.51.MS spectrum of [1,1'-Biphenyl]-4,4'-dicarbonitrile.

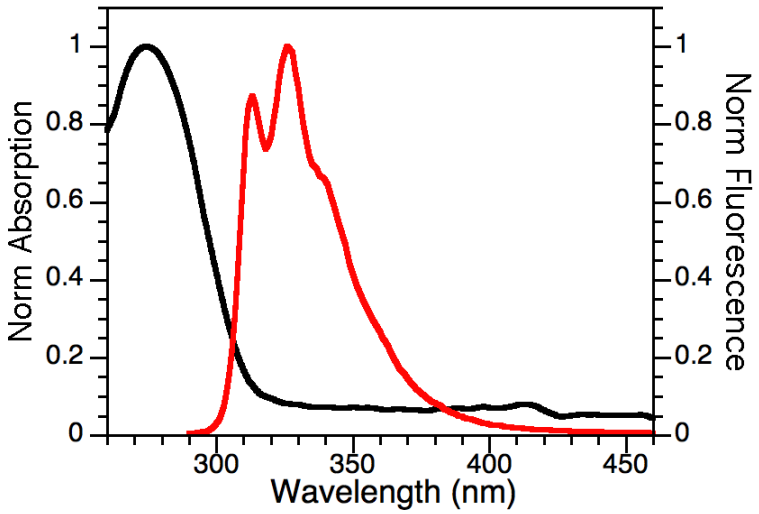

Figure 3.52. UV-Vis and fluorescence spectra (λ_{exc} 278 nm) of [1,1'-Biphenyl]-4,4'-dicarbonitrile.

10. 1,1'-Biphenyl, 4,4'-bis(trifluoromethyl).

^{1}H NMR (400 MHz, $CDCl_3$): δ 7.7 (m, 8H); ^{13}C NMR (100 MHz, $CDCl_3$): δ 143.3 (C6-8), 130.5-130.1 (C3-11), 127.6 (C5-7-9-13), 126.0-125.9 (C14-17), 125.5 (C2-4-10-12).

MS calculated for $C_{14}H_8F_6$: 290.05

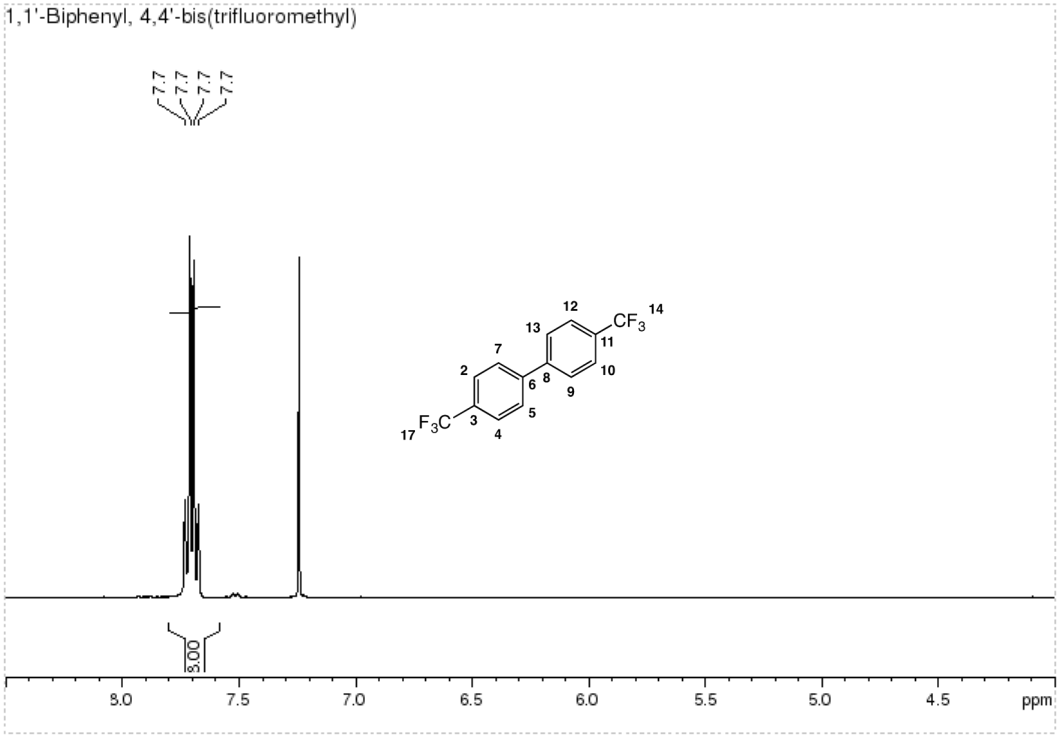

Figure 3.53. ^{1}H NMR of 1,1'-Biphenyl, 4,4'-bis(trifluoromethyl).

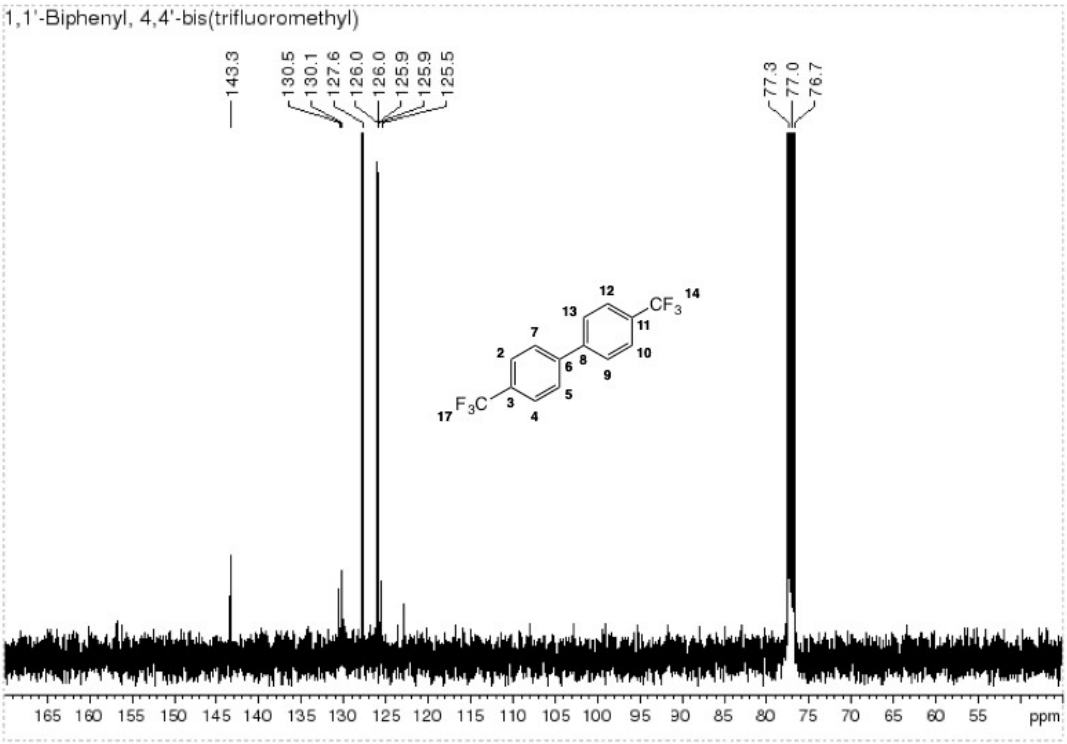

Figure 3.54. ^{13}C NMR of 1,1'-Biphenyl, 4,4'-bis(trifluoromethyl).

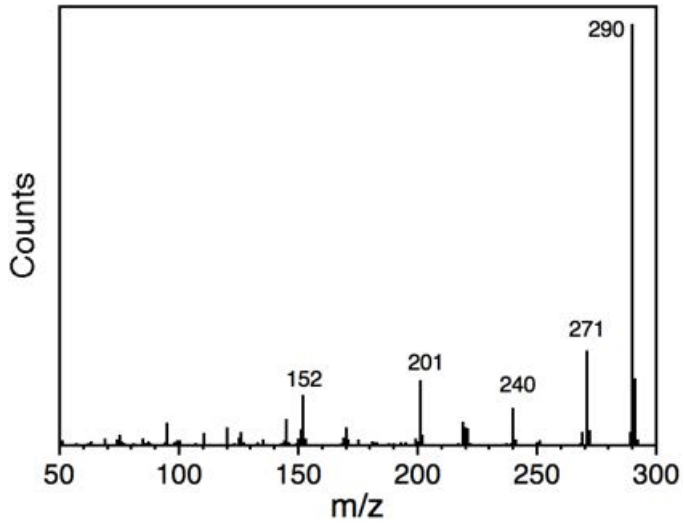

Figure 3.55. MS spectrum of 1,1'-Biphenyl, 4,4'-bis(trifluoromethyl).

11. Dimethyl [1,1'-biphenyl]-4,4'-dicarboxylate.

^{1}H NMR (400 MHz, $CDCl_3$): δ 8.1 (m, 4H), 7.7 (m, 4 H), 3.9 (s, 6 H); ^{13}C NMR (100 MHz, $CDCl_3$): δ 166.8 (C14-17), 144.4 (C6-8), 130.2 (C3-11), 129.7 (C2-4-10-12), 127.3 (C5-7-9-13), 52.2 (C20-23).

MS calculated for $C_{16}H_{14}O_4$: 270.09

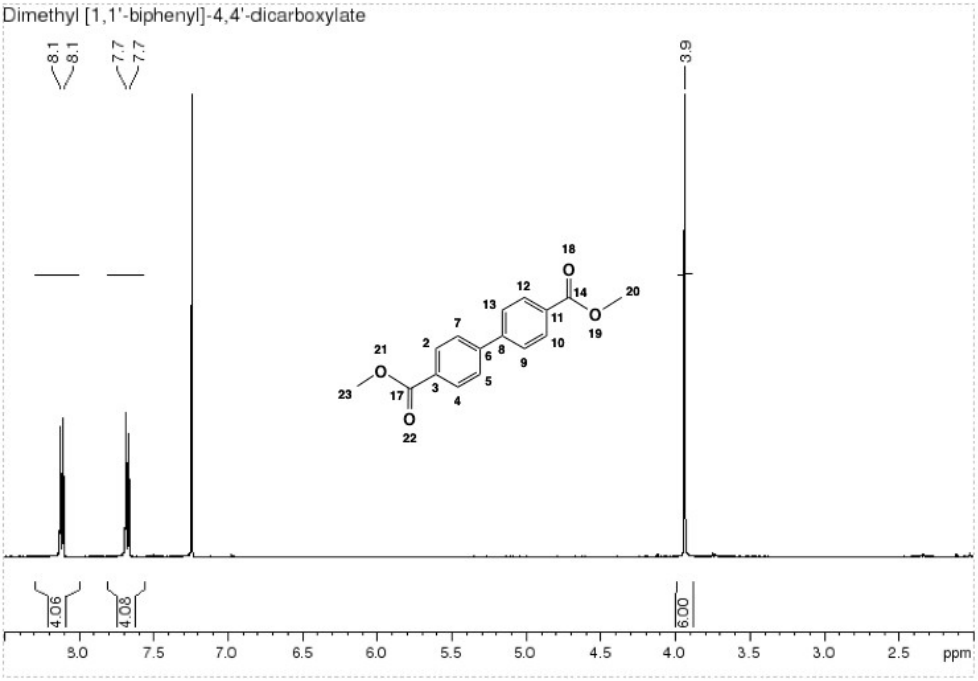

Figure 3.56. ^{1}H NMR of Dimethyl [1,1'-biphenyl]-4,4'-dicarboxylate

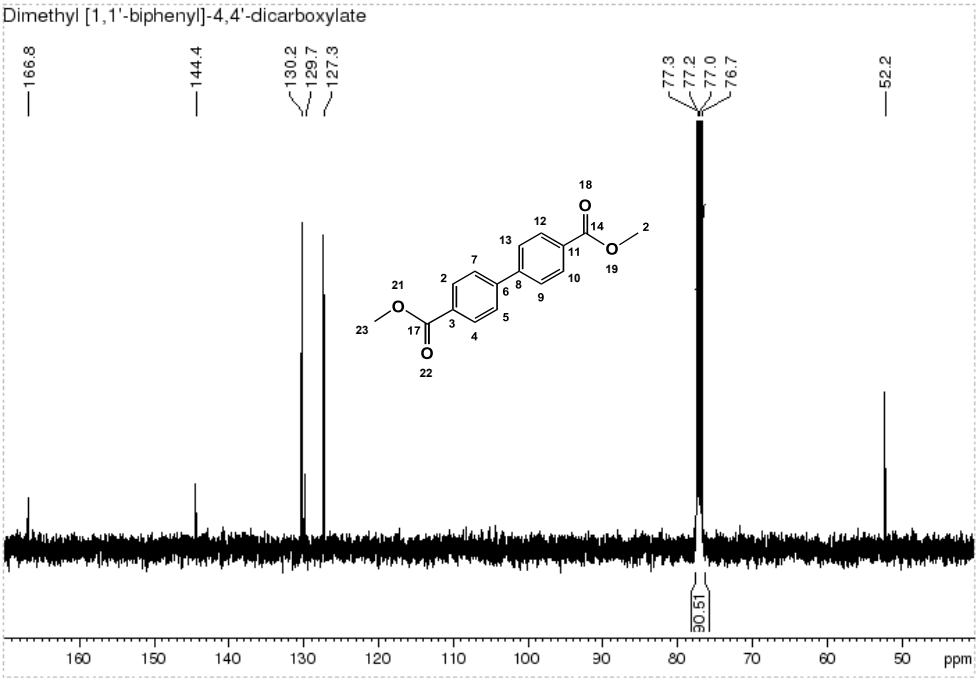

Figure 3.57. ^{13}C NMR of Dimethyl [1,1'-biphenyl]-4,4'-dicarboxylate

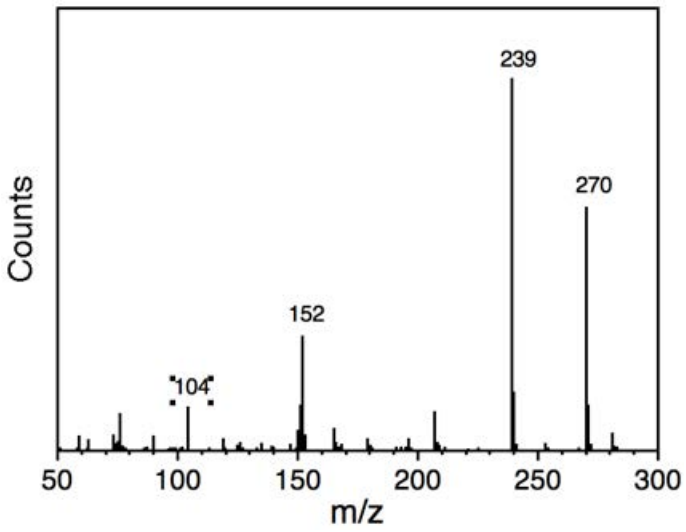

Figure 3.58. MS spectrum of dimethyl [1,1'-biphenyl]-4,4'-dicarboxylate.

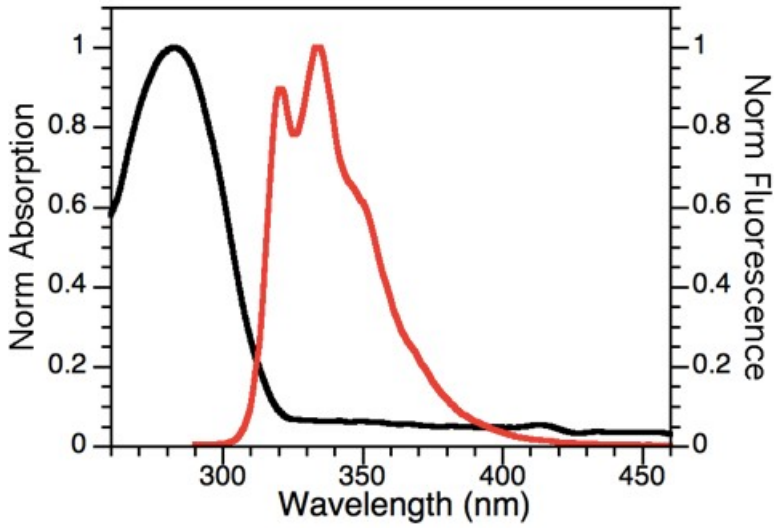

Figure 3.59. UV-Vis and fluorescence spectra (λ_{exc} 278 nm) of dimethyl [1,1'-biphenyl]-4,4'-dicarboxylate.

References

1. Hassan, J.; Sévignon, M.; Gozzi, C.; Schulz, E.; Lemaire, M., Aryl-aryl bond formation one century after the discovery of the Ullmann reaction. *Chem Rev* **2002,** *102* (5), 1359-470.
2. Sampson, P., Metal-Catalyzed Cross-Coupling Reactions Edited by F. Diederich (ETH, Zurich) and P. J. Stang (University of Utah). Wiley-VCH: Weinheim. 1998. xxi + 517 pp. $140. ISBN 3-527-29421-X. *J Am Chem Soc* **1998,** *120* (45), 11836-11837.
3. Negishi, E. i., Magical Power of Transition Metals: Past, Present, and Future (Nobel Lecture). *Angew Chem Int Ed* **2011,** *50* (30), 6738-6764.

4. Rai, R. K.; Tyagi, D.; Gupta, K.; Singh, S. K., Activated nanostructured bimetallic catalysts for C-C coupling reactions: recent progress. *Catal Sci Technol* **2016,** *6* (10), 3341-3361.
5. Ullmann, F.; Bielecki, J., Ueber Synthesen in der Biphenylreihe. *Ber Dtsch Chem Ges* **2006,** *34* (2), 2174-2185.
6. FANTA, P. E., The Ullmann synthesis of biaryls. *Chem Rev* **1946,** *38*, 139-96.
7. Weingarten, H., Mechanism of the Ullmann Condensation1. *J Org Chem* **1964,** *29* (12), 3624-3626.

8. Cohen, T.; Cristea, I., Kinetics and mechanism of the copper(I)-induced homogeneous Ullmann coupling of o-bromonitrobenzene. *J Am Chem Soc* **1976,** *98* (3), 748-753.
9. Marcoux, J.-F.; Doye, S.; Buchwald, S. L., A General Copper-Catalyzed Synthesis of Diaryl Ethers. *J Am Chem Soc* **1997,** *119* (43), 10539-10540.

10. Ackerman, L. K.; Lovell, M. M.; Weix, D. J., Multimetallic catalysed cross-coupling of aryl bromides with aryl triflates. *Nature* **2015,** *524* (7566), 454-7.
11. Sambiagio, C.; Marsden, S. P.; Blacker, A. J.; McGowan, P. C., Copper catalysed Ullmann type chemistry: from mechanistic aspects to modern development. *Chem Soc Rev* **2014,** *43* (10), 3525-50.
12. Judd, C. J.; Haddow, S. L.; Champness, N. R.; Saywell, A., Ullmann Coupling Reactions on Ag(111) and Ag(110); Substrate Influence on the Formation of Covalently Coupled Products and Intermediate Metal-Organic Structures. *Sci Rep* **2017,** *7* (1), 14541.
13. Göksu, H.; Yıldız, Y.; Çelik, B.; Yazıcı, M.; Kılbaş, B.; Şen, F., Highly Efficient and Monodisperse Graphene Oxide Furnished Ru/Pd Nanoparticles for the Dehalogenation of Aryl Halides via Ammonia Borane. *ChemistrySelect* **2016,** *1* (5), 953-958.
14. Basagni, A.; Ferrighi, L.; Cattelan, M.; Nicolas, L.; Handrup, K.; Vaghi, L.; Papagni, A.; Sedona, F.; Valentin, C. D.; Agnoli, S.; Sambi, M., On-surface photo-dissociation of C-Br bonds: towards room temperature Ullmann coupling. *Chem Commun (Camb)* **2015,** *51* (63), 12593-6.

15. Natarajan, S.; Liu, G.; Kim, S. H., Physical Insights into the Photoactivated Ullmann Coupling Process Producing Highly Conjugated Oligothiophene Films on a Copper Substrate. *J Phys Chem B* **2006,** *110* (15), 8047-8051.

16. Dhital, R. N.; Kamonsatikul, C.; Somsook, E.; Bobuatong, K.; Ehara, M.; Karanjit, S.; Sakurai, H., Low-temperature carbon-chlorine bond activation by bimetallic gold/palladium alloy nanoclusters: an application to Ullmann coupling. *J Am Chem Soc* **2012,** *134* (50), 20250-3.
17. Creutz, S. E.; Lotito, K. J.; Fu, G. C.; Peters, J. C., Photoinduced Ullmann C-N coupling: demonstrating the viability of a radical pathway. *Science* **2012,** *338* (6107), 647-51.
18. Niu, F.; Jiang, Y.; Song, W., In situ loading of Cu2O nanoparticles on a hydroxyl group rich TiO2 precursor as an excellent catalyst for the Ullmann reaction. *Nano Res* **2010,** *3* (11), 757-763.
19. Veisi, H.; Morakabati, N., Palladium nanoparticles supported on modified single-walled carbon nanotubes: a heterogeneous and reusable catalyst in the Ullmann-type N-arylation of imidazoles and indoles. *New J Chem* **2015,** *39* (4), 2901-2907.
20. Skubi, K. L.; Blum, T. R.; Yoon, T. P., Dual Catalysis Strategies in Photochemical Synthesis. *Chem Rev* **2016,** *116* (17), 10035-74.
21. Romero, N. A.; Nicewicz, D. A., Organic Photoredox Catalysis. *Chem Rev* **2016,** *116* (17), 10075-166.
22. Shaw, M. H.; Twilton, J.; MacMillan, D. W., Photoredox Catalysis in Organic Chemistry. *J Org Chem* **2016,** *81* (16), 6898-926.
23. Colmenares, J. C.; Luque, R., Heterogeneous photocatalytic nanomaterials: prospects and challenges in selective transformations of biomass-derived compounds. *Chem Soc Rev* **2014,** *43* (3), 765-78.
24. Fox, M. A.; Dulay, M. T., Heterogeneous photocatalysis. *Chem Rev* **1993,** *93* (1), 341-357.
25. Elhage, A.; Lanterna, A. E.; Scaiano, J. C., Light-Induced Sonogashira C–C Coupling under Mild Conditions Using Supported Palladium Nanoparticles. *ACS Sustain Chem Eng* **2018,** *6* (2), 1717-1722.
26. Elhage, A.; Lanterna, A. E.; Scaiano, J. C., Tunable Photocatalytic Activity of Palladium-Decorated TiO_2: Non-Hydrogen-Mediated Hydrogenation or Isomerization of Benzyl-Substituted Alkenes. *ACS Catalysis* **2017,** *7* (1), 250-255.
27. Pagliaro, M.; Pandarus, V.; Ciriminna, R.; Béland, F.; Demma Carà, P., Heterogeneous versus Homogeneous Palladium Catalysts for Cross-Coupling Reactions. *ChemCatChem* **2012,** *4* (4), 432-445.
28. Hainer, A. S.; Hodgins, J. S.; Sandre, V.; Vallieres, M.; Lanterna, A. E.; Scaiano, J. C., Photocatalytic Hydrogen Generation Using Metal-Decorated TiO_2: Sacrificial Donors vs True Water Splitting. *ACS Energy Lett* **2018,** *3* (3), 542-545.
29. Tyagi, A.; Yamamoto, A.; Kato, T.; Yoshida, H., Bifunctional property of Pt nanoparticles deposited on TiO2 for the photocatalytic sp3C-sp3C cross-coupling reactions between THF and alkanes. *Catal Sci Technol* **2017,** *7* (12), 2616-2623.
30. Skene, W. G.; Scaiano, J. C.; Listigovers, N. A.; Kazmaier, P. M.; Georges, M. K., Rate Constants for the Trapping of Various Carbon-Centered Radicals by Nitroxides: Unimolecular Initiators for Living Free Radical Polymerization. *Macromolecules* **2000,** *33* (14), 5065-5072.
31. Evano, G.; Blanchard, N.; Toumi, M., Copper-Mediated Coupling Reactions and Their Applications in Natural Products and Designed Biomolecules Synthesis. *Chem Rev* **2008,** *108* (8), 3054-3131.

32. Wang, B.; Durantini, J.; Nie, J.; Lanterna, A. E.; Scaiano, J. C., Heterogeneous Photocatalytic Click Chemistry. *J Am Chem Soc* **2016,** *138* (40), 13127-13130.

33. Christoforidis Konstantinos, C.; Fornasiero, P., Photocatalytic Hydrogen Production: A Rift into the Future Energy Supply. *ChemCatChem* **2017,** *9* (9), 1523-1544.

34. Malatesta, V.; Scaiano, J. C., Absolute rate constants for the reactions of tert-butoxyl with ethers: importance of the stereoelectronic effect. *J Org Chem* **1982,** *47* (8), 1455-1459.

35. Baldoví, M. V.; Mohtat, N.; Scaiano, J. C., Influence of Acids on Reaction Rates of Free Radical Scavenging by TEMPO. Relevance to "Living" Free Radical Polymerizations. *Macromolecules* **1996,** *29* (16), 5497-5499.

36. Kraatz, H. B.; van der Boom Milko, E.; Ben-David, Y.; Milstein, D., Reaction of Aryl Iodides with (PCP)Pd(II)—Alkyl and Aryl Complexes: Mechanistic Aspects of Carbon—Carbon Bond Formation. *Isr J Chem* **2010,** *41* (3), 163-172.

37. Giacco Tiziana, D.; Rol, C.; Sebastiani Giovanni, V., Involvement of adsorption effects in the TiO2-sensitized photooxidation rate of benzylic derivatives in CH3CN. *J Phys Org Chem* **2003,** *16* (2), 127-132.

38. Sarina, S.; Jaatinen, E.; Xiao, Q.; Huang, Y. M.; Christopher, P.; Zhao, J. C.; Zhu, H. Y., Photon Energy Threshold in Direct Photocatalysis with Metal Nanoparticles: Key Evidence from the Action Spectrum of the Reaction. *J Phys Chem Lett* **2017,** *8* (11), 2526-2534.

39. Berlman, I. B., Identifying the Lowest Excited Singlet State of Biphenyl and Its Analogs. *J Chem Phys* **1970,** *52* (11), 5616-5621.

40. Harvey, P. R.; Rudham, R., Photocatalytic oxidation of iodide ions by titanium dioxide. *J Chem Soc Faraday Trans 1: Physical Chemistry in Condensed Phases* **1988,** *84* (11), 4181-4190.

Chapter 4
Suggestions for Future Work

Future work will focus on taking advantage of the plasmonic properties of silver nanostructures and utilizing visible light to enhance the bactericidal properties of these coated AgNS. In addition to that, testing the coated AgNS on bacterial samples that are collected from humans will be a very valuable experiment as it will give a better idea of the efficiency of using these coated AgNS in medicine. Finally the cytotoxicity of these coated AgNS must be evaluated to make sure that they are not toxic for human cells.

The reaction conditions that were achieved for the Ullmann reaction should be utilized to expand the scope of Ullmann reaction and include C-C coupling between two aryl bromides and two-aryl chlorides. In fact the ability to achieve high selectivity using different excitation wavelengths should be expanded to include more organic synthesis.

Our extensive mechanistic study for the Ullmann project has inspired us on a new project that I am proudly taking part of with Andrew Hainer and Stefanie Rincon. The new project focuses on the free radicals that are generated from ethers and hydrogen production Scheme 4.1

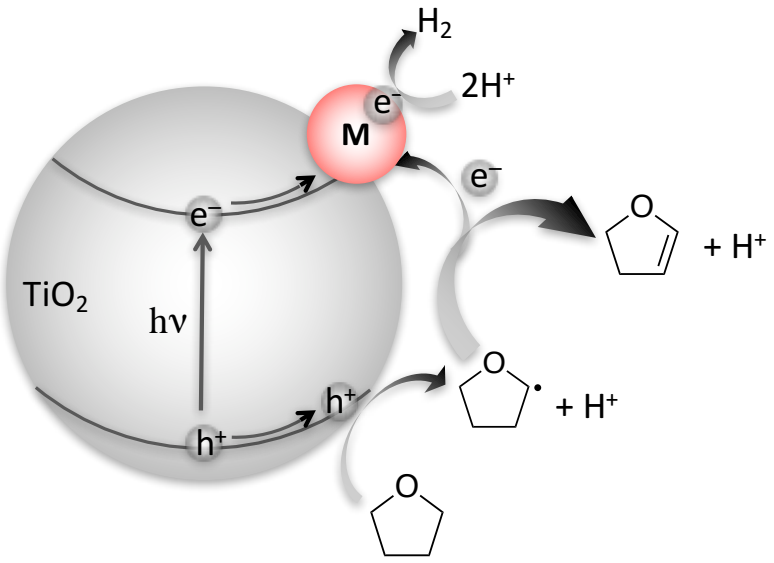

Scheme 4.1 metal decorated TiO_2 that captures the electrons, slowing down electron-hole recombination. Upon irradiation with UVA light, THF forms tetrahydrofuranyl radical which is a very good electron donor and H^+ that is reduced on the surface of the metal, generating hydrogen.

Our research focuses on cyclic ethers, particularly THF. The Scaiano group has broad experience with hydrogen atom transfer (HAT) chemistry of these molecules. [1] Cyclic ethers are not viewed as the typical electron donors used as sacrificial electron donor as alcohols and amines.

In our experiments, we want to focus on using 368 nm as a source of irradiation for the metal decorated TiO_2, such as palladium, i.e. Pd@TiO_2, suspended in THF. Despite the fact that visible light is usually more desirable for solar energy applications, 368 nm is frequently long enough to prevent or minimize product photodegradation during organic synthesis. The photolysis produces generous amounts of H_2 gas, quite comparable with typical sacrificial electron donor SED systems involving methanol or formic acid. The mechanism we propose is shown in scheme 4.2 where we anticipate that the hole will reside in the TiO_2 valence band, while the electrons will move rapidly to the metal particle, effectively their host.

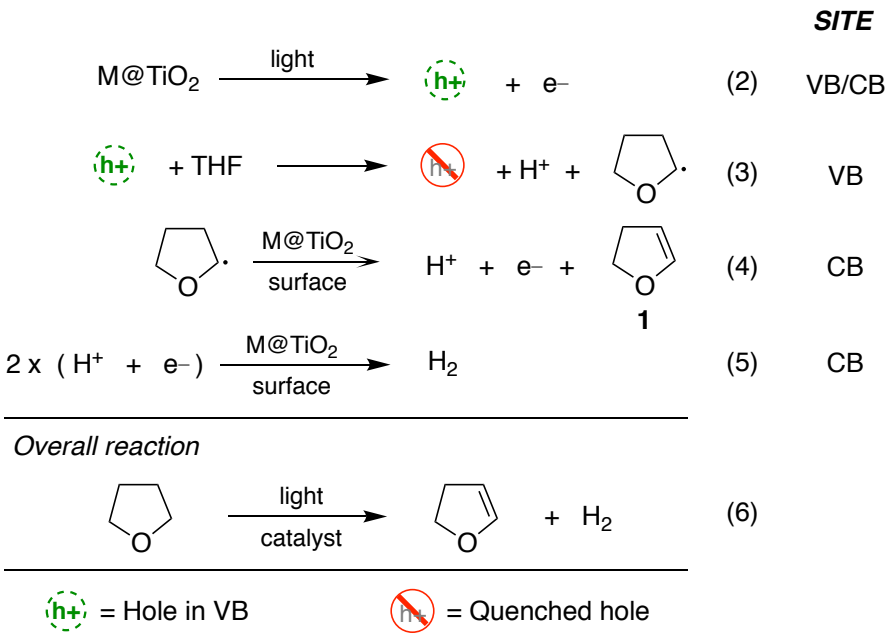

Scheme 4.2: Mechanism for the formation of hydrogen and dihydrofuran from THF. Note that the THF-derived radical formed in reaction 3 is mobile and can undergo solution reactions.

We will be testing different supported metals on TiO_2 in order to find the best catalyst that suits the system. Different cyclic ethers will also be tested in order to find which cyclic ether generates radical more easily and produces more hydrogen. Moreover, TEMPO will be utilized as a free radical scavenger to confirm whether free radicals from ethers are generated or not.

GC-FID and GC-MS will be used to characterize the TEMPO- adduct while thermal conductivity detector TCD will be used to measure how much hydrogen is being produced.

Reference

1. Malatesta, V.; Scaiano, J. C., Absolute rate constants for the reactions of tert-butoxyl with ethers: importance of the stereoelectronic effect. *J Org Chem* **1982,** *47* (8), 1455-1459.